PHD DISSERTATION

Theoretical and Experimental Characterization of the 60 GHz Radiocommunication Channel

Author:

Maria Teresa Martínez Inglés

Supervisor:

Dr. D. José María Molina García-Pardo (1)

Dr. D. José Víctor Rodríguez Rodríguez (1)

Prof. Mme. Martine Liénard (2)

(1) Universidad Politécnica de Cartagena (UPCT)
(2) Université des Sciences et Technologies de Lille (USTL)

Cartagena, June 2014

Rapport de soutenance de thèse

EN COTUTELLE

Nom et prénom : Mme MARTINEZ INGLES MARIA TERESA

Titre de la thèse :
THEORETICAL AND EXPERIMENTAL CHARACTERIZATION OF THE 60 GHZ
RADIOCOMMUNICATION CHANNEL

Discipline : Micro et Nano Technol.Acoust.Télécomm
Date de soutenance : 17/10/2014

Maria Teresa Ingles Martinez has defended her thesis entitled:" Theoretical and experimental characterization of the 60 GHz radiocommunication channel". Her very good presentation was unanimously considered by the jury as highly pedagogical and well-structured. She presented her research work with a concern of clarity. The jury asked numerous questions for which Maria Teresa Ingles Martinez gave accurate responses and demonstrated her in-depth knowledge of various issues in electromagnetism, experimentation, channel characterization and modeling aspects.

For all these reasons, the jury unanimously awarded Maria Teresa Ingles Martinez the degree of doctor of Universidad Politécnica de Cartagena and Université de Lille 1 with the highest possible honor.

Mention :

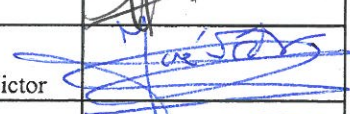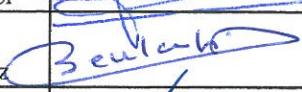☐ Honorable   ☒ Très Honorable

L'USTL n'attribue plus de mention "Très Honorable avec les Félicitations" (par décision du Conseil Scientifique du 15 juin 2007)

Nombre de pages du rapport :

Jury :
Président : NARCIS CARDONA
Signatures des membres

LIENARD Martine			
RODRIGUEZ Jose Victor			
BENLARBI DELAI Aziz			
CARDONA Narcis			

Acknowledgements

The realization of this thesis was not only the result of my own effort, but of everyone who has been by my side throughout this time. I have been surrounded by many people who gave me their time and support both in good times and in bad times.

I would like to start with the Spanish part of this thesis, the Universidad Politécnica de Cartagena, where I started to work in 2009.

Firstly, I would like to thank my Spanish supervisors Jose María Molina and Jose Victor Rodriguez for having given me the opportunity and for providing me with the means for reaching this conclusive point of my thesis. Everything that I have learnt is thanks to you, and without your patience and dedication all these years, it would have been impossible to finish the thesis. I would like to thank Juan Pascual for always being there when I have needed something. I would like to thank Leandro Juan for his time and for his belief in my ability to do this thesis.

I could never forget to thank my colleagues from the SiCoMo research group: María and Conchi. The time we shared was very pleasant and I really miss you a lot. The laboratory is not the same without you.

I do not want to forget the technical staff of the department, especially Noelia, who has been so attentive in solving my problems in a very effective way.

Finally, I would like to thank all the Departamento de Tecnologías de la Información y las Comunicaciones, from its head, Juan Morales, to the secretary, Ana Rodríguez.

I also need to give acknowledgment to the French part. The people from the Université des Sciences et Technologies de Lille and particularly at the TELICE research group who gave me the great opportunity of staying with them.

Firstly, I would like to thank my third supervisor and head of the TELICE group, Martine Liénard. Her help, support and dedication have helped me to overcome and develop some important issues of the thesis. Thanks a lot for her useful suggestions to improve this work.

Especially, I would like to thank Davy. Thank you for your friendship and your patience with the measurements. I would also like to thank Pierre Degauque and his wife for their great support on the things that I needed for living there. I would also like to thank Pierre Laly for his special greeting every morning, for his affection and friendship and for the last marvelous dinner with his family.

I do not want to forget to thank the secretary of the TELICE group, Emmanuelle Gillmann, for her help with a lot of administrative tasks that I have needed and for her nice behavior towards me.

Finally I would like to thank all the members of TELICE group. I have still remembered the foods in stadium. Thanks for making me feel one of you.

Now, I would like to mention the people on the personal side of my life.

Firstly, I would like to thank my parents, Jesus and Juani, for encouraging me to do my degree. Without the effort of my father during that summer for persuading me to choose my degree, my life would be different. I would also like to thank them for their advice, help and support in the difficult moments. Thank you for being such excellent role models of effort and work well done since I was a child.

I would like to thank my brother, Antonio Tomás and my sister Ana, for always giving me their support and trust. Thank you for always being close to me and making me laugh. In particular, I would like to mention my grandmother Ana María. Although she

does not understand what I do, she always encourages me and takes care of me with her marvelous food. Many thanks for your unconditional love. I would like to thank my nephew Antonio Jesus for giving me his special smile every time we meet. I do not want to forget to thank Cari, Pepe and Cary for their support and advice.

I would like to thank my friends, Mariana, Ainhoa and Inma, for always being close to me although we live far apart. Thank you for all the moments we have shared and for your advice during this challenge. I would also like to thank Victoria Bueno for her advice and friendship during the last years at University.

Finally, but not any less important, I would like to thank Jose Mª, my husband and Jose Jesus, my son for everything. If they had not supported me, this would not have been possible. Firstly, my son. I would like to say that I am sorry for all the moments that I could not play with him. Thank you for your love, hugs and smiles and for being the best child in the world for me. Regarding my husband, there are not words to express my feelings of gratitude. Thank you for believing in me and encouraging me when I needed it most and for being patient all the time.

This thesis was made possible by the things that every one of you gave me. Thank you everybody.

All of you are a part of this work.

Preface

The forthcoming wireless communication systems are expected to demand higher data rates and improved capacity bounds in order to provide the next generation of broadband multimedia services. In this context, the 60 GHz-frequency band has captured the interest of researchers due to the large bandwidth available and the small frequency reuse distance offered. This band offers the possibility of the development of short-range indoor systems with low-power transmitters and data transfer rates of up to several gigabits per second.

This thesis is focused in the theoretical and experimental characterization and modeling of the radio channel for 60 GHz systems and for large bandwidth channels by means of the analysis of measurements in different scenarios as well as the development of a channel sounder. Apart from that, ray tracing is also used to predict propagation at such frequencies. Moreover, different formulations for radiowave multiple diffraction analysis at the millimeter band have been studied and validated by measurements.

Contents

Appendices

Chapter 1

Introduction

1.1 Motivation and Objectives

Forthcoming wireless communication systems are expected to demand higher data rates and improved capacity bounds in order to provide the next generation of broadband multimedia services. In this context, the *60 GHz-frequency band* has captured the interest of researchers due to the large bandwidth available [Smulders, 2002], [Mikkonen, 1998], and the small frequency reuse distance offered [Luise, 1999].

Certainly, this interest is mostly concentrated in the extremely wide band available in the unlicensed *60 GHz band* (57–66 GHz for Europe). This frequency range allows wireless data rates of several Gigabits per second (*Gbps*) [Smulders, 2002], opening the door to a great deal of potential applications which require high data rates and short distances:

- *Wireless personal area networks* (*WPAN*). Wireless links can replace Ethernet (1000 Mbps), USB 2.0 (480 Mbps) or IEEE 1394 (800 Mbps) cables at home or in the office.
- Wireless video streaming. Uncompressed *high definition* (*HD*) video may require 1.5 Gbps, at the lowest.
- Vehicular applications. Two types can be recognized: intra-vehicle networks, which are a subset of *WPANs* and are oriented to remove wired connections from the car or even the aircraft cabin [Peter, 2007bis]. Also, inter-vehicle networks for delivery of traffic information.
- Fiber extensions (at *E-band*). *E-band* (70/80 GHz) is ideally suited to complement fiber in those cases where fiber is difficult or expensive to deploy, such as crossing rivers or railways. Also for fiber backup connections.

Yet, gigabit wireless is not the only motivation. The automotive industry is incorporating millimeter-wave radar units to its high-end vehicles. These units, operating at 77 GHz, provide features such as autonomous cruise control, collision avoidance, low-visibility driving aid, early warning systems, and may become standard in future intelligent highway systems [Natarajan, 2006], [Hajimiri, 2005].

Finally, *millimeter-wave* (and *THz*) imaging is proving to be a valuable tool in situations where visible, infrared or X-ray are insufficient. *Millimeter waves* can provide images under poor weather conditions (fog, clouds) which are useful for surveillance, rescue or aircraft landing [Yujiri, 2003] and can also be used to inspect persons rapidly for concealed weapons [Anderton, 2006].

Despite the appealing foreseen applications, systems in the *millimeter-wave* range face many challenges both from the channel performance point of view, and from the front-end realization perspective.

Regarding the channel performance, the implementation of such wireless systems raises several challenges in channel modeling.

In general, the modeling of the radio channel can be undertaken in two main ways:

- *Theoretically*, where the channel is characterized by means of simulations and theoretical approaches.

- *Experimentally*, where the radio channel is characterized by means of the analysis of measurements carried out in real scenarios.

This thesis is mainly focused on the experimental characterization and modelling of the radio channel for systems with large bandwidth in the millimeter frequency band for indoor environments. However, characterizing experimentally the radiowave wideband channel implies the availability of adequate and accurate channel sounders.

There are many parameters which characterize the radio channel, such as *path loss*, *RMS delay spread*, *angular spread*, and so on. The complex correlation coefficient or the capacity also define the performance of multiantenna systems. All these parameters can be deduced from experimental measurements. Thus, the particular behavior of the radio channel where measurements were carried out can be observed.

Thus, the objectives pursued in this thesis are:

1) The realization of the updated state-of-the-art in propagation models and channel sounders for *60 GHz* systems. This is an important task since it makes possible to optimize the research efforts finding research needs.
2) Development of a *frequency-domain MIMO* channel sounder in order to perform measurements in the millimeter band to measure the radio channel response.
3) Characterization and modeling of the main parameters of double channel propagation in millimeter frequencies.
4) Comparison between the centimeter and millimeter wave through measurement campaigns.
5) Exhaustive study of the multiple diffraction phenomenon in the millimeter band in order to validate theories about multiple diffraction.
6) Study of the standards, such as *IEEE 802.15.3c*, in the millimeter band through measurements.

1.2 Thesis Overview

In this section the organization and presentation of the work of this thesis is summarized.

Chapter 2 is devoted to the issue of propagation in the *mm-W* frequency band. Firstly, the concept of multipath propagation is described and the different environments in which the *mm-W* technology is applied are exposed. Next, the two types of used channel sounders in the *mm-W* band are presented. Large scale parameters and the main aspects about the wideband channel, such as characterization and modeling, are detailed. Finally, the issues which will be solved by this thesis are presented.

Chapter 3 deals with the study of the phenomenon of *radiowave multiple diffraction* in several scenarios and at the frequencies corresponding to the *mm-W* band. Four scenarios are presented with different numbers and shapes of obstacles. For every obstacle a brief introduction explains the issue. Then, the theoretical model scenario and the measurement setup are detailed. Finally, the obtained results and conclusions are showed.

Chapter 4 is about the modeling and characterization of the multidimensional millimeter channel. In this chapter, by means of indoor measurements in the 57–66 GHz frequency range, different aspects related to propagation are studied: double directional channel characterization, diffuse scatter analysis, *cm-W* and *mm-W* propagation comparison and the study of performance of the *IEEE 802.15c* standard.

This thesis concludes with Chapter 5 where the general conclusions of this thesis are summarized. The future perspectives and research lines derived from this work are also proposed in this chapter.

Furthermore, three appendices are annexed at the end of the thesis in order to treat some transversal topics and contribute to the overall comprehension of this thesis: *Appendix A* summarizes some basic concepts about the main propagation mechanisms. In *Appendix B*, the description of the main components of the used channel sounders in the thesis is presented. Next, the mentioned formulation for radiowave multiple diffraction in Chapter 3 is explained in depth in *Appendix C*. Finally, in *Appendix D* the diffuse scattering parametric study is shown.

1.3 Scientific Publications

This thesis has given rise to 7 international journals (*IJ*) indexed in to the Journal Citation Reports, 13 international conferences (*IC*) and 4 national conferences (*NC*).

Particularly, the work of Chapter 3 has been published in 4 international journal, 2 international conferences and 2 national conferences:

IJ Maria-Teresa Martinez-Ingles, José-Víctor Rodríguez, Jose-Maria Molina-Garcia-Pardo, Juan Pascual-García and Leandro Juan-Llácer, "Comparison of a UTD-PO Formulation for Multiple-Plateau Diffraction With Measurements at 62 GHz", *IEEE Transactions on Antennas and Propagation*, vol. 61, no 2, pp. 1000-1003, February 2013. Digital Object Identifier: 10.1109/TAP.2012.2224836.

IJ Maria-Teresa Martinez-Ingles, José-Víctor Rodríguez, Jose-Maria Molina-Garcia-Pardo, Juan Pascual-García and Leandro Juan-Llácer, "Parametric Study and Validation of a UTD-PO Multiple-Cylinder Diffraction Solution through Measurements at 60 GHz", *IEEE Transactions on Antennas and Propagation*, vol. 61, no. 8, pp. 4397-4400, August 2013. Digital Object Identifier: 10.1109/TAP.2013.2262665.

IJ Maria-Teresa Martinez-Ingles, José-Víctor Rodríguez, Jose-Maria Molina-Garcia-Pardo, Juan Pascual-García and Leandro Juan-Llácer, "Experimental and Theoretical Comparison of Cylindrical Against Rectangular Obstacles in mm-Wave Multiple Diffraction", *IEEE Transactions on Antennas and Propagation*, vol. 61, no. 10, pp. 5347-5350, October 2013. Digital Object Identifier: 10.1109/TAP.2013.2273409.

IJ Maria-Teresa Martinez-Ingles, Juan Pascual-García, José-Víctor Rodríguez, Rubén López-Moya, Jose-Maria Molina-Garcia-Pardo, and Leandro Juan-Llácer, "UTD-PO Solution for Estimating the Propagation Loss due to the Diffraction at the Top of a Rectangular Obstacle when Illuminated from a Low Source", *IEEE Transactions on Antennas and Propagation*, vol. 61, no. 12, December 2013. Digital Object Identifier: 10.1109/TAP.2013.2281822.

IC Maria-Teresa Martinez-Ingles, José-Víctor Rodríguez, Jose-Maria Molina-Garcia-Pardo, Juan Pascual-García and Leandro Juan-Llácer, "Comparison of a UTD-PO Formulation for Multiple Diffraction of Rectangular Obstacles with Measurements in the Millimetre-Wave Frequency Band", *COST IC1004 TD(12)04005,* Lyon, France. 2-4 May, 2012.

NC Maria-Teresa Martinez-Ingles, José-Víctor Rodríguez, Jose-Maria Molina-Garcia-Pardo, Juan Pascual-García and Leandro Juan-Llácer, "Comparación de una Formulación UTD-PO para el Análisis de la Difracción Múltiple de Obstáculos Rectangulares con Medidas a 62 Ghz", *XXVII Simposium Nacional de la Unión Científica Internacional de Radio,* Elche, Comunidad Valenciana, España. 12-14 September 2012.

IC Maria-Teresa Martinez-Ingles, José-Víctor Rodríguez Jose-Maria Molina-Garcia-Pardo, Juan Pascual-García and Leandro Juan-Llácer, "Multiple-Cylinder Diffraction Measurements at 60 GHz", *7th European Conference on Antennas and Propagation,* Gothenburg, Suecia. 8-12 April 2013.

NC Maria-Teresa Martinez-Ingles, José-Víctor Rodríguez, Jose-Maria Molina-Garcia-Pardo, Juan Pascual-García and Leandro Juan-Llácer, "Validación de una solución UTD-PO para el análisis de la difracción múltiple de cilindros a través de medidas a 60 GHz", *XXVIII Simposium nacional de la unión científica internacional de radio URSI*, Santiago de Compostela, Spain. 11-13 September 2013.

The work of Chapter 4 has been published in 3 international journals, 11 international conferences and 2 national conference:

IJ Maria-Teresa Martinez-Ingles, Concepción Sanchis-Borras, José-María Molina-García-Pardo, José-Víctor Rodríguez and Leandro Juan-Llácer, "Experimental evaluation of an indoor mimo-ofdm system at 60 GHz based on the IEEE802.15.3c standard", *IEEE Antennas and Propagation letteres*, vol. 12, pp. 1562 – 1565. December 2013. ISSN 1536-1225.

IJ Maria-Teresa Martinez-Ingles, Davy P. Gaillot, Juan Pascual-García, Jose-Maria Molina-Garcia-Pardo, Martine Liénard and José-Víctor Rodríguez, "Deterministic and Experimental Indoor mmW Channel Modeling", *IEEE Antennas and Propagation letteres,* vol. 13, pp. 1047-1050. December 2014. Digital Object Identifier: 10.1109/LAWP.2014.2327054.

IJ Maria-Teresa Martinez-Ingles, Jose-Maria Molina-Garcia-Pardo, Juan Pascual-García, José-Víctor Rodríguez and Leandro Juan Llácer, "Experimental Comparison between Centimeter- and Millimeter-Wave Ultra-Wideband Radio Channels", *Radio Science,* vol. 49, June 2014. Digital Object Identifier:10.1002/2014RS005439.

IC Maria-Teresa Martinez-Ingles, Jorge Angosto-Tebas, Concepción García-Pardo, Juan Pascual-García, José-Víctor Rodríguez, Jose-Maria Molina-Garcia-Pardo and Leandro Juan-Llácer. "Design of a 60GHz Channel Sounder and Initial Measurements". *COST IC1004 TD(11)01015*. Lund, Suecia. 20-21 June 2011.

IC Maria-Teresa Martinez-Ingles, Concepción García Pardo, Juan Pascual García, Jose-Maria Molina-Garcia-Pardo, José-Víctor Rodríguez, Juan Reig and Leandro Juan Llácer. "Initial Experimental Characterization of the Millimeter-Wave Radio Channel". *6th European Conference on Antennas and Propagation*, 26-30 March 2012.

IC Maria-Teresa Martinez-Ingles, Concepción García-Pardo, Juan Pascual-García, José-Víctor Rodríguez, Jose-Maria Molina-Garcia-Pardo and Leandro Juan-Llácer, "Indoor 60 GHz Measurements and Comparison with Ray Tracing", *COST IC1004 TD(12)080* Barcelona, Spain. 08-10 February 2012.

IC Maria-Teresa Martinez-Ingles, Juan Pascual-García, José-Víctor Rodríguez, Jose-Maria Molina-Garcia-Pardo and Leandro Juan-Llácer, Davy P. Gaillot, Martine Liénard, and Pierre Degauque. "Indoor radio channel characterization at 60 GHz". *COST IC1004 TD(12)05050* Bristol, United Kingdom 24-26 September 2012.

IC Maria-Teresa Martinez-Ingles, Jose-Maria Molina-Garcia-Pardo, José-Víctor Rodríguez, Juan Pascual-García, and Leandro Juan-Llácer, "Comparison of Indoor Radio Channels at 2–10 and 57–66 GHz". *COST IC1004 TD(13)06088*. Málaga, Spain. 6-8 February 2013.

IC Maria-Teresa Martinez-Ingles, Juan Pascual-García, José-Víctor Rodríguez, Jose-Maria Molina-Garcia-Pardo, Leandro Juan-Llácer, Davy P. Gaillot, Martine Liénard and Pierre Degauque. "Indoor radio channel characterization at 60 GHz". *7th European Conference on Antennas and Propagation.* Gothenburg, Suecia. 8-12 April 2013.

IC Maria-Teresa Martinez-Ingles, Jose-Maria Molina-Garcia-Pardo, José-Víctor Rodríguez, Juan Pascual García and Leandro Juan Llacer. "Experimental comparison of UWB against MM-Wave indoor radio channel characterization". *IEEE Antennas and Propagation Symposium*. Orlando, Estados Unidos de América. 7-13 July 2013.

IC Maria-Teresa Martinez-Ingles, Concepcion Sanchis-Borras, Jose-Maria Molina-Garcia-Pardo, José-Víctor Rodríguez and Leandro Juan-Llácer. "Experimental Evaluation of an Indoor MIMO-OFDM System at 60 GHz based on the IEEE802.15.3c standard". *COST IC1004 TD(13)08004*, Ghent, Belgium, 23-27 September 2013.

IC Maria-Teresa Martinez-Ingles, Davy Gaillot, Juan Pascual García, Jose-Maria Molina-Garcia-Pardo, Martine Liernard and José-Víctor Rodríguez. "On clustering for deterministic and measured indoor mmW channels", *8th European Conference on Antennas and Propagation*. La Haya, Holand. 6-11 April 2014.

IC Maria-Teresa Martinez-Ingles, Juan Pascual-García, José-Víctor Rodríguez, Jose-Maria Molina-Garcia-Pardo and Leandro Juan-Llácer, Davy P. Gaillot, Martine Liénard, and Pierre Degauque. "On Indoor Clustering at the mmW Band". *COST IC1004 TD(14)10001* Aalborg, Denmark 26-28 May 2014.

IC Maria-Teresa Martinez-Ingles, Davy P. Gaillot, Juan Pascual-Garcia, Jose-Maria Molina-Garcia-Pardo, Martine Lienard, José-Víctor Rodríguez, Leandro Juan-Llacer and Pierre Degauque, "Channel Modeling at mmW using Ray Tracing", *European Conference on Networks and Communications Bolgona, Italy, June 23/26 2014*

NC Maria-Teresa Martinez-Ingles, Juan Pascual García; José-Víctor Rodríguez; Jose-Maria Molina-Garcia-Pardo, Leandro Juan Llacer; Davy Gaillot, Martine Lienard and Pierre Degauque. "Caracterización del canal radio en un entorno interior en la banda de 60 GHz". *XXVIII Simposium Nacional de la Unión Científica Internacional de Radio URSI*. Santiago de Compostela, Spain,11-13 September 2013.

NC Maria-Teresa Martinez-Ingles, Concepcion Sanchis-Borras, Jose-Maria Molina-Garcia-Pardo, Juan Pascual-Garcia, José-Víctor Rodríguez and Leandro Juan-Llácer. "Evaluación experimental de un Sistema MIMO-OFDM basado en IEEE802.15.3c en interiores". *VII Jornadas de Introducción a la Investigación 2014*, Cartagena, 7-9 May 2014.

1.4 Cotutelle Framework

The work here presented is within the framework of the following research project: TEC2010-20841-C04-03, from the *Ministerio de Economia y Competitividad* of Spain.

The stage at TELICE research group in 2013 has also been funded by the *Ministerio de Economia y Competitividad* of Spain (Orden Ministerial del 24/2/2011) and European funds.

Chapter 2

State of the art

The *millimeter wave frequency band* is nowadays seen as the most feasible wireless frequency band for transmitting several gigabits via radio. The interest in this band relies on it being an unlicensed band for commercial applications and its ability to provide extremely high data rates [Park, 2007]. The *IEEE 802.15.3c* task group (*TG3c*) has recently published the standard for the millimeter-wave(*mm-W*)-based alternative physical layer extension for *IEEE 802.15.3c* [IEEE 802.15.3, 2009], which uses the 60 GHz band for wireless personal area networks in the so-called *Wireless Gigabit Ethernet*.

Simultaneously, the industry has created the consortium *Wireless Gigabit Alliance*, commonly called *WiGig* [WiGig, 2010], which is devoted to the development and promotion of wireless communications in the 60 GHz band.

The propagation characteristics in the *mm-W* band are quite different from those in the lower frequency bands commonly used today for cellular communication. The smaller received aperture at *mm-W* makes the received power much lower than at *centimeter-wave*

(*cm-W*) frequencies. Furthermore, since the dimensions of typical shadowing objects are large in relation to the wavelength in *mm-W*, sharp shadow zones are formed. Also, due to the high penetration loss of most materials at 60 GHz, multi-path components propagating through walls or other objects typically have low power.

This chapter is devoted to presenting the problem of propagation in the *mm-W* frequency band.

2.1 Multipath Propagation

2.1.1 Multipath Propagation Phenomena

In a realistic environment, signal transmission follows not only a direct path, but also a number of different propagation paths. In the presence of a direct path, line of sight (*LoS*) propagation is defined, while, if the direct path is obstructed, propagation occurs in so-called non-line of sight (*NLoS*) conditions.

These paths undergo various effects, depending on the type of interaction between the wave and the surrounding objects, such as diffraction, reflection or scattering. These phenomena give rise to an attenuation of the signal and to a phase rotation, due to the impedance mismatch between the wave impedance of the object and the free space impedance of the incident plane wave. Furthermore, the length of each path relating the transmitter (*Tx*) and the receiver (*Rx*) is different, leading to time delays between the waves associated to these paths or, similarly to phase shifts in the frequency domain. At the output port of the receiving antenna, the observed signal corresponding to the summation of the different waves, multipath propagation mechanisms may lead to a significant distortion of the received signal.

It must be emphasized that for *mm-W* and in practical situations, the distance between *Tx* or *Rx* and any object is always much greater than the wavelength. One can thus assume that the plane wave assumption is valid and the concept of rays as well. For example, the far field for a $\lambda/2$ dipole at 60 GHz is 2.5 mm.

Figure 2.1 illustrates the concept of *multipath propagation* and the main propagation mechanisms which are described in *Appendix A*.
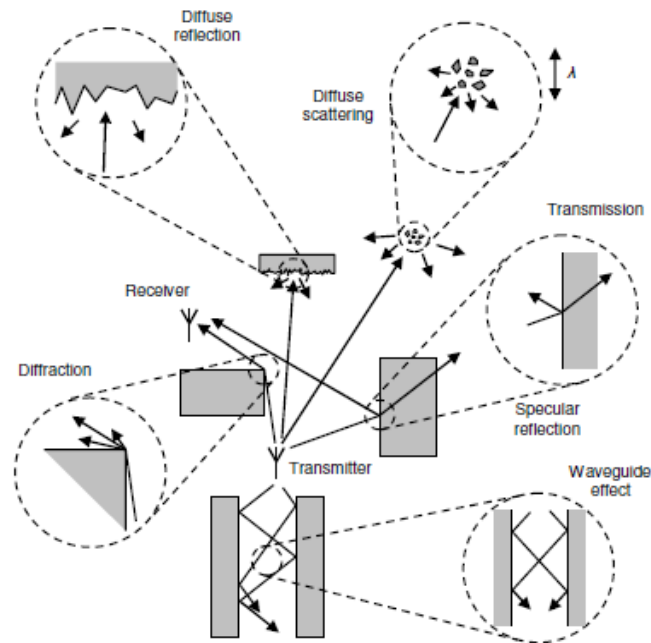
Figure 2.1: Main propagation mechanisms [Pagani, 2008].

If propagation modeling is considered, it is also useful to introduce the concept of *cluster*.

A cluster is defined as a superposition of multiple paths of similar propagation characteristics, as depicted in Figure 2.2. In this figure, the cluster or group of scatters is defined by its mean angle of departure (θ_T, φ_T) (direction of departure – *DoD*), mean angle of arrival (θ_R, φ_R) (direction of arrival – *DoA*), and time-delay of arrival (*ToA*). (θ, φ) refers to the azimuth and elevation angle of the rays, the subscripts *T* and *R* referring to the ray departing from *Tx* and to the ray arriving on *Rx*, respectively. For each of these two rays, one can associate electric field e_T and e_R. From experimental results, it is difficult to extract, for a given propagation path, the exact number of clusters, since hidden clusters or twin clusters could exist [Sibille, 2010]. As we will see in the following chapters, a deterministic model would help in the understanding of these clusters.
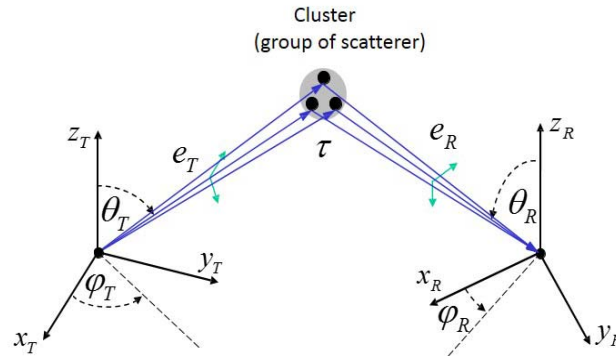
Figure 2.2: Representation of a cluster.

2.1.2 Classification of the Environments

The applications of mm-W technology are mainly dedicated to indoor or short-range high data rate communications. Therefore, five environments have been identified in the *IEEE 802.15.3c*: Residential, office, library, desktop and kiosk [IEEE 802.15.3, 2009]. For all of these except kiosk, two channel models are proposed corresponding to *LoS* and *NLoS* configurations and based on measurements. In both cases, the centre frequency is 62.5 GHz and the frequency bandwidth is 3 GHz. Measurements cover a range from 1 m to 5 m for *LoS* office while for the *NLoS* case the range is in the order of 10m. However, only two configurations were studied and it thus seems difficult to generalize these results to other office environments.

Despite the significant efforts which have been carried out in [IEEE 802.15.3, 2009] to make models as realistic as possible, the number of available measurements on which the model can be based in the 57–64 GHz range, as well as the number of available measurement data, are insufficient to fully characterize the underlying environments.

Nevertheless, additional measurements have been carried out by many other authors and an overview of the main channel characteristics is presented in [Fu, 2013]. The results reported in this paper were obtained in offices of various sizes, varying from 25 m^2 to 100 m² and equipped with different types of floor and furniture. Large variations of the channel parameters are outlined, but interpretation of the results is difficult since they have been obtained with quite different experimental set-ups (antennas, bandwidth, sampling, etc.)

2.2 Propagation Channel Characterization and Modelling

Double directional propagation channel characterization concerns estimation from measurements or deterministic models of the characteristics of paths in terms of *DoD*, *DoA*, *ToA* and *amplitude* [Sibille, 2010]. It must be emphasized that polarization aspects have not yet been considered in literature. The experimental approach needs an accurate wideband *multiple-input-multiple-output* (*MIMO*) channel sounder, while the deterministic approach needs a fine description of the environment, and it must take all the propagation phenomena into account, including the scattering effect which appears when the wavelength becomes smaller than the size or roughness of some furniture. This point will be discussed in Chapter 4.

2.2.1 Channel Sounding

Channel sounding are generally constructed to capture either time of frequency domain snapshots [Rappaport, 1996]. In the case of *mm-W*, two different channel sounders are generally used. The former is based on a 5.3 GHz channel sounder with up-converters to reach mm-W bandwidth [Kivinen, 2007]. To get the channel impulse response, this technique, based on a sliding correlator does not request any reference cable between the *Tx* and *Rx*, and real-time sampling enables numerous successive snapshots. Averaging the received signals allows the *signal to noise ratio* (*SNR*) to be increased. Unfortunately, this 5.3 GHz sounder has a limited bandwidth of 100 MHz, this bandwidth being kept after the up-converter. That channel sounder can be used to determine the *DoD/DoA* of the rays by means of virtual *MIMO* arrays; however, in this case the phase continuity is a major concern. Modification of the previous sounder is introduced in [Ranvier, 2007]. In order to synchronize the transmitter and the receiver and avoid phase drifts, the same 14-GHz synthesizer was used, and both *Tx* and *Rx* connected by a 25-meter low loss cable.

The second type of channel sounder concerns those based on a frequency domain implemented with a vector network analyzer. A review of such types of channel sounders with different characteristics and performances is given in [Fu, 2013] and [Yong, 2011]. These sounders need an *RF* cable between *Tx* and *Rx* and the calibration procedure must be carefully done since this cable can introduce phase distortion in *mm-W*. The work of this thesis will be based on this latter approach.

2.2.2 Large Scale Parameters: Path Loss and Shadowing

The *Path Loss* (*PL)* is defined as the ratio between the transmitted power and the received power, which describes the attenuation of the transmitted signal in the radio link. *PL* is a very important characteristic for link budget analysis in order to ensure that the actual deployment can meet the coverage of the target area.

For frequency selective channels and for a given distance, *d*, between *Tx* and *Rx*, one can introduce the *average large-scale path loss* defined as the mean path loss in the frequency band under consideration. *PL*(*d*) can be determined from measurements in the time or frequency domain. For the latter, if the band is divided into *Nf* discrete frequencies, *PL*(*d*) is deduced from the transfer function *H*(*d,f*) as:

$$\overline{PL(d)}_{dB} = -10\log_{10}\left(\frac{1}{Nf}\sum_{f=1}^{Nf}\left|H(d,f)\right|^2\right) \qquad (2.1)$$

Experimental results have shown that *PL*(*d*) decreases logarithmically with distance, both for outdoor and indoor radio channels [Rappaport, 1996]. It can thus be expressed as a function of distance by using a path loss exponent, *n*, as:

$$\overline{PL(d)}_{dB} = \overline{PL(d_0)} + 10n\log\left(\frac{d}{d_0}\right) \qquad (2.2)$$

where $\overline{PL(d_0)}$ is the mean path loss at a reference distance (usually 1 m). The exponent *n* is strongly dependent on the environment.

The *shadowing* is due to the variation of the surrounding environments; as a consequence, the received power will vary around its mean value. Thus, the shadowing is introduced in (2.3) by the random variable X_{σ_e}:

$$\overline{PL(d)}_{dB} = \overline{PL(d_0)} + 10n\log\left(\frac{d}{d_0}\right) + X_{\sigma_e} \qquad (2.3)$$

where X_{σ_e} is a zero-mean Gaussian distributed random variable in decibels with standard deviations σ_e (also in dB).

Table 2.1 provides an overview of *path loss* parameters deduced from measurements at 60 GHz in an office environment and by considering omnidirectional antennas. This table shows that for a given size of the environment, the path loss exponent is of the order of 1.17, the standard deviation of the shadowing effect varying from 1.3 to 5.4. However, it must be outlined that in the two experiments, the radiation pattern of the antennas are not identical.

Reference	Antennas Tx/Rx	D(m)	PL(do)Min/Max	n	σ_e
[Yang, 2005] office 66m²	Biconical	1–6	50.3/69.8 dB	1.17	1.3/2.7
[Yong, 2007]	Omni/Horn 30°HPBW		84.6	1.16	5.4

Table 2.1: Overview of path loss parameters.

Let us mention that in [Collonge, 2004], the authors quantify the signal attenuation when the direct path is shadowed by persons. They concluded that the attenuation generally increases by more than 20 dB, for a median duration of about 100 ms in the presence of one to five persons and of 300 ms in the presence of 11–15 persons. These values give an idea of the time variation of the indoor 60 GHz channel.

2.2.3 Wideband Aspects

2.2.3.1 Small Scale Propagation Channel: Description

A wideband radio channel model needs a detailed insight into the complex radio wave propagation mechanisms. As depicted in Figure 2.3, the description of the channel can be "coarse" including the *Tx* and *Rx* antenna effects; therefore the measured impulse response can be expressed in terms of complex amplitudes and delays of the various paths. On the other hand the finest description of the so-called double directional channel excludes the antenna's effect, and the *DoA*, *DoD* and *amplitude* of each path can be identified. The channel is therefore fully described by the *complex impulse response* (*CIR*) $h(t,\tau,\varphi_T,\varphi_R)$, given by (2.4) [Richter, 2005]. This is the most complete form of the impulse response, also taking into account the polarization matrix of any path *k* and where γ_{VV} and γ_{HH} are the co-polarized complex amplitude for vertical and horizontal

polarization respectively, γ_{VH} and γ_{HV} are the complex amplitudes for the cross-polarized configuration. As an example, γ_{VH} refers to a *Tx* antenna vertically polarized and a *Rx* antenna horizontally polarized.
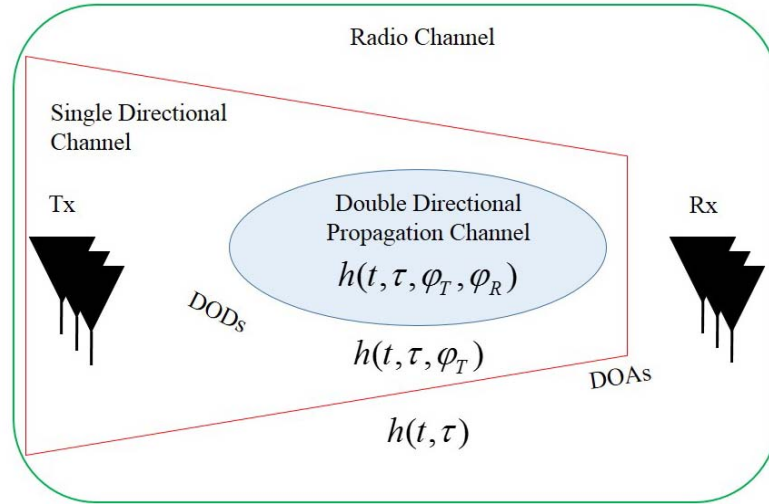
Figure 2.3: Radio channel and double directional propagation channel.

$$h(t,\tau,\varphi_T,\varphi_R) = \sum_{k=1}^{K} \begin{bmatrix} \gamma_{HH,k} & \gamma_{HV,k} \\ \gamma_{VH,k} & \gamma_{VV,k} \end{bmatrix} \cdot \delta(t-t_k)\delta(\tau-\tau_k) \cdot \delta(\varphi_T-\varphi_{T_k}) \cdot \delta(\varphi_R-\varphi_{R_k}) \quad (2.4)$$

Results presented in the literature only deal with vertically polarized fields, and depolarization of the waves is neglected. Indeed, for *mm-W* it has been shown in [Järveläinen, 2013] where there is only minor coupling between the original and the orthogonal polarization. In this case, (2.4) can be simplified, its form being given by (2.5).

$$h(t,\tau) = \sum_{k=1}^{K} \gamma_{VV,k}(t)\delta(\tau-\tau_k(t)) \quad (2.5)$$

If the *Rx* antenna or *Tx* antenna is moving for a distance *d*, the time variable *t* in (2.5) is replaced by *d*.

2.2.3.2 Wideband Channel Characterization

- **Time Domain Characterization**

The *Power Delay Profile*, (*PDP*), and noted $P(\tau)$ is computed by averaging, spatially or temporally, the channel impulse response, $\overline{|h(d,\tau)|^2}$ over a local area [Rappaport, 1996]:

$$P(\tau) = \overline{|h(d,\tau)|^2} \qquad (2.6)$$

A wideband multipath channel can be described by its dispersion in the delay domain, which is usually expressed in terms of the *RMS* (*Root Mean Square*) *delay Spread*, σ_τ, and of the maximum excess delay [Rappaport, 1996]. The *RMS delay spread* is defined as:

$$\sigma_\tau = \sqrt{\frac{\sum\limits_k P(\tau_k)\tau_k^2}{\sum\limits_k P(\tau_k)} - \left(\frac{\sum\limits_k P(\tau_k)\tau_k}{\sum\limits_k P(\tau_k)}\right)^2} \qquad (2.7)$$

In practice, σ_τ depends on the noise threshold applied to the *PDP* and that which is used to distinguish received multipath components from thermal noise. Typical values of this threshold are between 10–30 dB below the strongest path.

The *maximum excess delay* is defined as the maximum delay between the first and the last arriving multipath component whose amplitudes are greater than a given threshold. It can be written as:

$$MED = \max(\tau_i) - \min(\tau_i) \qquad (2.8)$$

- **Frequency Domain Characterization**

In the frequency domain, the parameter used to quantify the frequency selectivity of the channel is the *coherence bandwidth Bc*. It is a statistical measure of the range of frequencies over which the channel can be considered to have components with approximately equal gain and linear phase. In other words, *coherence bandwidth* is the range of frequencies over which two frequency components have a strong amplitude correlation [Rappaport, 1996]. Hence, the *coherence bandwidth* is deduced from the

autocorrelation of the frequency domain function $H(f)$. If a correlation coefficient of 0.5 is chosen, an empirical relation between Bc and σ_τ has been proposed:

$$B_c = \frac{1}{5\sigma_\tau} \qquad (2.9)$$

For a correlation coefficient of 0.9, the relation between delay spread and coherence bandwidth becomes:

$$B_c = \frac{1}{50\sigma_\tau} \qquad (2.10)$$

There is no specific rule for choosing either a coefficient of 0.5 or 0.9. If the coherence bandwidth is used to define the optimum subcarrier spacing in an *OFDM* system, a coefficient of 0.9 is often considered to fulfill the flat channel condition within a subcarrier. If frequency diversity techniques are considered, the frequency shift between two "uncorrelated" subchannels usually correspond to the coherence bandwidth defined for a correlation coefficient of 0.5.

- **Time variability of the channel**

Doppler Spread and *coherence time* describe the time varying nature of the channel caused by movement in a small-scale region.

If we suppose a mobile receiver moving at a constant speed, v, along a distance, *d*, a phase change is produced in the received signal. This phase change causes a frequency change called *Doppler shift*, v [Rappaport, 1996]:

$$v = \frac{v}{\lambda}\cos\theta \qquad (2.11)$$

where θ is the angle between the direction of motion of the mobile and the direction of the arrival of the waves.

When a mobile radio channel changes with a certain time rate, a spectral broadening is produced. *Doppler spread B_D* is defined as the range of frequencies over which the received *Doppler spectrum* is essentially non-zero. When a pure sinusoidal tone of frequency is transmitted, the received signal spectrum, called the *Doppler spectrum,*

will have components in the range $f_c \pm v$ where f_c is the central frequency. The amount of spectral broadening depends on the relative velocity of the mobile, and on the angle θ. It should be remarked that if the baseband signal bandwidth is much greater than B_D, the effects of *Doppler spread* are negligible at the receiver.

The *coherence time* is inversely proportional to the *Doppler spread* and is a statistical measure of the time duration on which the channel impulse response is invariant. So, it quantifies the similarity of the channel response at different times. The *coherence time* is the time duration on which two received signals are strongly correlated in amplitude. It is often deduced by considering a correlation coefficient of 0.5.

- **Angular Spread**

Another interested parameter is the *RMS angular spread*. In *MIMO* systems it is possible to determine the *Direction of Departure* (*DoD)* or *Angles of Departure* (*AoD*), and *Direction of Arrival* (*DoA*) or *Angles of Arrival* (*AoA*) of the waves. For any angle ϕ_k, the power of the ray being $P(\phi_k)$, the *RMS angular spread* is given by [Fleury, 2000]:

$$\sigma_\phi = \sqrt{\frac{\sum_k P(\phi_k)\phi_k^2}{\sum_k P(\phi_k)} - \left(\frac{\sum_k P(\phi_k)\phi_k}{\sum_k P(\phi_k)}\right)^2} \qquad (2.12)$$

ϕ_k being $\theta_{TX,k}$ $\theta_{RX,k}$ $\varphi_{TX,k}$ $\varphi_{RX,k}$ for the four possible angular spreads. We name these four angles the transmit-elevation, receive-elevation, transmit-azimuth and receive-azimuth.

- **Experimental Results**

Some wideband channel characterization results can be found in [Fu, 2013] and delay spread obtained in an office of 100m² in a *LoS* scenario varies from 5 ns to 80 ns with a mean value of 35 ns. In [Yong, 2007], results are deduced from one measurement campaign covering a range from 1 m to 5 m, the frequency bandwidth being a 3 GHz range centered at 62.5 GHz. In this study, a virtual uniform circular array allowed the estimation of *DoA*. Various antenna patterns are considered, leading to quite different values of angular spread. Even if results of such measurements are interesting, their

interpretation is not obvious because the effect of the radiation pattern of the antennas has not been subtracted.

2.2.3.3 Wideband Channel Modeling

Two main classes of channel model are identified: physical and stochastic (or analytical) models. Figure 2.4 summarizes the classes and associated subclasses described in the next paragraphs.
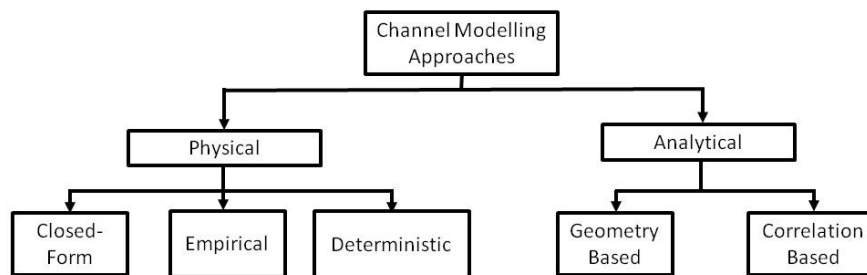
Figure 2.4: Classification of channel modeling approaches.

- **Physical Model**

Physical models describe wireless propagation in terms of parameters having a physical sense. These parameters can describe characteristics of either an individual path or of a subset of paths, as in the case of the *empirical model* of path loss. The *closed-form* approach is also part of physical models, the model matching experimental results obtained in a given environment. However, the parameters introduced in these models must be changed from one scenario to another. Lastly, *deterministic models* include ray tracing, ray launching or *FDTD* (*Finite Difference Time Domain*)-based models. Note that these deterministic models are the most complex and computationally expensive approaches. Their accuracy depends on the topographical database used and on the availability of the materials characteristics of each obstacle in the *mm-W* bandwidth.

In *Appendix A*, detailed information about the *3D ray tracing* developed in the *SiCoMo* research group and available at the beginning of the thesis is given. This model takes reflection into account, but only single diffraction leading to discrepancies between experimental and predicted results in complex environments. Therefore, multiple-diffraction at *mm-W* over several obstacles must be taken into account to fit the model to the "reality" as much as possible.

In this sense, radiowave multiple diffraction has been widely investigated through two-dimensional theoretical models, usually developed within an urban context, with Walfish and Bertoni being the pioneers in proposing a formulation for the prediction of radiowave attenuation in urban environments [Walfish, 1988]. They evaluated the propagation losses in the vertical plane, which contains both the transmitter and the receiver, taking the phenomenon of multiple diffraction – caused by the presence of buildings – into account.

In this model, the path loss is expressed as the summation of three terms (Figure 2.5):

$$L = L_0 + L_{dif} + L_{df} \qquad (2.13)$$

where L_0 is free space path loss, L_{dif} is the additional attenuation due to the multiple diffraction over the buildings, and L_{df} is the diffraction from the last building before reaching the receiver, Rx, located at street level.
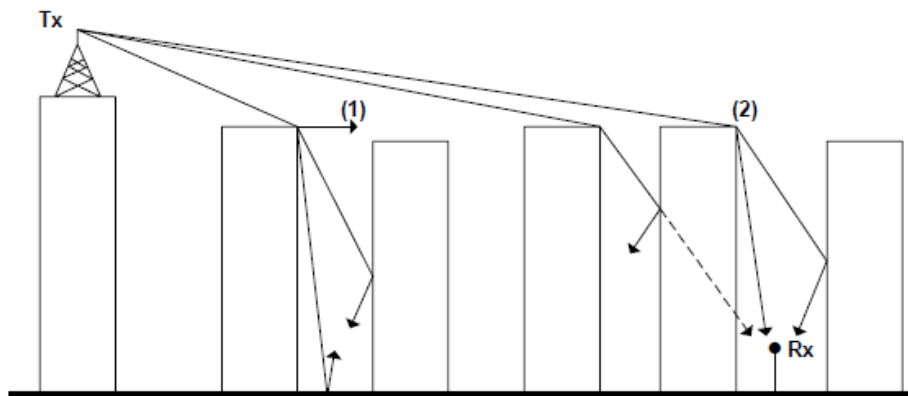
Figure 2.5: Propagation paths in urban environment.

In this sense, a *Uniform Theory of Diffraction* and *Physical Optics (UTD-PO)* formulation for multiple-cylinder and multiple-plateau diffraction is compared with measurements performed at 60 GHz in Chapter 3. The detailed formulation is shown in *Appendix C*.

Lastly, single-order diffuse components have been implemented in the ray tracing tool in order to increase the accuracy of the model [Degli-Esposti, 2007]. This will also be treated in Chapter 4.

- **Analytical Models**

Analytical channel models provide mathematical models for the channel transfer function or the *channel impulse response* (*CIR*) between transmitting antenna(s) and receiving antenna(s). This channel transfer function or *CIR* is a function of one or more independent variables. The *Rayleigh fading channel* is an example of the narrowband analytical model. Stochastic modeling provides a statistical representation of the channel by using numerous measurements. It can be divided in three subgroups (see Figure 2.4): the correlation based model, the *geometry based stochastic model* (*GBSM*), and the *Saleh-Valenzuela (S-V) model*. The correlation-based model uses the channel second-order statistics in order to obtain a generic full correlation model which describes the spatial behavior of a system. *GBSM* simulates the effect of wave propagation by considering scatters distributed between *Tx* and *Rx* and provides information on channel amplitude, phase, angle and time for each path. Finally, the most popular model is the *S-V model* [Saleh, 1987] based on the clustering of rays in both the temporal and spatial domains. This model has been extended to the angular domain by Spencer [Spencer, 2000]. Based on this approach, a generic *mm-W* channel model is proposed in [Yong, 2007] and was later adopted by the *IEEE 802.15.3c* group as the standard model for millimetric band *CIRs*. The channel model relies on two classes of parameters, namely intercluster and intracluster parameters, of *ToA*, *AoA* and *amplitude*.

Identification of clusters (clustering) is a difficult task due to the major problem of cluster parameterization, where the parameters have to be extracted from measurement data. There are some options for clustering, one of which is visual inspection, but this becomes impractical for large amounts of measurement data [Czink, 2006bis]. Another possibility is using the *K-Means algorithm* [Han, 2001] with the *Multipath Component Distance (MCD)* distance [Czink, 2006]. This algorithm is one of the most commonly used clustering algorithms.

In [Czink, 2006bis], a framework is proposed to automatically identify multi-path clusters from *MIMO* channel measurement data. It includes power and *MCD* distance into the *K-means* concept. Another option for obtaining the clusters is detailed in [Gustafson, 2014]. The method consists of sorting the rays with respect to their delays and then grouping rays. In Chapter 4 this problem will be treated both analytically and experimentally.

The extended *S-V model* of *CIR* is given in equation (2.14) [Spencer, 2000]. This expression comes from equation (2.4), where the summation over all paths is grouped into two summations, one dealing the number of clusters *(L)*, and another dealing with the number of rays within each cluster *(Kl)*. The interest of this expression is to separate the contribution of inter-cluster and intra-cluster parameters. Furthermore, the delay and angle random variables are independent and described by the distribution functions given in Table 2.2.

$$h(\tau,\phi) = \sum_{l=1}^{L} \sum_{k=1}^{K_l} \alpha_{k,l} \delta(\tau - T_l - \tau_{k,l}) \delta(\phi - \Theta_l - \varphi_{k,l}) \qquad (2.14)$$

The estimated value of parameters is extracted from one measurement campaign and by using either 30° or 60° *half power beamwidth* (*HPBW*) antennas. However, these results have to be confirmed by extensive measurement campaigns.

CIR parameter		Distribution	Distribution parameter	[Yong, 2007] 30°/60°
T_l	Time arrival of cluster	Poisson	Γ	49.8/38.8
$\tau_{k,l}$	Intra-cluster time of arrival	Poisson	γ	45.2/64.9
Θ_l	Angle of arrival of cluster	Uniform distribution	$[0,2\pi)$	102/66.4
$\varphi_{k,l}$	Angle of arrival of path in a cluster	Laplacian distribution	σ	5/6
$\alpha_{k,l}$	Amplitude of ray (intra-cluster)	$\overline{\alpha_{k,l}^{\;2}} = \overline{\alpha_{0,0}^{\;2}} \cdot e^{-T_l/\Gamma} \cdot e^{-T_k/\gamma}$ α is Rayleigh distributed		

Table 2.2: Wideband Channel model parameters from [Yong 2007].

2.2.4 Issues to be Solved

The interest of the multipath propagation channel model is quite recent. A deterministic approach with accurate description of the environment will help in understanding the cluster approach model and the physical sense to give to clusters in an indoor environment. In this sense, an in-depth knowledge of the clustering issue in the mm-W frequency band is needed, since this structure is generally accepted but it must be verified. Furthermore, the correct implementation of the classical propagation mechanism, such as diffuse scattering according to electrical parameters, must be taken into account.

In addition, the *mm-W* literature focus on *SISO* channel analysis, so a *MIMO* approach could be interesting to fully understand the double directional channel in *mm-W*. The *3D ray tracing* will allow important statistical research by changing the environment characteristics.

In terms of channel characterization, more data is needed at these frequencies. Indeed, in [IEEE 802.15.3, 2009] it was claimed that the number of available measurements on which the model could be based in the 57–64 GHz range as well as the number of available measurement data were insufficient to fully characterize the underlying environments.

In summary, channel modeling and characterization in *mm-W* is now a hot topic, where there is a lack of experimental and theoretical research due to the complexity of the problem. The analysis in space and frequency domain enables us to study completely the double-directional channel. In this sense, it is necessary to analyze the *AoA*, *AoD*, and *ToA* of energy propagation in these bands.

Chapter 3

Radiowave Multiple Diffraction at the mm-wave frequency band

Many radiowave multiple-diffraction investigations have been carried out for current communication systems [Walfisch, 1988] [Juan-Llácer, 1997] [Holm, 1996] [Xia, 1992] [Rodríguez, 2007]. However, to the best of the author's knowledge, not much scientific literature about the diffraction phenomenon in the 60 GHz-frequency band can be found. Only three works, [Maltsev, 2010], [Jacob,2012] and [Kleine-Ostmann, 2012] are in relation with the diffraction study regarding such frequency band.

This chapter deals with the study of the phenomenon of radiowave multiple diffraction under several scenarios and at the frequencies corresponding to the *mm-wave* band.

Firstly, in Section 3.1, a hybrid uniform theory of diffraction-physical optics (*UTD-PO*) formulation for the analysis of multiple-diffraction of spherical waves by a series of rectangular plateaux is compared with measurements performed at 62 GHz.

Secondly, in section 3.2, a *UTD-PO* theoretical formulation for the analysis of the multiple-diffraction of spherical waves by a series of cylinders is compared with measurements carried out at 60 GHz.

Next, a comparison of the presence of cylindrical against rectangular obstacles in radio wave multiple-diffraction, at *mm-W* frequencies is detailed in Section 3.3, both theoretically and experimentally.

Finally, in Section 3.4, a new method based on a *UTD-PO* formulation for the analysis of the propagation loss due to the diffraction that takes place at the top of a rectangular obstacle that is illuminated from a low source (i.e., the transmitter height is smaller than the obstacle height) is validated through measurements performed at 60 GHz.

The main conclusions deduced from the work presented in this chapter are outlined in section 3.5.

3.1 Modeling of Obstacles as Dielectric Rectangular Plateaux

In this section, the aim is to compare the theoretical formulation for the analysis of multiple-diffraction of spherical waves by a series of rectangular plateaux with measurements performed at 62 GHz.

3.1.1 Introduction

Radiowave multiple-diffraction over an array of obstacles has been studied using many formulations, which are normally proposed within an urban propagation context and usually assume such obstacles (buildings) to be modeled as knife edges [Xia, 1992], [Zhang, 1995] or wedges [Kara, 2002], [Juan-Llácer, 2002]. However, less attention has been focused on the analysis of multiple-diffraction when the diffracting elements are considered to be modeled as rectangles, which could be more appropriate in order to obtain more accurate and realistic signal strength predictions when the obstacles present

such rectangular shapes (plateaux). In this case, some solutions for urban environments, based on the *uniform theory of diffraction* (*UTD*) [Erricolo, 2001], the parabolic equation method [Janaswamy, 2000], or a hybrid *UTD-physical optics (PO)* approach that assumes a plane-wave incidence [Rodríguez, 2005], have been proposed.

On the other hand, since the 60 GHz-frequency band has captured the interest of researchers due to the large bandwidth available [Jay, 2009] and the small frequency reuse distance offered [Smulders, 2002], the phenomenon of radiowave diffraction has been recently studied at the mm and sub-mm band in [Jacob, 2012].

This section presents the comparison of a hybrid *UTD-PO* formulation for the analysis of multiple-diffraction by a series of plateaux -–which assumes spherical-wave incidence—with measurements performed at 62 GHz.

3.1.2 Theoretical Model

An idealized representation of the considered propagation environment can be observed in Figure 3.1, where *n* rectangular plateaux of the same height, which is relative to the transmitter antenna height *H*, have been taken into account, assuming that they have the same thickness *v* and a constant inter-plateau spacing *w*.
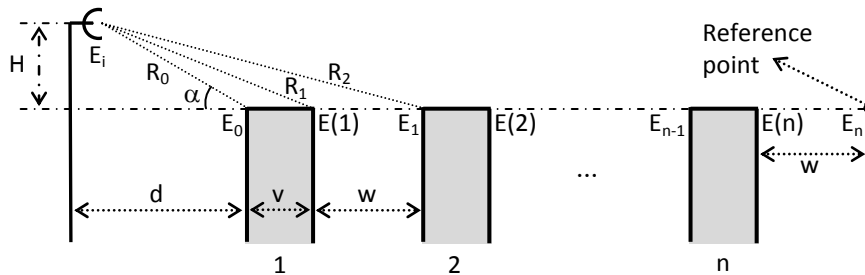
Figure 3.1: Scheme of the propagation environment considered.

The transmitting point is assumed to be located above or level with the average rooftop height ($H \geq 0$) and at a certain distance *d* from the array of obstacles (spherical-wave incidence). For multiple-diffraction analysis purposes, this configuration can be considered as a series of wedges of interior angle $\pi/2$ radians, joined two by two, forming the flat-roofed obstacles, as Figure 3.2 shows.

Figure 3.2: Rectangular obstacle seen as a combination of two joined wedges of interior angle π/2 rad.

In this sense, the total field that reaches the reference point indicated in Figure 3.1 is computed by considering the recursive *UTD-PO* solution explained in *Appendix C*. In this way, taking into account that the field that reaches the left wedge forming the rooftop of the first obstacle E_0 is:

$$E_0 = \frac{E_i}{R_0} \exp(-jkR_0) \qquad (3.1)$$

where E_i is the relative amplitude of the spherical source and k is the wave number.

Thus, the total field that reaches the reference point indicated in Figure 3.1, located at a distance w from the last plateau, can be expressed, assuming $\alpha \geq 0$, for $n \geq 1$, as

$$
\begin{aligned}
E_n = \frac{1}{2n} &\left\{ \sum_{q=0}^{n-1} E_q \left[\frac{R_0}{R_{2(n-q)}} \exp\left[-jk(R_{2n} - R_{2q}) \right] \right.\right. \\
&+ \sqrt{\frac{R_0}{(n-q)(v+w)[R_0 + (n-q)(v+w)]}} \\
&\left. \cdot D\left(\phi' = \frac{\pi}{2} + \alpha, \phi = \frac{3\pi}{2}, L = \sqrt{\frac{R_0(n-q)(v+w)}{R_0 + (n-q)(v+w)}} \right) \cdot \exp\left[-jk(n-q)(v+w) \right] \right] \\
&+ \sum_{r=1}^{n} E(r) \left[\frac{R_0}{R'_{2(n-r)+1}} \exp\left[-jk(R_{2n} - R_{2r-1}) \right] + \sqrt{\frac{R_0}{[(n-r)(v+w)+w][R_0 + (n-r)(v+w)+w]}} \right. \\
&\left.\left. \cdot D\left(\phi' = \alpha, \phi = \pi, L = \sqrt{\frac{R_0[(n-r)(v+w)+w]}{R_0 + [(n-r)(v+w)+w]}} \right) \cdot \exp\left[-jk[(n-r)(v+w)+w] \right] \right] \right\} \quad (3.2)
\end{aligned}
$$

where $D(\phi, \phi', L)$ is the diffraction coefficient for a finitely conducting wedge, as given in [Luebbers, 1984a],

$$R_x = \begin{cases} \sqrt{\left[d + \dfrac{x}{2}(v+w)\right]^2 + H^2}, & x \quad even \\[2em] \sqrt{\left[d + \dfrac{x-1}{2}(v+w)+v\right]^2 + H^2}, & x \quad odd \end{cases} \qquad (3.3)$$

$$R_x' = \sqrt{\left[d + \frac{x-1}{2}(v+w)+w\right]^2 + H^2} \quad (3.4)$$

and *E(n)* is the field reaching the corners on the right of the rooftops, as observed in Figure 3.1:

$$E(n) = \frac{1}{2n-1}\left\{ \sum_{m=0}^{n-1} E_m \left[\frac{R_0}{R_{2(n-m)-1}} \exp\left[-jk(R_{2n-1}-R_{2m})\right] \right.\right.$$

$$+ \sqrt{\frac{R_0}{[(n-m)(v+w)-w][R_0+(n-m)(v+w)-w]}}$$

$$\cdot D\left(\phi'=\frac{\pi}{2}+\alpha, \phi=\frac{3\pi}{2}, L=\sqrt{\frac{R_0[(n-m)(v+w)-w]}{R_0+[(n-m)(v+w)-w]}}\right) \cdot \exp\left[-jk[(n-m)(v+w)-w]\right]\right]$$

$$+ \sum_{p=1}^{n-1} E(p)\left[\frac{R_0}{R_{2(n-p)}} \exp\left[-jk(R_{2n-1}-R_{2p-1})\right] + \sqrt{\frac{R_0}{(n-p)(v+w)[R_0+(n-p)(v+w)]}} \right.$$

$$\left.\left. \cdot D\left(\phi'=\alpha, \phi=\pi, L=\sqrt{\frac{R_0(n-p)(v+w)}{R_0+(n-p)(v+w)}}\right) \cdot \exp\left[-jk(n-p)(v+w)\right]\right]\right\} \quad (3.5)$$

It should be noted that, with this theoretical formulation, the analysis of multiple-plateau diffraction with an angle of incidence smaller than zero ($\alpha < 0$) could not be carried out, since, in this case, the impinging wave front would hit the wedges that form the corners on the right of the rectangular obstacles from inside the plateaux, which is meaningless for this purpose. On the other hand, it should also be pointed out that, although multiple transition region diffraction is implicit in the environment under study (Figure 3.1) and that implies, in a *UTD* context, the consideration of *slope diffraction* (high-order diffraction terms) [Capolino, 1997], [Erricolo, 2002], [Tabakcioglu,2009], [Andersen,1997] , [Tabakcioglu, 2010] , [Holm, 2000], this *UTD-PO* solution does not need to incorporate it, due to the recursive relation in which only single diffractions are involved in the calculations.

3.1.3 Measurement Setup

The channel sounder employed is based on the channel sounder detailed in *Appendix B*. For this measurement campaign, the scheme is depicted in Figure 3.3.
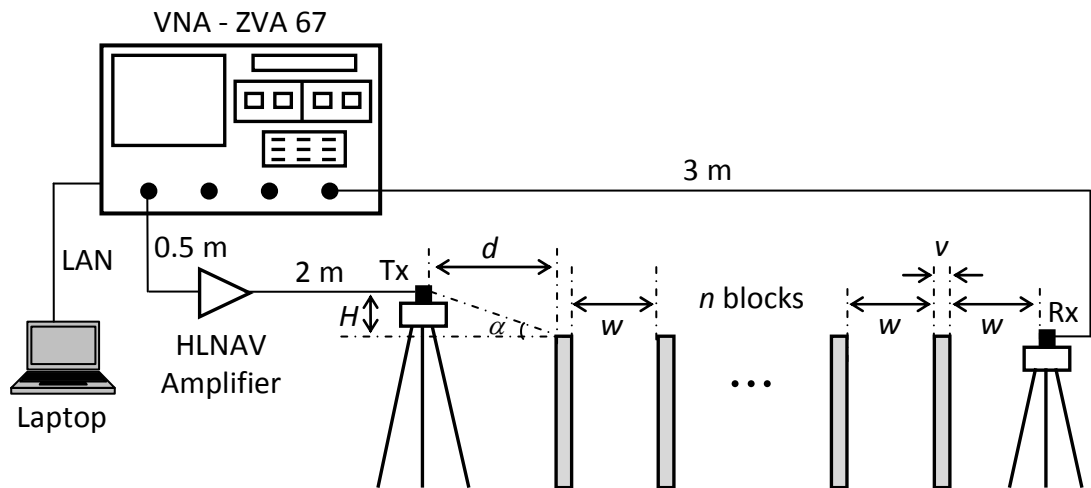
Figure 3.3: Scheme of the measurement setup.

As can be observed in Figure 3.3, the receiving antenna (*Rx*) is directly connected to one port of the vector network analyzer (*VNA)* through a 3 m coaxial cable, while the signal of the transmitter port of the *VNA* is first amplified and then connected to the transmitting antenna (*Tx*) through a 2 m coaxial cable (the amplifier is, moreover, connected to the *VNA* through a 0.5 m coaxial cable). Both antennas are omnidirectional antennas *Q-par QOM55-65 VRA*.

Measurements were performed for four cases: $n = 4$ (for $d = 0.10$ m and $d = 0.20$ m) and $n = 6$ (for $d = 0.10$ m and $d = 0.20$ m). Figure 3.4 shows the photos of the scenario.

a)   b)

Figure 3.4: Photos a) Scenario for n=4 rectangular obstacles and b) Scenario for n=6 rectangular obstacles.

For d = 0.20 m, the transmitting antenna height was varied from 0 m to 0.03 m and, for d = 0.10 m, from 0 m to 0.02 m, both cases in steps of 0.005 m. In such a way, the incident angle α has a maximum value of about 8° and 11°, respectively, which should be large enough for multiple-diffraction considerations.

The *channel frequency response* (*G*) was measured over 301 frequency points, equally spaced between 60 and 64 GHz, leading to a frequency step of 13.3 MHz and resolution time of 0.3 ns (0.10 m), while being 1 Hz the *intermediate frequency*.

Since the theoretical model for multiple-diffraction analysis stated in the previous part is a *2D* approach and, as mentioned before, the considered antennas are omnidirectional (the energy is captured from all directions of the measurement environment), the results of the measurements were processed so that wave propagation was only considered along the vertical plane in which the transmitter and the receiver were aligned, considering the first contribution and cancelling the rest of them. To do so, the *time-gating* technique was applied for measurements taken both with and without blocks (rectangular plateaux), as can be observed in Figure 3.5, where an example of the time-domain measurement for H = 0 m, d = 0.10 m and the cases of n = 4 and free space (without blocks) is depicted.
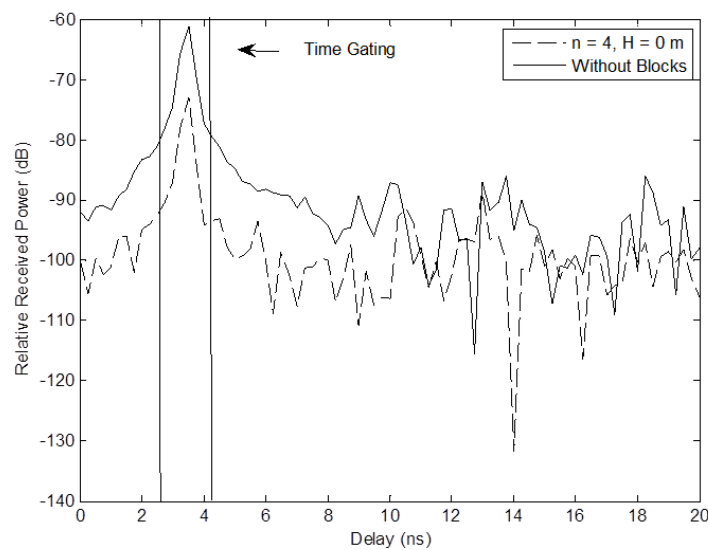
Figure 3.5: Example of the *time-gating* technique applied. In this case, H = 0 m, d = 0.10 m, and the cases of n = 4 and free space (without blocks) are depicted.

Therefore, the methodology used to obtain the desired contributions for attenuation calculation due to multiple-diffraction was as follows:

a) The frequency-domain G was transformed into the time-domain via *inverse fast Fourier transform* (*IFFT*) and converted into the power delay profile (*PDP*):

$$PDP(\tau) = |h(\tau)|^2 = |ifft(G(f))|^2 \quad (3.6)$$

b) Then, the desired contribution was windowed, obtaining the time gated (*TG*) response $PDP_{TG}(\tau)$.

c) Finally, the time-domain mean path loss in logarithmic units was calculated from the *PDP* as [Molina-Garcia-Pardo, 2004]:

$$L = -10\log_{10}\sum_{i=0}^{\infty}PDP_{TG}(\tau_i) \quad (3.7)$$

Hence, the attenuation due to multiple-diffraction (A) is obtained by the difference (in dB) between the path loss existing in the presence of the plateaux (L_p) and that calculated in free space (without the rounded obstacles), (L_{fs}):

$$A = L_p - L_{fs} \quad (3.8)$$

Furthermore, since 301 frequency points were selected, a maximum delay of 75.2 ns (22.5 m) could be measured, not having time-aliasing in the domain (the maximum dimension of the measurement environment is 7 m).

On the other hand, it can be noted that each frequency sweep took around 10 minutes, and nobody was inside the measuring environment during the measurement process, so the channel can be considered as stationary. Moreover, in order to obtain the results shown in the next section, all measurements for all cases were repeated 5 times and properly averaged for statistical purposes.

3.1.4 Results

In Figure 3.6 and Figure 3.7, the results for the attenuation as a function of H at the reference point of Figure 3.1—relative to the free-space field strength—calculated with the proposed *UTD-PO* formulation for a series of plateaux ($n = 4$ and $n = 6$) are compared with the measurements performed at 62 GHz, considering $d = 0.20$ m and $d = 0.10$ m, respectively.

Furthermore, a *hard/vertical* polarization was considered in both cases, assuming $w=0.20$ m, $v=0.02$ m, and rectangular blocks made of granite (with a *complex permittivity* of 4.85–1.42j at 62 GHz [Akeyama, 2005]).
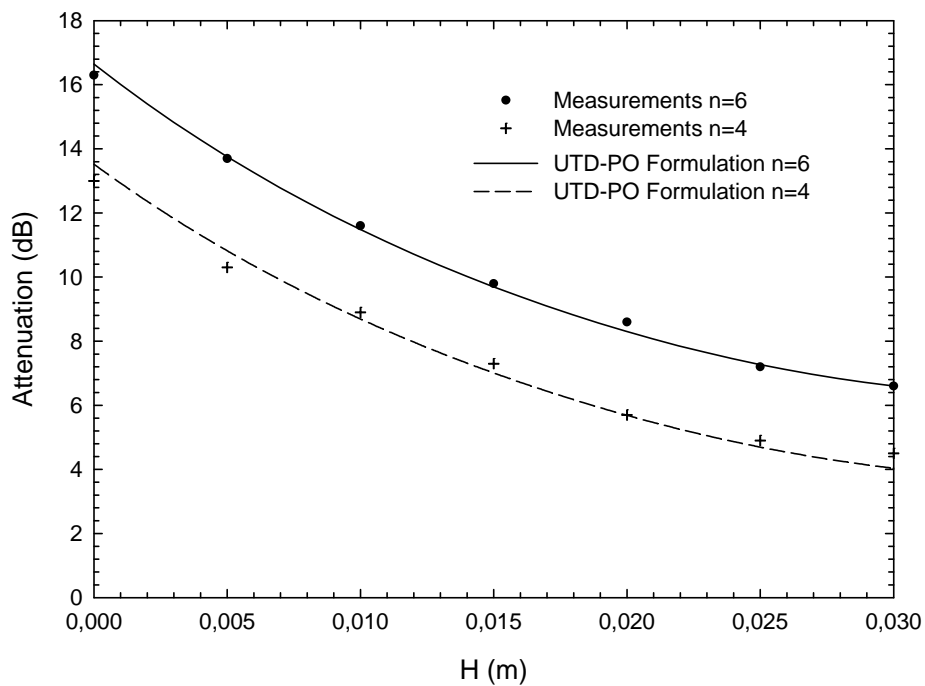
Figure 3.6: Comparison of the UTD-PO formulation results with the measurements at 62 GHz. $d = 0.20$ m, $w = 0.20$ m, $v = 0.02$ m, and *hard/vertical* polarization.
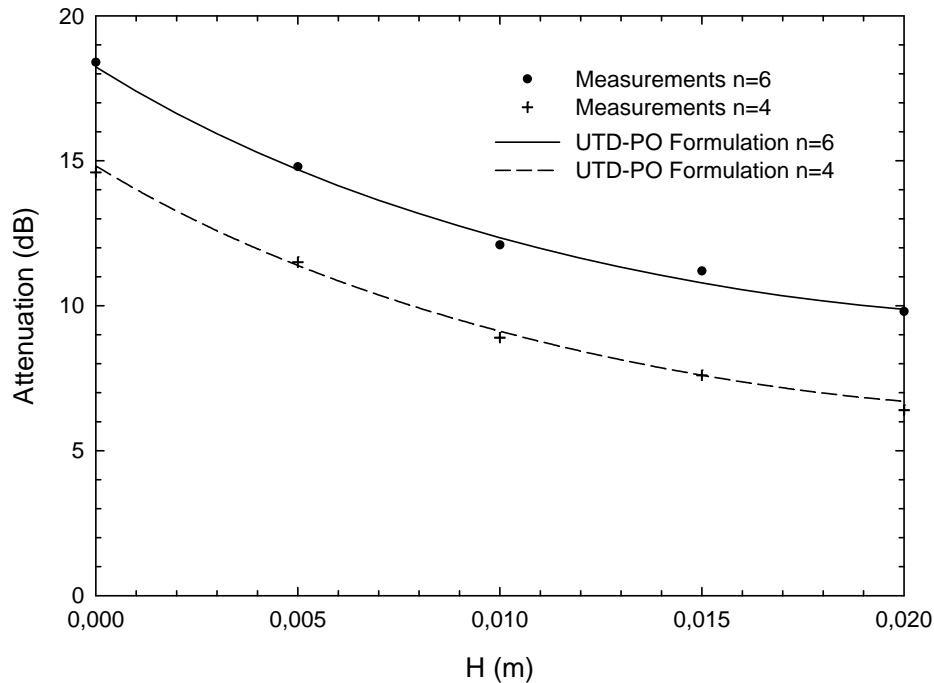
Figure 3.7: Comparison of the UTD-PO formulation results with the measurements at 62 GHz.
$d = 0.10$ m, $w = 0.20$ m, $v = 0.02$ m, and *hard/vertical* polarization.

As it can be observed, an excellent agreement is obtained between the measurements and the prediction achieved by the *UTD-PO* solution for both values of *n* and *d*. In this sense, Table 3.1 shows the mean and the variance of the error in *dB* between the theoretical model and the empirical values. It can be noted how such statistical parameters exhibit a very small error between the *UTD-PO* formulation and the measured results.

	Mean Error	**Variance**
n=4 (d=0.10 m)	0.27	0.05
n=4 (d=0.20 m)	0.19	0.03
n=6 (d=0.10 m)	0.27	0.02
n=6 (d=0.20 m)	0.30	0.04

Table 3.1: Mean and variance of the error between the *UTD-PO* Model and the measurements (dB).

Moreover, since the series of rectangular obstacles can be assumed as a scaled-model of an urban environment, the validity of the *UTD-PO* solution for urban path loss evaluation can also be determined, as shown in other works such as [Erricolo, 2002bis], where the method for urban propagation analysis proposed in [Erricolo, 2001] is validated through measurements on scaled-models performed at 25 GHz in this case.

3.1.5 Conclusions

A comparison between results obtained by a hybrid *UTD-PO* formulation for the analysis of multiple-plateau diffraction and measurements performed at 62 GHz has been presented. A solid agreement has been found between predicted and measured attenuation values. Therefore, since the series of rectangular blocks can be assumed as scaled-models of an urban environment, the proposed *UTD-PO* formulation could be applied in the analysis of urban radiowave propagation.

3.2 Modeling of Obstacles as Perfectly Conducting Cylinders

The goal of this section is to compare the theoretical formulation for the analysis of multiple-diffraction of spherical waves by a series of cylinders with measurements performed at 60 GHz.

In addition, the influence of the variation of parameters, such as: the number of cylinders considered, the radius of curvature, the distance from the transmitter to the array of rounded obstacles, and the polarization is analyzed both theoretically and experimentally in order to evaluate the impact of such parameters on radiowave propagation losses.

3.2.1 Introduction

In order to analyze *radiowave multiple-diffraction* over rounded shapes (mountains, hills, or other rounded surfaces), proper model shapes such as cylinders, rather than knife-edges or wedges, can be more realistic in order to obtain more accurate results, as shown in [Koutitas, 2006]. Thus, a hybrid *UTD-PO* formulation for multiple-cylinder diffraction analysis was recently proposed [Rodríguez, 2008].

Such formulation overcomes the need for the incorporation of the *slope diffraction* mechanism, which is present in [Koutitas, 2006] (consideration of high-order diffraction terms), thanks to a recursive relation in which only single diffractions are involved in the calculations; therefore producing an easier, faster solution.

In the following subsections, the *UTD-PO* formulation for the analysis of the multiple-diffraction of spherical waves over a series of cylinders, given in [Rodríguez, 2008], is validated through measurements performed at 60 GHz

3.2.2 Theoretical Model

In Figure 3.8, a schematic of the considered propagation environment is depicted. A series of *n* perfectly conducting cylinders of the same height (relative to the transmitter antenna height *H*), constant inter-cylinder spacing *w*, and the same radius of curvature *r*, have been taken into account. Additionally, the source is at an arbitrary height (above, level with, or below the average cylinder height), and is located at a certain distance *d* from the array of cylinders.
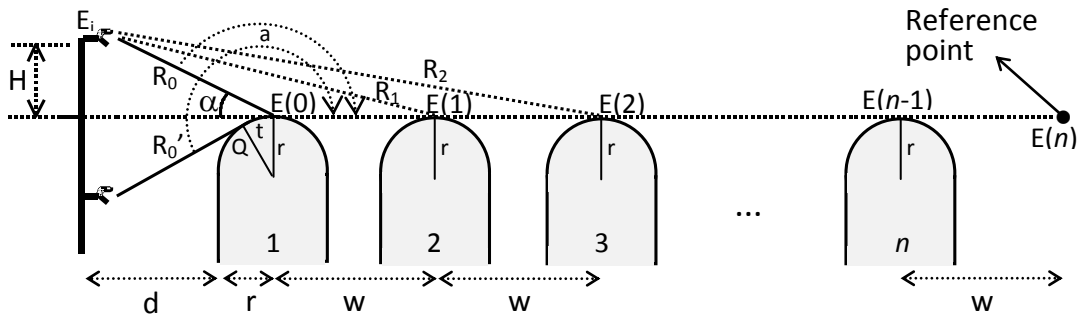
Figure 3.8: Schematic of the considered propagation environment.

In this sense, the field reaching the reference point indicated in Figure 3.8 can be obtained by the final solution presented in *Appendix C*.

If we first consider the base station antenna above the average rooftop height ($H \geq 0$), when $n = 0$ (absence of cylinders), the observed field at the reference point in Figure 3.8 (the field that impinges on the first cylinder) can be expressed as

$$E_0 = \frac{E_i}{R_0} \exp(-jkR_0) \qquad (3.9)$$

where E_i is the relative amplitude of the spherical source and k is the wave number.

Thus, the total field that reaches the reference point indicated in Figure 3.8 (for $n > 1$,), considering the far-field approximation by which $d >> r$, $w >> r$, $d >> t$, $w >> t$, can be expressed as follows.

a) Transmitting point above or level with the average cylinder height ($H \geq 0$, $\alpha \geq 0$)

$$E(n) = \frac{1}{n} \sum_{m=0}^{n-1} E(m) \left[\frac{R_0}{R_{n-m}} e^{-jk(R_n - R_m)} + \sqrt{\frac{R_0}{(n-m)w[R_0 + (n-m)w]}} R_{s,h}(a) e^{-jk(n-m)w} \right] \quad (3.10)$$

b) Transmitting point below the average cylinder height ($H < 0$, $\alpha < 0$)

$$E(n) = \frac{1}{n} \sum_{m=0}^{n-1} E(m) \sqrt{\frac{R_0'}{(n-m)w[R_0' + (n-m)w]}} T_{s,h}(a) e^{-jk(n-m)w} \quad (3.11)$$

being that in this case

$$E(0) = \frac{E_i}{R_0'} \sqrt{\frac{R_0'}{R_0' + t(a)}} e^{-jkR_0'} e^{-jkt(a)} \approx \frac{E_i}{R_0'} e^{-jkR_0'} e^{-jkt(a)} \quad (3.12)$$

and

$$T_{s,h}(a) = -m' \sqrt{\frac{2}{k}} e^{-j\frac{\pi}{4}} \left\{ \frac{-F[X(a)]}{2\varepsilon(a)\sqrt{\pi}} + \left[\begin{array}{c} p*(\varepsilon(a)) \\ q*(\varepsilon(a)) \end{array} \right] \right\} \quad (3.13)$$

is the diffraction coefficient for both *soft* (s) and *hard (h)* polarizations, where

$$X(a) = \frac{kL(a-\pi)^2}{2}$$
$$L = \frac{R_0'(n-m)w}{R_0' + (n-m)w} \quad (3.14)$$
$$\varepsilon(a) = m'(a-\pi)$$
$$t(a) = r(a-\pi)$$

It should be noted that, in (3.11), the term which refers to the direct rays in (3.10) does not appear. Furthermore, for cylinders with very small values of radius of curvature, the presented solution perfectly converges with that given in [Rodríguez, 2007] regarding multiple diffraction over a series of knife edges.

3.2.3 Measurement Setup

The channel sounder used in this section is shown in Figure 3.9.
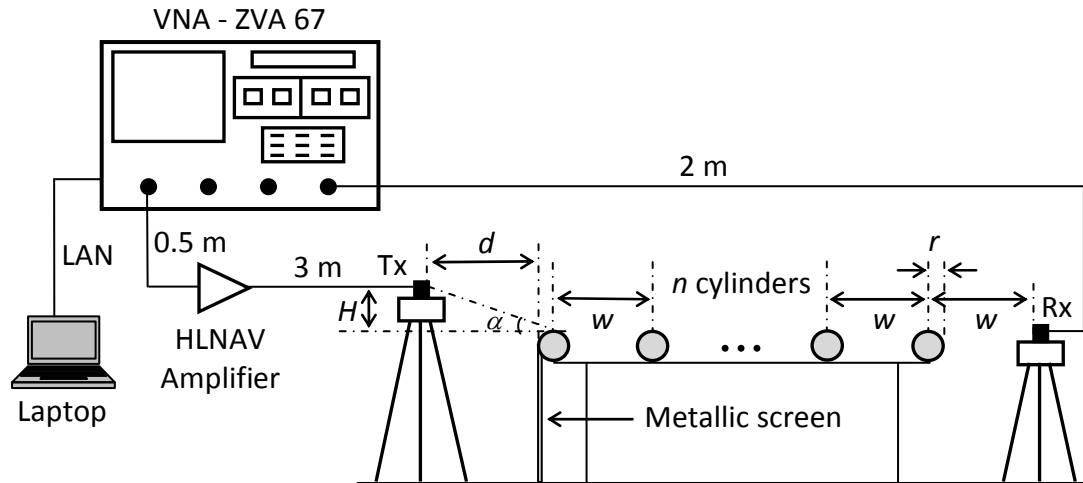
Figure 3.9: Schematic of the measurement setup.

As in the previous scheme, the receiving antenna (*Rx*) is directly connected to one port of the *VNA* through a 2 m coaxial cable. The signal of the transmitter port of the *VNA* is first amplified and then connected to the transmitting antenna (*Tx*) through a 3 m coaxial cable (the amplifier is, moreover, connected to the *VNA* through a 0.5 m coaxial cable).

For more details about the channel sounder, see *Appendix B*.

Measurements were performed for three different values of *n* (number of cylinders), two values of *r* (radius of curvature of the cylinders), both *hard/vertical* and *soft/horizontal* polarizations, and two different values of *d* (distance from the transmitter to the series of cylinders): *d* = 0.10 m and *d* = 0.20 m. Therefore, the previously mentioned parametric study led to 24 different scenarios in which the multiple-diffraction attenuation due to the presence of the array of cylinders was obtained as a function of *H* (transmitting antenna height). When *d* = 0.20 m was considered, the transmitting antenna height was varied from -0.02 m to 0.02 m, and for *d* = 0.10 m, from -0.01 m to 0.01 m; for both cases in steps of 0.0025 m. Therefore, the incident angle *α* has a maximum value of around 5.2° (and -5.2° for *H* < 0) for the evaluated results, which should be large enough for multiple-diffraction considerations. Furthermore, a metallic screen was located at the position of the first cylinder in order to eliminate any contribution coming from below the array of

rounded obstacles, as can be observed in Figure 3.9. Figure 3.10 shows photos of the scenario.

a)   b)
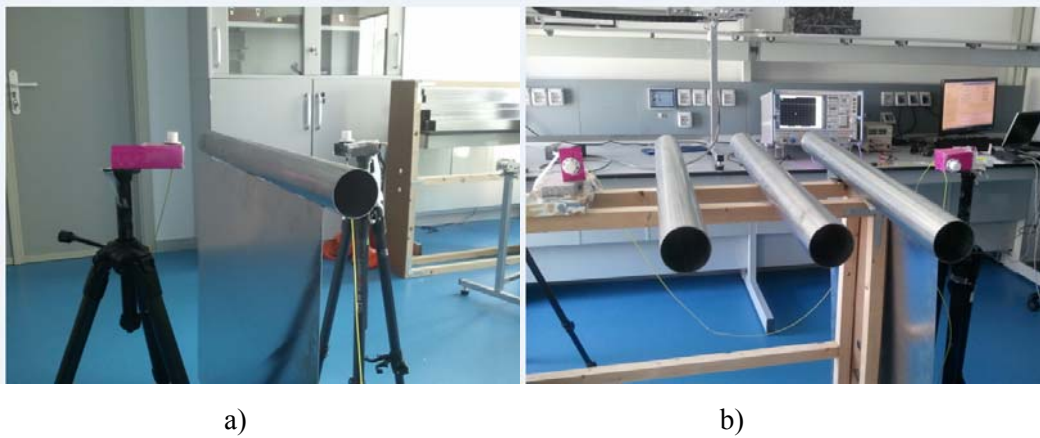
Figure 3.10: Photos a) Scenario for n=1 cylinder obstacle and b) Scenario for n=3 cylinder obstacles.

The *channel frequency response* was measured over 301 frequency points, equally spaced between 58 and 62 GHz, leading to a frequency step of 13.3 MHz, with 1 Hz being the *intermediate frequency*. These values were chosen in order to have a resolution time of 0.25 ns (0.075 m), and to be able to perform the *time-gating* technique, which was explained in 3.1.3.

The attenuation due to multiple-diffraction (*A*) is obtained by the same way that in 3.1.3; the attenuation is the difference (in dB) between the path loss existing in the presence of the cylinders (*Lc*) and that calculated in free space (without the rounded obstacles), (*Lfs*):

$$A = L_c - L_{fs} \qquad (3.15)$$

being *Lc*

$$L_c = -10\log_{10}\sum_{i=0}^{F}PDP_{TG}(\tau_i) \qquad (3.16)$$

For more details, see 3.1.3.

Furthermore, a maximum delay of 75.2 ns (22.57 m) could be measured due to 301 frequency points were selected, without having time-aliasing in the domain (the maximum dimension of the measurement environment is 7 m).

On the other hand, in subsection 3.1.3, each frequency sweep took around 5 minutes, and nobody was inside the measuring environment during the measurement process and thus, the channel can be considered as stationary. Each different scenario (out of the 24 considered) took around 3 hours to be measured, considering calibration and measurements with and without cylinders.

3.2.4 Results

The results for the attenuation as a function of H at the reference point of Figure 3.8, relative to the free-space field strength, can be observed in Figures 3.11 to 3.14, in which both the theoretical predictions calculated with the *UTD-PO* formulation and the measurements performed at 60 GHz are depicted. Three different values of n, the number of perfectly conducting cylinders ($n = 1$, $n = 3$, and $n = 5$) have been considered in the four figures, as well as two different radio of curvature ($r = 0.02$ m and $r = 0.04$ m). Furthermore, constant inter-cylinder spacing of $w = 0.232$ m has been assumed in each case.
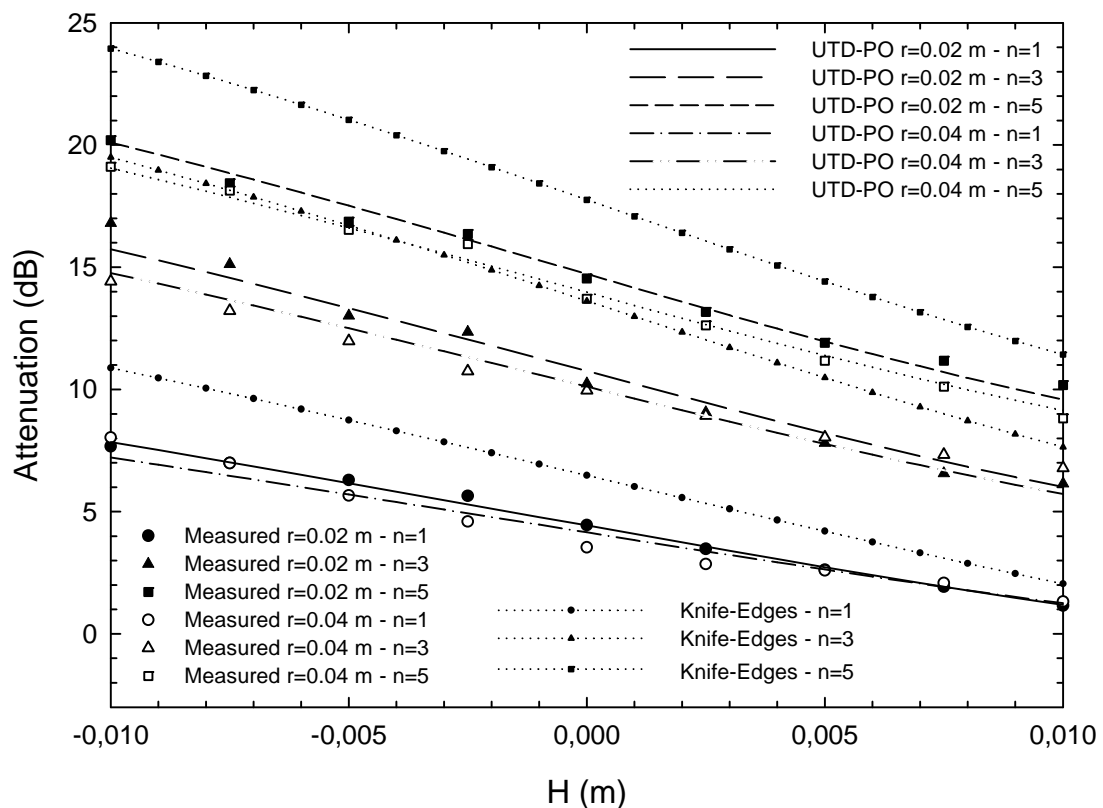
Figure 3.11: Comparison of the UTD-PO formulation results with the measurements at 60 GHz. $w = 0.232$ m, $d = 0.10$ m, and *hard/vertical* polarization.
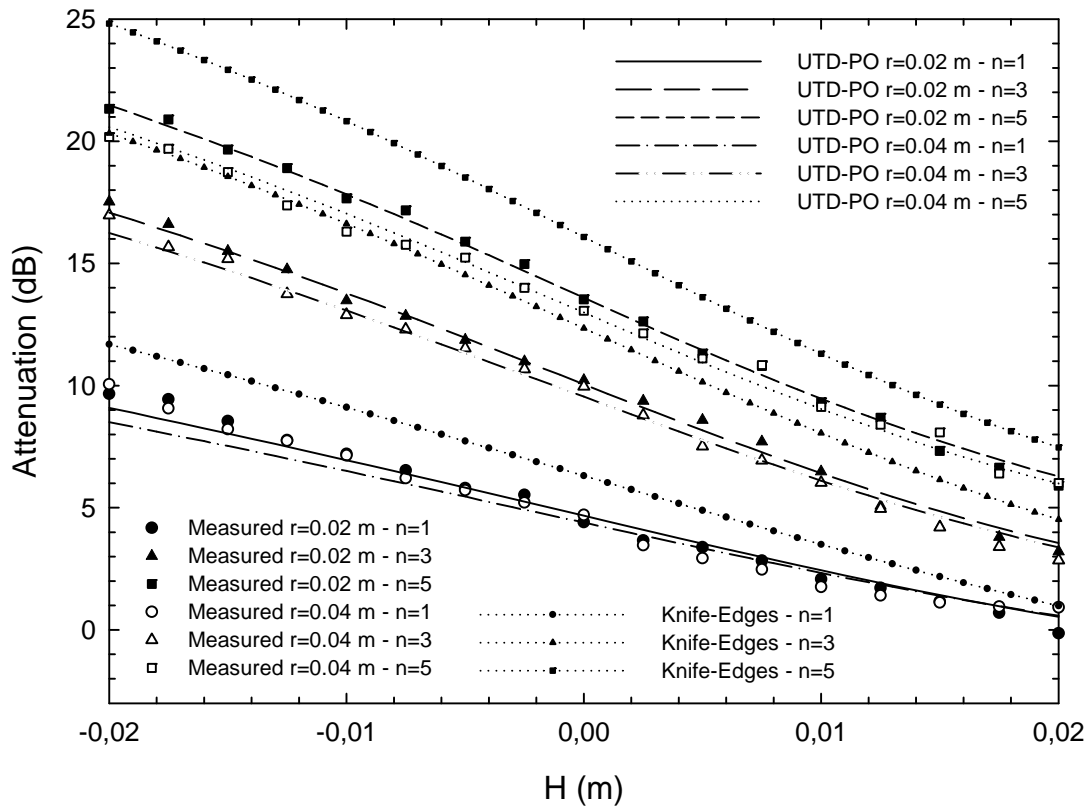
Figure 3.12: Comparison of the UTD-PO formulation results with the measurements at 60 GHz. $w = 0.232$ m, $d = 0.20$ m, and *hard/vertical* polarization.
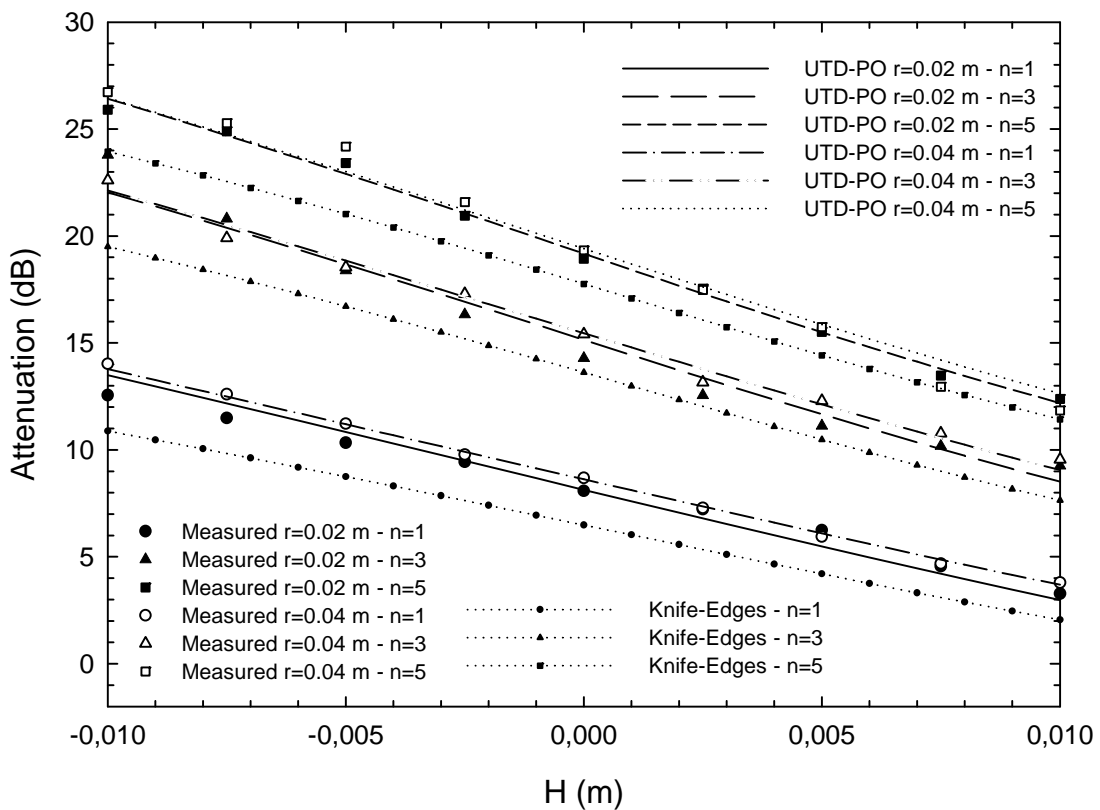
Figure 3.13: Comparison of the UTD-PO formulation results with the measurements at 60 GHz. $w = 0.232$ m, $d = 0.10$ m, and *soft/horizontal* polarization.
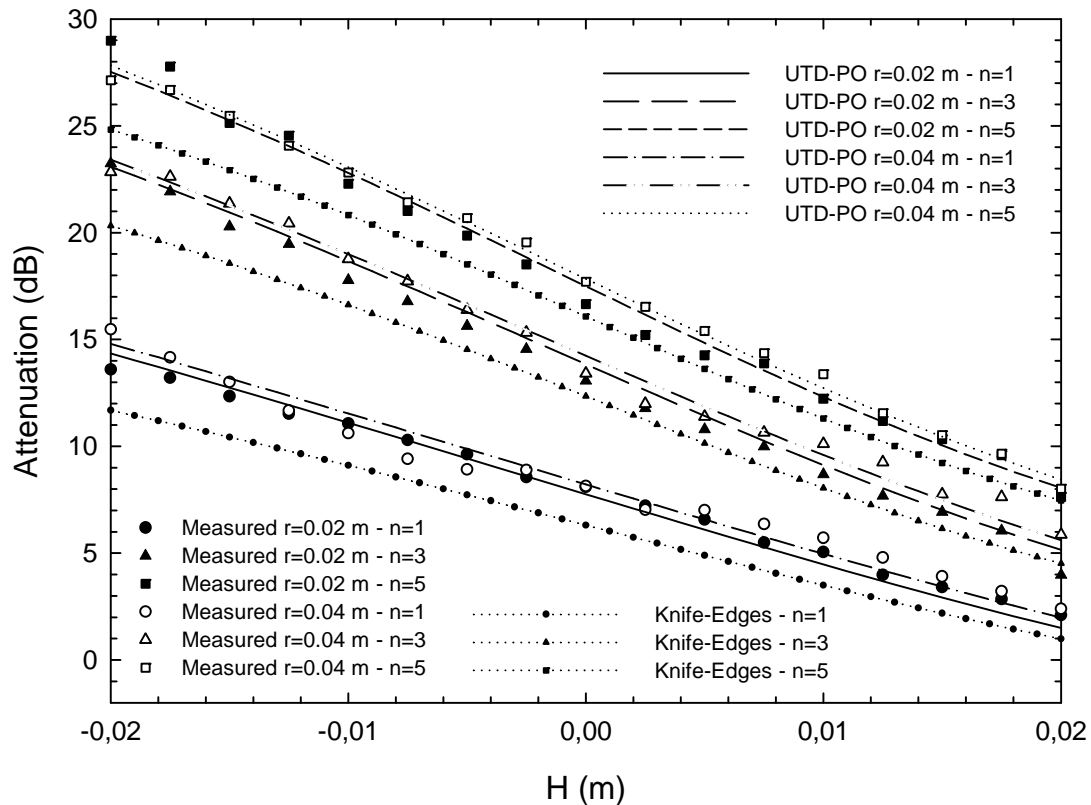
Figure 3.14: Comparison of the UTD-PO formulation results with the measurements at 60 GHz. $w = 0.232$ m, $d = 0.20$ m, and *soft/horizontal* polarization.

In Figures 3.11 and 3.12, the results for *hard/vertical* polarization, considering $d = 0.10$ m and $d = 0.20$ m, respectively, are shown. In Figures 3.13 and 3.14, the attenuation results for *soft/horizontal* polarization are depicted for $d = 0.10$ m and $d = 0.20$ m, respectively. For comparison purposes, the curves corresponding to the cases where the cylinders are substituted by knife-edges are also shown in the plots (such curves have been obtained through the formulation presented in [Rodríguez, 2007]).

As can be observed, a solid agreement is obtained in the four figures between the theoretical predictions achieved by the *UTD-PO* formulation and the measurements. In order to quantify such agreement, Tables 3.2 and 3.3 show the *mean* and the *variance* of the error in dB between the theoretical solution and the empirical values, for *hard/vertical* and *soft/horizontal* polarization, respectively.

	r=0.02 m		r=0.04 m	
	Mean Error	**Variance**	**Mean Error**	**Variance**
n=1 (**d=0.10 m**)	0.69	0.200	0.34	0.073
n=1 (**d=0.20 m**)	0.33	0.043	0.50	0.121
n=3 (**d=0.10 m**)	0.46	0.059	0.44	0.085
n=3 (**d=0.20 m**)	0.26	0.035	0.29	0.036
n=5 (**d=0.10 m**)	0.31	0.044	0.21	0.033
n=5 (**d=0.20 m**)	0.21	0.013	0.29	0.068

Table 3.2: *Mean* and *Variance* of the error between the *UTD-PO* results and the measurements (dB). Vertical polarization.

	r=0.02 m		r=0.04 m	
	Mean Error	**Variance**	**Mean Error**	**Variance**
n=1 (**d=0.10 m**)	0.71	0.168	0.12	0.004
n=1 (**d=0.20 m**)	0.48	0.205	0.54	0.100
n=3 (**d=0.10 m**)	0.68	0.193	0.34	0.039
n=3 (**d=0.20 m**)	0.97	0.377	0.42	0.103
n=5 (**d=0.10 m**)	0.25	0.024	0.52	0.179
n=5 (**d=0.20 m**)	0.54	0.153	0.25	0.041

Table 3.3: *Mean* and *Variance* of the error between the *UTD-PO* results and the measurements (dB). Horizontal polarization.

It should be noted how such statistical parameters exhibit a relatively small error between the *UTD-PO* solution and the measurements for all the cases considered.

Regarding the parametric analysis, the following conclusions can be drawn in view of Figures 3.11 to 3.14:

a) *Variation of the radius of curvature of the cylinders (r).*

For a given *n*, the radius of curvature of the cylinders seems to have little impact on the attenuation results, although its influence is higher at negative angles of incidence (*H* < 0) for *hard/vertical* polarization (up to 1.04 dB of difference), and at positive angles of incidence (*H* > 0) for *soft/horizontal* polarization (up to 0.7 dB of difference). The smaller radius leads to slightly greater values of attenuation, at a certain *n*, when *hard/vertical* polarization is considered, while the opposite occurs for *soft/horizontal* polarization.

b) *Variation of the numbers of cylinders (n).*

As expected, the higher the number of cylinders considered, the greater the multiple-diffraction attenuation obtained. The influence of the variation of the parameter *n* is more significant at negative angles of incidence, where a greater difference is observed between *n* = 1 and *n* = 3 (maximum difference of 8.5 dB) than between *n* = 3 and *n* = 5 (maximum difference of 4 dB).

c) *Variation of the distance between the transmitter and the series of cylinders (d).*

As mentioned in the previous section, because parameter *H* was considered from -0.02 m to 0.02 m when *d* = 0.20 m, and from -0.01 m to 0.01 m for *d* = 0.10 m, the incident angle α had the same maximum value of 5.2° (and -5.2° for *H* < 0) for the two considered values of the distance between the transmitter and the cylinders. However, the curves corresponding to the different values of *d*, when assuming the same *n*, *r*, and polarization, are not identical, due to the fact that although the same range of angles of incidence is evaluated, the wave front is considered to be spherical and therefore, the attenuation obtained in every case is different because the distance covered by the wave is not the same. Thus, there exists more attenuation at a given negative angle of incidence for *d* = 0.20 m (a maximum difference of 1.37 dB for α = -5.2°, *n* = 5, *r* = 0.02 m, and *hard/vertical* polarization), but the opposite occurs for positive values of α, where the value *d* = 0.10 m shows more losses due to multiple diffraction (a maximum difference of 3.29 dB for α = 5.2°, *n* = 5, *r* = 0.02 m, and *hard/vertical* polarization).

d) Variation of the type of polarization.

The influence of the type of polarization is more relevant at negative angles of incidence, where the *soft/horizontal* polarization results show a greater attenuation with respect to the *hard/vertical* polarization case (up to 7 dB of difference).

3.2.5 Conclusions

A *UTD-PO* solution for the analysis of multiple-cylinder diffraction has been validated through measurements performed at *60 GHz*. A parametric study has been carried out both theoretically and experimentally in which the influence of: the number of cylinders, the radius of curvature, the distance from the transmitter to the array of rounded surfaces, and the polarization has been analyzed. The solid agreement found between the predicted and measured results (with a *Mean Error* ranging from 0.12 to 0.71 dB) shows that the *UTD-PO* theoretical formulation can be applied for radiowave propagation studies when multiple-diffraction over cylindrical surfaces has to be taken into account.

3.3 Comparison Between Rectangular and Cylindrical Modeling

A comparison of the presence of cylindrical against rectangular obstacles in radio wave multiple-diffraction analysis in the *mm-W* frequency-band is presented in this section.

Both theoretical results—through hybrid formulations *UTD-PO*—and experimental results—through measurements performed at 60 GHz are used to the analysis of multiple diffraction in the *mm-W* band when propagation over periodic obstacle patterns—either rounded or flat—has to be considered.

3.3.1 Introduction

The theoretical analysis of the multiple diffraction which takes place when radio waves impinge over an array of obstacles should involve, among other considerations, a realistic modeling of such obstructing elements in order to obtain precise path loss predictions. In this sense, if an urban propagation environment is to be studied, buildings

should be modeled as rectangular sections (plateaux) as the most rigorous choice, as shown in [Janaswamy, 2000]. However, if the elements obstructing the line of sight between the transmitter and the receiver have a rounded shape, as occurs in the case of hills present in a rural environment, cylindrical modeling of the obstacles would be the better option [Koutitas, 2006].

A different number of scenarios are suitable for studying the phenomenon of multiple diffraction at *mm-W* frequencies. For example, an aircraft cabin is expected to occur the phenomenon of multiple diffraction due to the presence of the seat rows. In this way, to analyze such multiple diffraction, if the seats are considered to be empty, rectangular modeling would be the most appropriate to obtain realistic predictions but, if they are taken, cylindrical shapes would better model the heads of the passengers.

Thus, in this Section the difference between the previously mentioned two types of modeling in the multiple-diffraction analysis of wireless communication systems is evaluated in the *mm-W* frequency-band.

A comparison of cylindrical against rectangular obstacles is performed both theoretically—through hybrid formulations *UTD-PO* and experimentally—through measurements performed at 60 GHz within a controlled environment where cylindrical and square-section bars are considered. The results can be applied to the analysis of multiple diffraction in the *mm-W* band when propagation over periodic obstacle patterns has to be considered.

3.3.2 Theoretical Model

Figure 3.15 shows the schemes of the propagation environments considered for the multiple-cylinder model and for the multiple-plateau model.
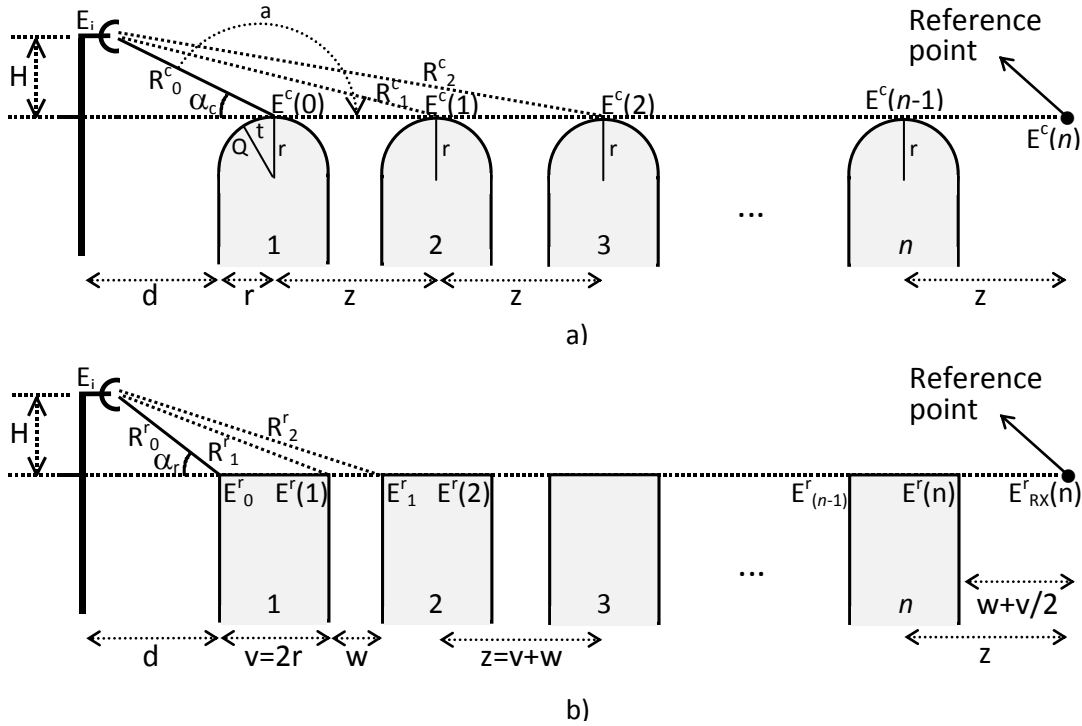
Figure 3.15: Scheme of the propagation environments considered: a) array of cylinders, b) array of plateaux (rectangular sections).

In Figure 3.15 a), the model is composed of a series of n perfectly-conducting cylinders of the same height—which is relative to the transmitter antenna height H—, constant inter-cylinder spacing z, and the same radius of curvature r, have been taken into account. Moreover, the source is at an arbitrary height, above or level with the average cylinder height ($H \geq 0$), and is located at a certain distance d from the array of cylinders (spherical-wave incidence).

In this sense, the field reaching the reference point indicated in Figure 3.15a) can be obtained by the final solution presented in C.18 in *Appendix C*.

In Figure 3.15b), an idealized representation of the propagation environment considered for the multiple-plateau model can be observed, where n perfectly-conducting rectangular plateaux of the same height, which is relative to the transmitter antenna height H, have been taken into account, assuming that they have the same thickness v and constant inter-plateau spacing w ($v+w = z$). The transmitting point is assumed to be located above or level with the average rooftop height ($H \geq 0$) and at a certain distance d from the array of rectangular sections (spherical-wave incidence).

In this case, the total field arriving at the reference point indicated in Figure 3.15b) can be calculated by applying the final formulation given in C.8 in *Appendix C*.

3.3.3 Measurement Setup

In Figure 3.16, the scheme of the measurement setup considered for both scenarios (cylinders and square-section bars) can be observed. Such measurement setup is the same as that employed in 3.2.3.
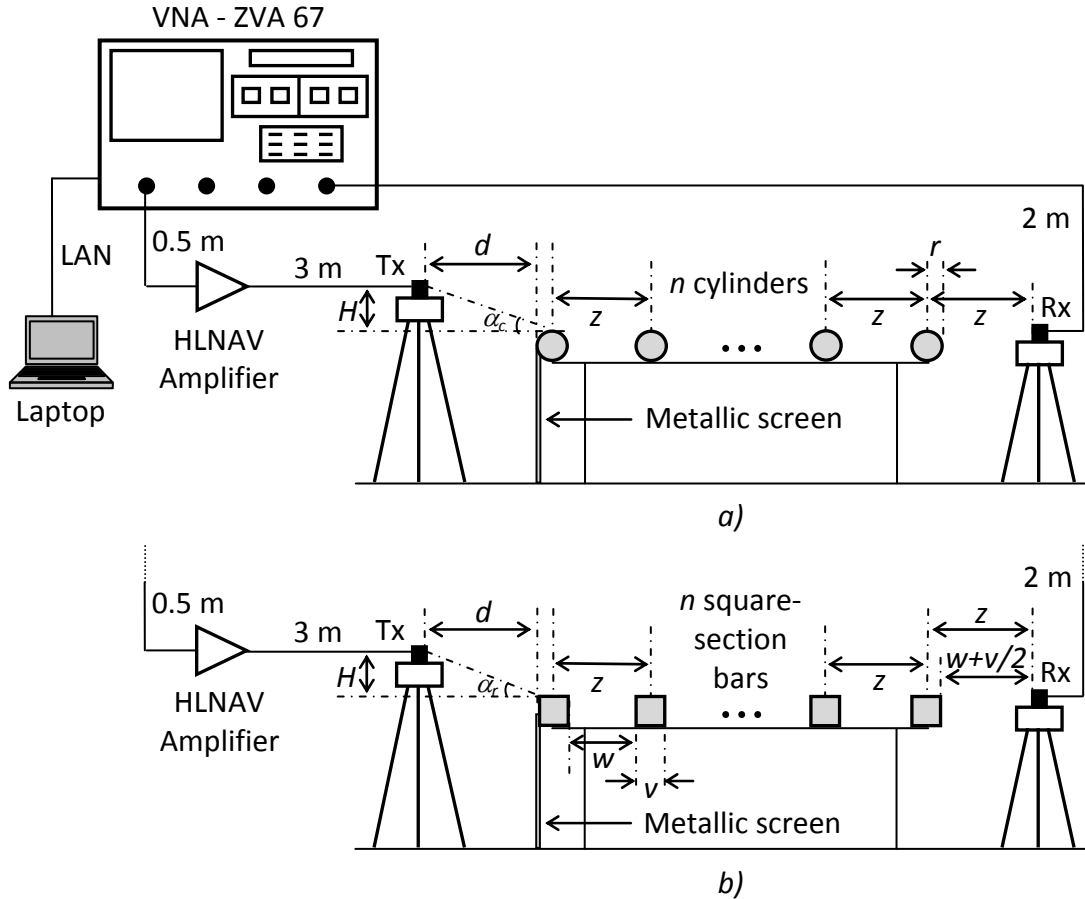
Figure 3.16: Scheme of the measurement setup for an array of a) *n* cylinders
b) *n* square-section bars.

Measurements were performed for three different values of *n* (number of perfectly-conducting cylindrical bars or perfectly-conducting square-section bars), two values of $r = v/2$ (radius of curvature of the cylinders or half the width of the square sections), *soft/horizontal* polarization, and two different values of *d* (distance from the transmitter to the series of obstacles): $d = 0.10$ m and $d = 0.20$ m. When $d = 0.20$ m was considered, the transmitting antenna height was varied from 0 m to 0.02 m and, for $d = 0.10$ m, from 0 m to 0.01 m, both cases in steps of 0.025 m. In such a way, the incident angles α_c and α_r (see Figure 3.14) have a maximum value of around 5.2° and 5.7°, respectively, for the evaluated results, which should be large enough for multiple-diffraction considerations.

Moreover, a metallic screen was placed at the location of the first obstacle in both scenarios in order to eliminate any contribution coming from below the array of diffracting elements, as can be observed in Figure 3.16. In Figure 3.17, the real scenarios are showed.

a)   b)   c)
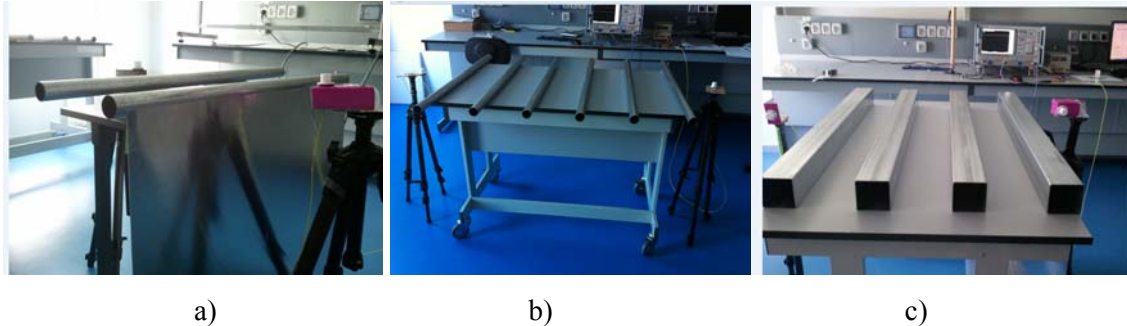
Figure 3.17: Photos a) Scenario for n=2 cylinder obstacles, b) Scenario for n=6 cylinder obstacles and c) Scenario for n=4 rectangular obstacles.

The *channel frequency response* was measured over 301 frequency points, equally spaced between 58 and 62 GHz, leading to a frequency step of 13.3 MHz, with 1 Hz being the *intermediate frequency*. These values were chosen in order to have a resolution time of 0.25 ns (0.075 m) and to be able to perform the *time-gating* technique which is explained in 3.1.3.

Furthermore, 301 frequency points were selected, so that a maximum delay of 75 ns (22.5 m) could be measured, not having time aliasing in the domain (the maximum dimension of the measurement environment is 7 m).

3.3.4 Results

The results for the attenuation as a function of H at the reference point of Figure 3.15—relative to the free-space field strength—can be observed in Figures 3.18 to 3.21, where both the theoretical predictions calculated with the previously explained formulations and the measurements performed at 60 GHz are depicted.

Three different values of n—number of perfectly-conducting cylinders/square-section bars—($n = 2$, $n = 4$, and $n = 6$) have been considered in the four figures as well as two different values of $r = v/2$: $r = 0.02$ m and $r = 0.04$ m. Furthermore, constant inter-obstacle spacing of $z = 0.232$ m and *soft/horizontal* polarization have been assumed in every case.
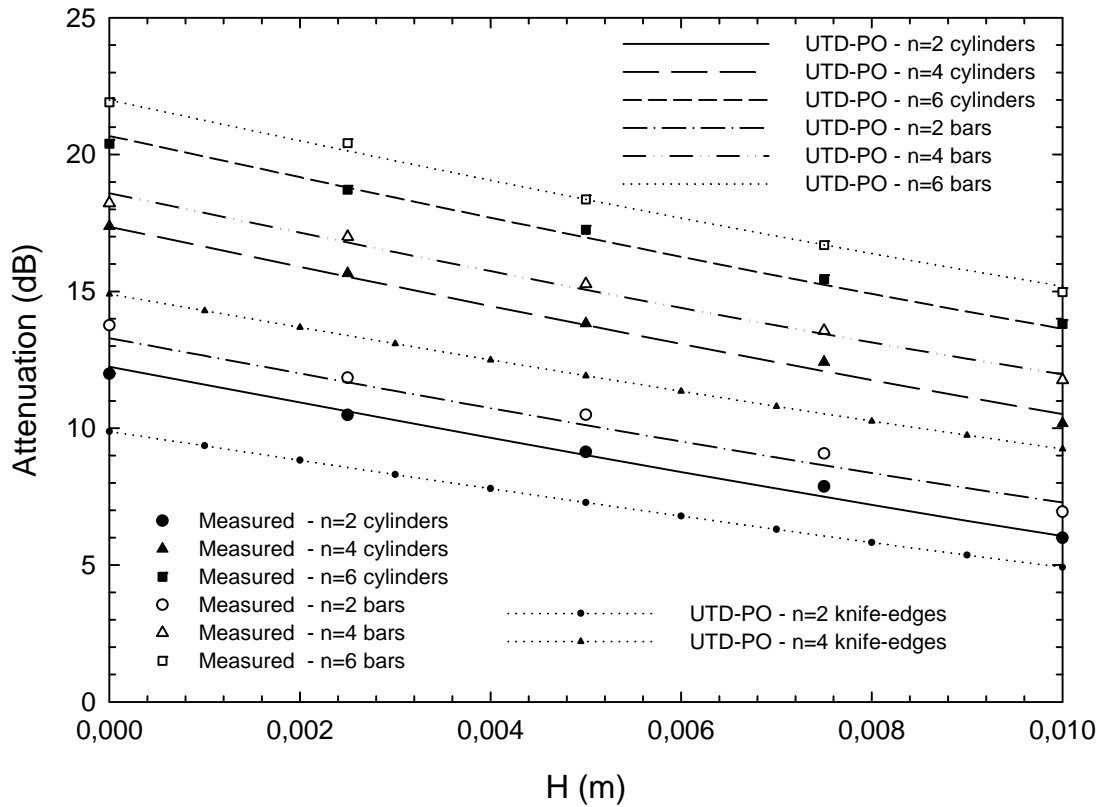
Figure 3.18: Comparison of the theoretical formulation results against the measurements at
60 GHz. *z* = 0.232 m, *d* = 0.10 m, and *r* = 0.02 m.
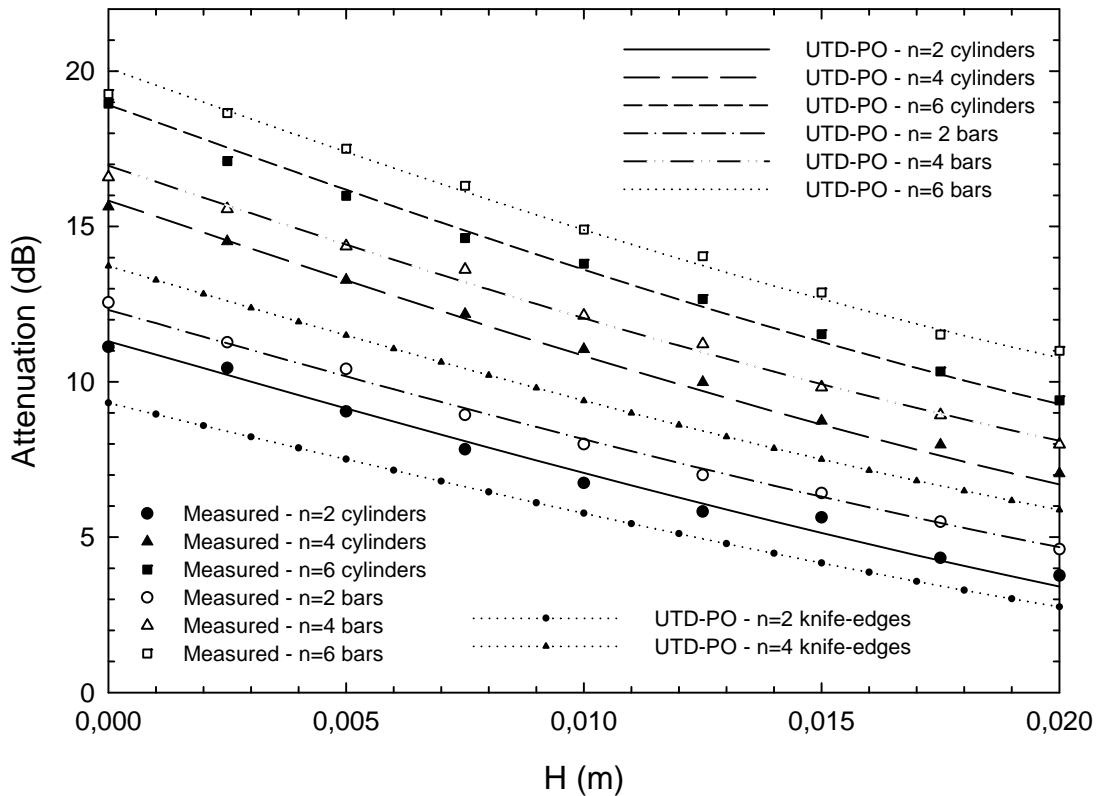
Figure 3.19: Comparison of the theoretical formulation results against the measurements at
60 GHz. *z* = 0.232 m, *d* = 0.20 m, and *r* = 0.02 m.
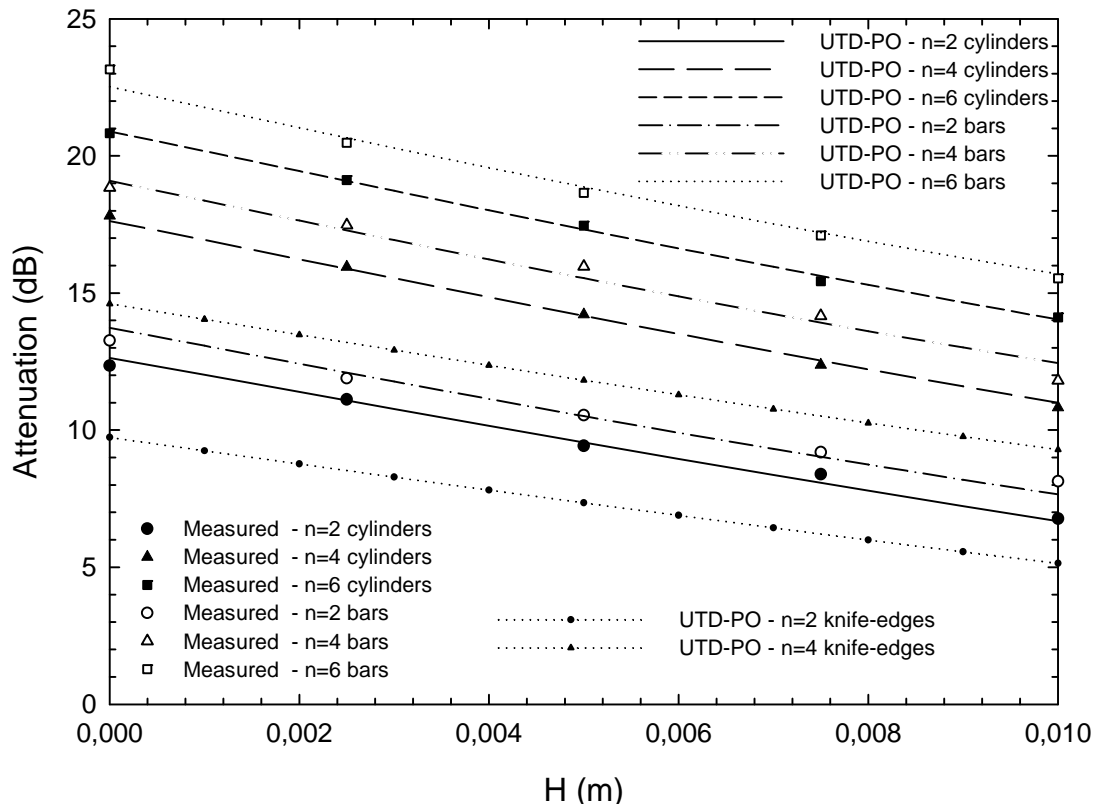
Figure 3.20: Comparison of the theoretical formulation results against the measurements at 60 GHz. $z = 0.232$ m, $d = 0.10$ m, and $r = 0.04$ m.
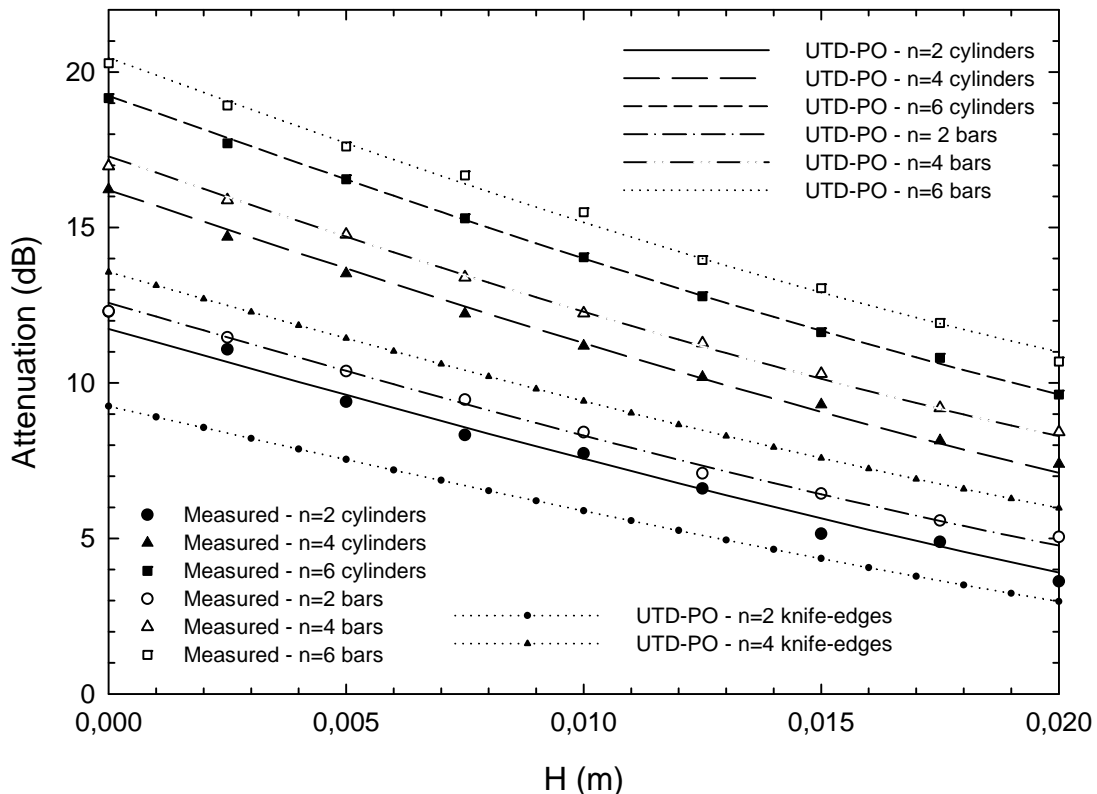
Figure 3.21: Comparison of the theoretical formulation results against the measurements at 60 GHz. $z = 0.232$ m, $d = 0.20$ m, and $r = 0.04$ m.

In Figure 3.18 and Figure 3.19, the results for $r = 0.02$ m, considering $d = 0.10$ m and $d = 0.20$ m, respectively, are shown. On the other hand, in Figure 3.20 and Figure 3.21, the attenuation results, assuming in this case $r = 0.04$ m, are depicted for $d = 0.10$ m and $d = 0.20$ m, respectively. For comparison purposes, the curves corresponding to the cases where the obstacles are substituted by knife-edges are also shown in the plots for $n=2$ and $n=4$ (such curves have been obtained through the formulation presented in [Rodríguez, 2007]).

As can be observed, a solid agreement is obtained in the four figures between the theoretical predictions achieved by the theoretical formulations and the measurements. In this sense, in order to quantify such agreement, Table 3.4 and Table 3.5 show the *mean* and the *variance* of the error in dB between the theoretical solutions and the empirical values, for $r = 0.02$ m and $r = 0.04$ m, respectively.

	Cylinder Model		Plateau Model	
	Mean Error	Variance	Mean Error	Variance
n=2 (*d*=0.10 m)	0.19	0.012	0.35	0.011
n=2 (*d*=0.20 m)	0.25	0.014	0.11	0.007
n=4 (*d*=0.10 m)	0.17	0.017	0.22	0.005
n=4 (*d*=0.20 m)	0.19	0.014	0.16	0.017
n=6 (*d*=0.10 m)	0.20	0.005	0.11	0.012
n=6 (*d*=0.20 m)	0.20	0.011	0.23	0.051

Table 3.4: *Mean* and *variance* of the error between the theoretical results and the measurements (dB). R=0.02 m.

	Cylinder Model		Plateau Model	
	Mean Error	Variance	Mean Error	Variance
n=2 (*d*=0.10 m)	0.16	0.011	0.08	0.095
n=2 (*d*=0.20 m)	0.28	0.027	0.12	0.012
n=4 (*d*=0.10 m)	0.12	0.003	0.35	0.025
n=4 (*d*=0.20 m)	0.15	0.008	0.11	0.006
n=6 (*d*=0.10 m)	0.10	0.003	0.25	0.037
n=6 (*d*=0.20 m)	0.06	0.004	0.16	0.010

Table 3.5: *Mean* and *variance* of the error between the theoretical results and the measurements (dB). R=0.04 m

It can be noted how such statistical parameters exhibit a relatively small error between the theoretical solutions and the measurements for all the cases considered.

Regarding the comparison between the cylindrical and rectangular obstacle modeling, it should be noted that, for a given n, the rectangular (square in the measurement scenario) modeling shows more attenuation than the cylindrical modeling for all the cases evaluated and, moreover, the interesting fact is that, for a given n, the difference between the curves of the two types of obstacle representation appears to be constant with H (according to the simulation results). The mean value of such offset (along the entire range of H considered in each case) for the different values of n, r, and d can be observed in Table 3.6.

	r=0.02 m		r=0.04 m	
	d=0.10 m	d=0.20 m	d=0.10 m	d=0.20 m
n=2	1.11	1.10	0.99	0.78
n=4	1.31	1.23	1.40	1.06
n=6	1.41	1.30	1.59	1.21

Table 3.6: *Mean* of the offset between the rectangular and cylindrical modeling results.

In view of Table 3.6, it can be observed that, for given values of r and n, the mean value of the offset is always greater for the smaller value of d ($d = 0.10$ m), with a maximum difference of 0.38 dB (compared to the case when $d = 0.20$ m) for $n = 6$ and $r = 0.04$ m. Moreover, for a fixed value of r and d, the offset grows with the number of obstacles n (with a maximum value of 1.59 dB for $n = 6$, $r = 0.04$ m and $d = 0.10$ m).

In order to further analyze the latter fact, Figure 3.22 is shown, where the offset in dB between the multiple-plateau and the multiple-cylinder theoretical models is evaluated as a function of n for the two values of r considered: $r = 0.02$ m and $r = 0.04$ m, considering $H = 0.005$ m with $d = 0.10$ m, and $H = 0.01$ m with $d = 0.20$ m ($\alpha = 2.86°$ in both cases).
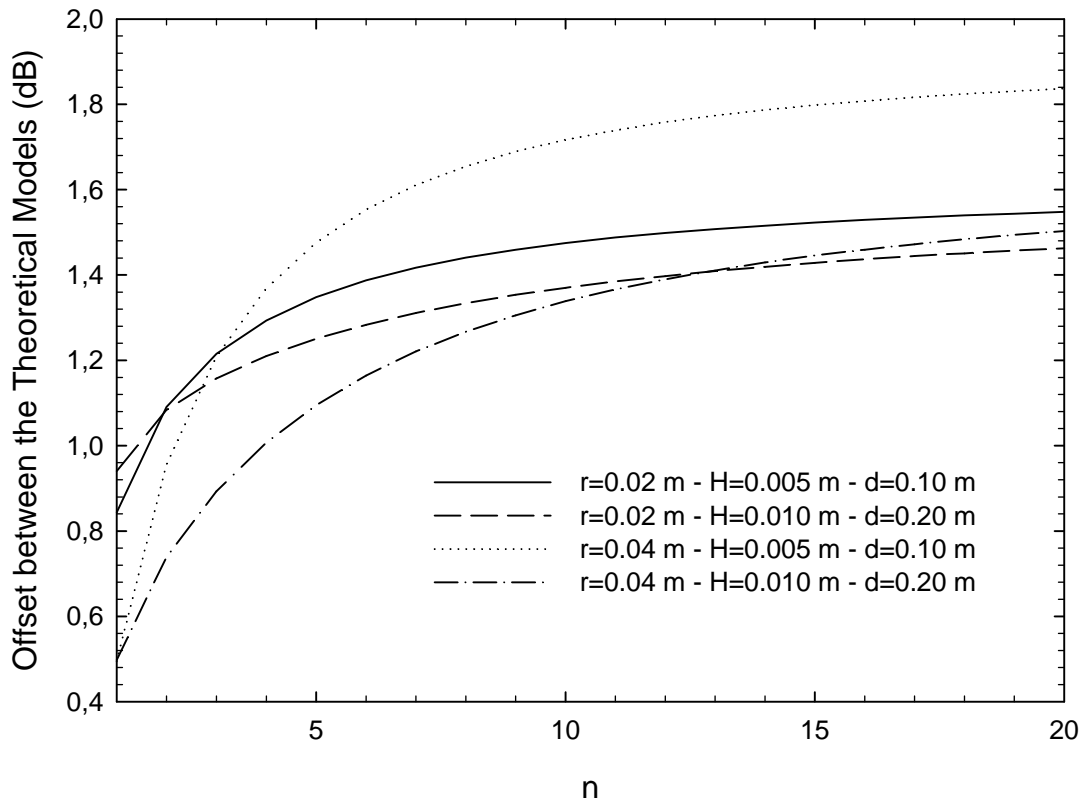
Figure 3.22: Offset between the multiple-cylinder and the multiple-plateau theoretical models as a function of the number of obstacles *n*. *z* = 0.232 m.

Both z = 0.232 m and *soft/horizontal* polarization have been again assumed in every case. As can be observed in the figure, for a fixed value of *r*, the offset for both values of *d* follows the same tendency after passing a few obstacles (around $n = 5$). On the other hand, for a given value of *d* (and the corresponding value of *H*), first, the smaller radius $r = 0.02$ m leads to greater offsets when compared to $r = 0.04$ m but, after some obstacles ($n = 2$ for $H = 0.005$ m and $d = 0.10$ m, and $n = 13$ for $H = 0.01$ m and $d = 0.20$ m), the opposite occurs, and the greater radius $r = 0.04$ m shows a greater offset (with a maximum value of 1.82 dB for $H = 0.005$ m, $d = 0.10$ m, and $n = 20$) .

3.3.5 Conclusions

A comparison of cylindrical against rectangular obstacles in radio wave multiple-diffraction evaluation has been performed, both theoretically—through *UTD-PO* formulations—and experimentally—through measurements performed at 60 GHz. Solid agreement has been found between the predicted and measured results. The rectangular modeling has shown higher attenuation than the cylindrical obstacle representation for all

the cases evaluated and a constant difference with *H*—of up to 1.82 dB—has arisen when comparing the two types of models (for a given number of diffracting elements *n*). Such a fact shows that the choice of appropriate obstacle modeling can be significant to obtain realistic multiple-diffraction loss predictions in the *mm-W* band.

3.4 Radiowave Negative Incidence Over a Rectangular Obstacle

In this last Section, the propagation loss due to the diffraction that takes place at the top of a rectangular obstacle that is illuminated from a low source is studied, i.e., the transmitter height is smaller than the obstacle height.

For this aim, a method based on a *UTD-PO* formulation for the analysis of the propagation loss is presented.

The method, which is mathematically less complex than existing techniques, applies *Babinet's principle*, and is validated through the solid agreement obtained with measurements at 60 GHz and the comparison with a method which is based on the evaluation of a Fresnel surface integral.

3.4.1 Introduction

The evaluation of radiowave propagation over a rectangular block that is illuminated from below can be beneficial to signal-level prediction (e.g. analysis and planning of radioelectric coverage in urban environments). Such evaluation necessarily implies the consideration of the diffraction phenomenon that occurs due to the presence of the block. In this sense, several studies have proposed different methods to obtain the attenuation caused by a flat-topped obstacle [Whitteker,1990] [Gong,1989] [Haslett,1991], all of which are based on the calculation of Fresnel integrals.
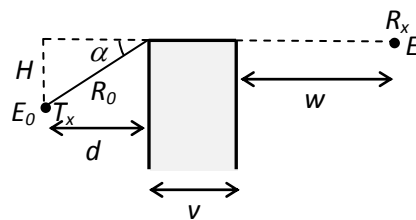
Figure 3.23: Geometry considered.

As can be observed in Figure 3.23, the receiver will be considered to be located at the "shadow boundary" of the second wedge of the plateau (i.e., along the extension of the block straight top). Such assumption is due to the fact that the *UTD-PO* formulation is based on the solutions presented in *Appendix C* for radiowave multiple-diffraction analysis which were developed in order to analyze the multiple-building diffraction loss factor described by Bertoni. Such factor is present in urban environments (it is well-known that he and Walfish expressed urban propagation path loss as the summation of three factors, namely, free space losses, multiple-building diffraction losses, and final diffraction losses from the top of the last building down to street level).

In this sense, losses due to building diffraction are usually evaluated at a receiving point located at the same height of the preceding buildings, i.e., where a final diffracting element would be placed. At such position, the final diffraction losses down to street level would be evaluated with the proper formula.

Therefore, considering the *UTD-PO* formulation expressed later, if the receiver is located at different heights, the recursivity that lies within the solution could not take place. The above-mentioned fact is a limitation of the proposed formulation but, on the other hand, the case considered in this thesis is significant enough to be analyzed in radiowave propagation over a rectangular obstacle, above all, if we consider that the receiving point could be located over an eventual final diffracting obstacle (where the formulation for final diffraction losses would be applied).

3.4.2 Theoretical Model

The scenario is depicted in Figure 3.24, consisting of a perfectly conducting rectangular obstacle illuminated from below with an angle of incidence α.
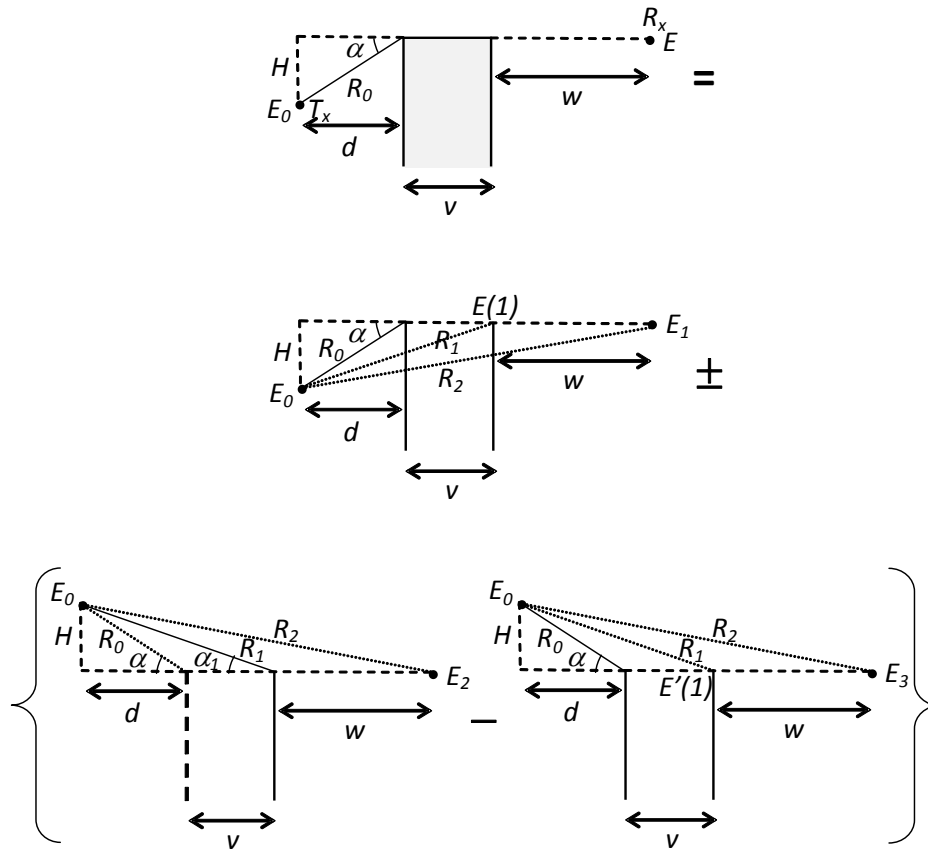
Figure 3.24: Schematic of the considered environment.

As stated in [Whitteker,1990], the resultant field strength E at the receiving point R_x can be obtained as the summation of two components: one which considers propagation over a double knife-edge instead of the rectangular block (E_1), and another which represents the additional reflection that takes place on the top of the plateau.

The second component can be calculated, as indicated in [Haslett, 1991], as the contribution from a virtual source undergoing inverted double knife-edge diffraction. In order to simplify the evaluation of such geometry, *Babinet's principle* can be applied so that the reflected component would be, as shown in Figure 1, the difference between a single diffraction over the second knife-edge in the absence of the first (E_2), with illumination from above, at the angle of incidence α_1, and a double knife-edge diffraction (E_3), also considering illumination from above, at the angle of incidence α.

Therefore, by considering the *UTD-PO* solution for multiple knife-edge diffraction as presented in [Rodríguez, 2007], the total field E that reaches the receiving point R_x in Figure 2.23 can be calculated as

$$E = E_1 \pm (E_2 - E_3) \qquad (3.17)$$

where '+' is applied when vertical polarization is considered and '−' for horizontal polarization. The first term in (1) can be calculated as follows:

$$E_1 = \frac{1}{2}\left[\frac{E_0}{R_0}\exp(-jkR_0)\sqrt{\frac{R_0}{(v+w)(R_0+v+w)}}\right.$$

$$\cdot D\left(\varphi = \frac{3\pi}{2}, \varphi' = \frac{\pi}{2}+\alpha, L = \frac{R_0(v+w)}{R_0+(v+w)}\right)\exp(-jk(v+w)) + E(1)\sqrt{\frac{R_0}{w(R_0+w)}} \qquad (3.18)$$

$$\left.\cdot D\left(\varphi = \frac{3\pi}{2}, \varphi' = \frac{\pi}{2}+\alpha, L = \frac{R_0 w}{R_0+w}\right)\exp(-jkw)\right]$$

where E_0 is the relative amplitude of the spherical wave (the transmitter Tx is assumed to be located at a certain distance d in Figure 1), k is the wave number,

$$E(1) = \frac{E_0}{R_0}\exp(-jkR_0)\sqrt{\frac{R_0}{v(R_0+v)}} \cdot D\left(\varphi = \frac{3\pi}{2}, \varphi' = \frac{\pi}{2}+\alpha, L = \frac{R_0 v}{R_0+v}\right)\exp(-jkv) \quad (3.19)$$

and $D(\phi,\phi', L)$ is the diffraction coefficient for a knife-edge, as given in [Kouyoumjian, 1974]. It should be noted that the *UTD-PO* solution used in this paper for multiple knife-edge diffraction analysis −assuming spherical-wave incidence−, as stated in [Rodríguez, 2007], is not a pure *UTD* approach, but a hybrid *UTD-PO* formulation obtained following the same methodology as that which is used in [Juan-Llácer, 2002] for the multiple-wedge diffraction of plane waves, which, at the same time, is based on the recursive *PO* formulation presented in [Saunders,1991]. In this way, it is assumed that the fields reaching the reference points of Figure 3.23 which correspond to E_1 and E_3 (where multiple-diffraction occurs) may be seen as the average of two field contributions coming from two spherical wave fronts impinging over every knife-edge so that the formulation can be expressed in terms of single diffractions in a recursive manner [Rodríguez, 2007].

One of these contributions corresponds to the field diffracted by the first knife-edge evaluated at a distance of *v+w* from such edge and the other takes account of the field diffracted once by the first knife-edge which is diffracted again by the second edge and evaluated at a distance *w* from the latter. As stated in [Rodríguez, 2007], the fact that E_1 and E_3 may be seen as the mentioned average of contributions implies considering identical wave fronts impinging with the same angle of incidence over every knife-edge (as occurs in the plane-wave incidence case [Juan-Llácer, 2002]).

In order to ensure the latter consideration in these spherical-wave incidence cases, in order to calculate the second contribution, a virtual spherical source is located (in the absence of the first knife-edge) at a distance *Ro* from the second knife-edge (the same distance which separates the source from the first knife-edge), bearing a relative amplitude *E(1)·Ro* (when considering the evaluation of E_1) and *E'(1)·Ro* (when considering the evaluation of E_3), which ensures the fields *E(1)* and *E'(1)*, respectively, over the second knife-edge—which were previously calculated—due to the spherical decay with distance, *1/R_0.*

Furthermore, the virtual spherical source is located with an angle of incidence α relative to the height of the knife-edges [Rodríguez, 2007]. This ensures the calculation of an arithmetic mean of a number of contributions coming from identical spherical wave fronts and impinging over every knife-edge with the same angle of incidence α. The obtaining of the recursive *UTD-PO* solution is possible due to the fact that the *UTD* diffraction coefficients are proportional to a Fresnel integral, as the solution presented in [Saunders,1991] is. Therefore, in the *UTD-PO* solution used in this paper for multiple knife-edge diffraction, only single diffractions are involved in the calculations (high-order diffraction terms are not considered in the diffraction coefficients) and that is one of the main advantages of the formulation, since such lack of terms barely entails in this case any loss in accuracy while at the same time providing a good computational efficiency.

The remaining terms in (3.17) are calculated as follows:

$$E_2 = \frac{E_0}{R_2}\exp(-jkR_2) + \frac{E_0}{R_1}\exp(-jkR_1)\sqrt{\frac{R_1}{w(R_1+w)}}$$
$$\cdot D\left(\varphi = \frac{3\pi}{2}, \varphi' = \frac{\pi}{2}+\alpha_1, L = \frac{R_1 w}{R_1+w}\right)\exp(-jkw)$$

(3.20)

and

$$E_3 = \frac{1}{2}\left[\frac{E_0}{R_0}\exp(-jkR_0)\left(\frac{R_0}{R_2}\exp(-jk(R_2-R_0))+\sqrt{\frac{R_0}{(v+w)(R_0+v+w)}}\right.\right.$$

$$\left. \cdot D\left(\varphi=\frac{3\pi}{2},\varphi'=\frac{\pi}{2}+\alpha, L=\frac{R_0(v+w)}{R_0+(v+w)}\right)\exp(-jk(v+w))\right)$$

$$+E'(1)\left[\frac{R_0}{R_1'}\exp(-jk(R_2-R_1))\right.$$

$$\left.\left.+\sqrt{\frac{R_0}{w(R_0+w)}}D\left(\varphi=\frac{3\pi}{2},\varphi'=\frac{\pi}{2}+\alpha, L=\frac{R_0 w}{R_0+w}\right)\exp(-jkw)\right]\right] \tag{3.21}$$

where

$$R_1' = \sqrt{(d+w)^2+H^2} \tag{3.22}$$

and

$$E'(1) = \frac{E_0}{R_0}\exp(-jkR_0)\left[\frac{R_0}{R_1}\exp(-jk(R_1-R_0))\right.$$

$$\left.+\sqrt{\frac{R_0}{v(R_0+v)}}D\left(\varphi=\frac{3\pi}{2},\varphi'=\frac{\pi}{2}+\alpha, L=\frac{R_0 v}{R_0+v}\right)\exp(-jkv)\right] \tag{3.23}$$

It should be noted that R_1' represents the distance between the previously mentioned virtual spherical source and the receiver, since in this case such direct ray has to be taken into account [Rodríguez, 2007].

3.4.3 Measurement Setup

As the previous Sections, the channel sounder employed is based on a Rohde & Schwarz ZVA67 *VNA*.
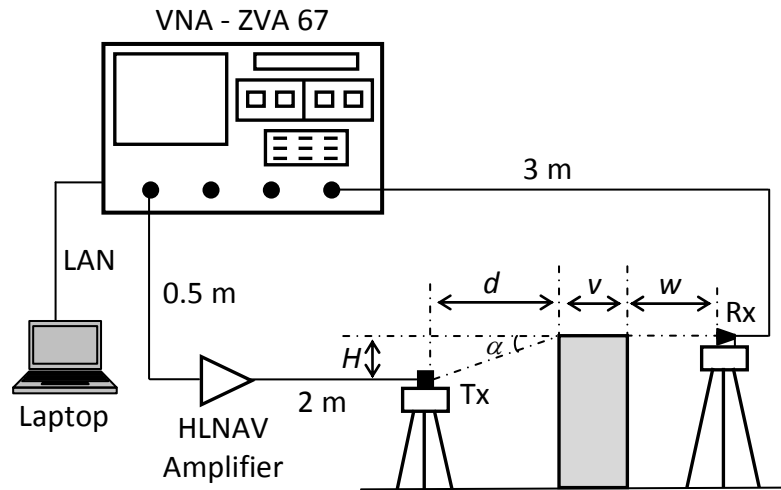
Figure 3.25: Scheme of the measurement setup.

As seen in Figure 3.25, the receiving antenna (*Rx*) is connected to one port of the *VNA* by using a 3 m coaxial cable, while the transmitter port signal of the VNA is amplified before being connected to the transmitting antenna (*Tx*) through a 2 m coaxial cable (the amplifier is, moreover, connected to the VNA through a 0.5 m coaxial cable). A horn antenna manufactured by *Q-PAR* (Ref. *H3445 25810-TA UG-385/U Comp*) was used as a receiver while an omnidirectional antenna *Q-par QOM55-65 VRA* as a transmitter.

The *channel frequency response* was measured at 501 frequencies equally spaced between 58 and 62 GHz, with a frequency step of 8 MHz, and 10 Hz as the *intermediate frequency*. As the previous theoretical models, this model is a *2D* approach. The results of the measurements were processed so that wave propagation is only considered along the vertical plane in which the transmitter and the receiver were aligned, considering the first contribution and cancelling the rest of them. To do so, a rectangular *time-gating* technique, described in 3.1.3, is applied for measurements taken both with and without the rectangular obstacle. Hence, the attenuation due to the block is obtained by the difference between the losses existing in the presence of the rectangular obstacle and the losses in free space (without the block).

Moreover, a maximum delay of 125.2 ns (37.57 m) could be measured due to 501 frequency points were selected, without having time-aliasing in the domain (the maximum dimension of the measurement environment is 7 m).

The channel can be considered to be stationary, because during the measurement process, nobody was inside the measuring environment. A detailed description of the channel sounder used in this work can be found in *Appendix B*.

3.4.4 Results

In order to validate the proposed solution, measurements were performed as a function of H (i.e., the rectangular obstacle height minus the transmitter height) at 60 GHz with a perfectly conducting rectangular block, $d = 0.20$ m, $v = w = 0.373$ m, for both horizontal and vertical polarizations.

Figure 3.26 depicts the results against the measured values for the attenuation at the receiver, relative to the free-space field strength, as obtained with both the proposed *UTD-PO* solution and the method given in [Haslett,1991] which is based on the evaluation of a Fresnel surface integral, as presented in [Millington,1962].

Furthermore, for the sake of comparison, the results for a double knife-edge for the same geometry parameters, as calculated using the *UTD-PO* formulation presented in [Rodríguez, 2007] and the mentioned method based on a Fresnel surface integral [Millington,1962], are also shown in the plot. As can be clearly seen, a solid agreement is found between the proposed solution and the measurements, especially for vertical polarization.
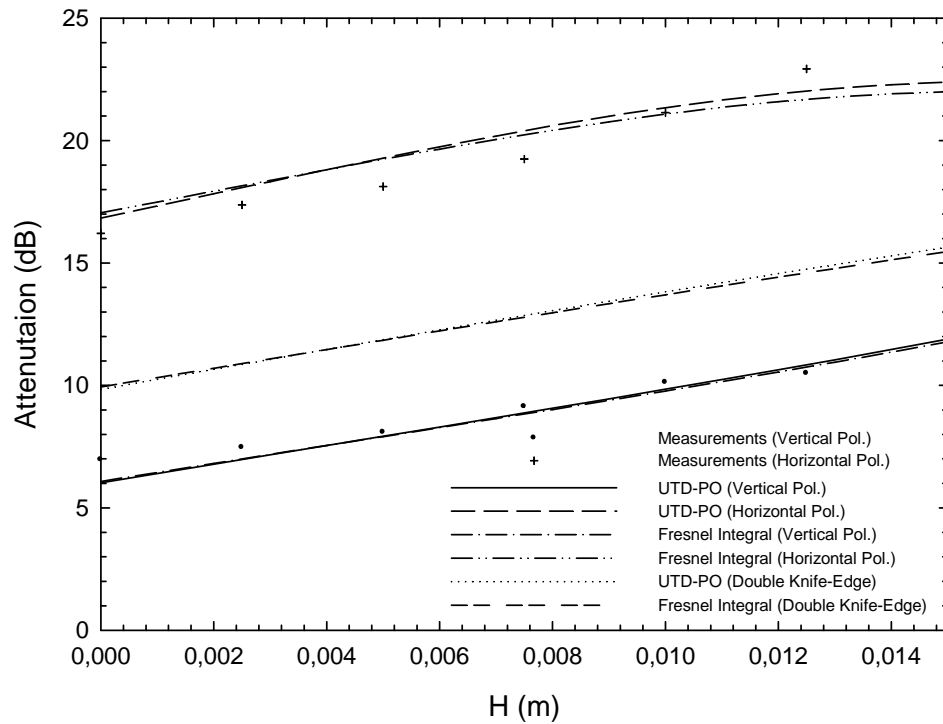
Figure 3.26: Comparison of measurements with the attenuation obtained using both the proposed UTD-PO solution for the evaluation of the propagation loss due to the diffraction that takes place at the top of a perfectly conducting rectangular obstacle and the method given in [Haslett, 1991] based on the evaluation of a Fresnel surface integral, as presented in [Millington, 1962]. Frequency = 60 GHz, $d = 0.20$ m, v = w = 0.373 m. The solutions for double knife-edge diffraction are also shown in the plot.

Moreover, an excellent agreement can be observed between the proposed *UTD-PO* solution and the Fresnel surface integral method. In order to quantify such agreement, Table 3.6 shows the mean and the variance of the error in dB between the two theoretical solutions and the empirical values, for both polarizations.

It should be noted how such statistical parameters exhibit a relatively small error between the proposed *UTD-PO* solution and the measurements, for all the cases considered. Besides, the *UTD-PO* formulation shows a smaller error than the method based on a Fresnel surface integral when horizontal polarization is considered.

	Mean Error		Variance	
	Vertical Pol.	Horizontal Pol.	Vertical Pol.	Horizontal Pol.
UTD-PO	0.50	0.85	0.11	0.09
Fresnel	0.48	1.01	0.07	0.16

Table 3.6: Mean and Variance of the error between the *UTD-PO* and the Fresnel integral results and the measurements (dB).

3.4.5 Conclusions

A new method based on a hybrid *UTD-PO* formulation for the evaluation of the propagation loss due to the diffraction that takes place at the top of a rectangular obstacle that is illuminated from a low source has been presented. The proposed solution shows less mathematical complexity than other existing techniques, and comparison with measurements and a method based on the evaluation of a Fresnel surface integral shows solid agreement.

3.5 Conclusions

In this chapter, several *UTD-PO* solutions for the analysis of radiowave multiple diffraction, which are less mathematical complexity than other existing techniques, have been validated through measurements performed at 60 GHz.

For the case of the series of rectangular blocks as obstacles, a solid agreement has been found between predicted data by the hybrid *UTD-PO* formulation and measured attenuation values at 62 GHz. Therefore, since the series of rectangular blocks can be assumed as scaled-models of an urban environment, the proposed *UTD-PO* formulation could be applied in the analysis of urban radiowave propagation.

Regarding the analysis of multiple-cylinder diffraction, it was performed a campaign of measurements at 60 GHz. A *UTD-PO* solution for this analysis has been validated with them. A parametric study has been carried out both theoretically and experimentally in which the influence of: the number of cylinders, the radius of curvature, the distance from the transmitter to the array of rounded surfaces, and the polarization has been analyzed. A *Mean Error* ranging from 0.12 to 0.71 dB has been found between the predicted and measured results. Thus, the *UTD-PO* theoretical formulation can be applied for radiowave propagation studies when multiple-diffraction over cylindrical surfaces has to be taken into account.

Next, a comparison of cylindrical against rectangular obstacles in radio wave multiple-diffraction evaluation has been studied. First, theoretically, it has been predicted the attenuation by *UTD-PO* formulations. Secondly, experimentally, measurements have

been performed at 60 GHz. A firm agreement has been found between the predicted and measured results. The rectangular modeling has shown higher attenuation than the cylindrical obstacle representation for all the cases evaluated and a constant difference with *H*—of up to 1.82 dB—has arisen when comparing the two types of models (for a given number of diffracting elements *n*). Such a fact shows that the choice of appropriate obstacle modeling can be significant to obtain realistic multiple-diffraction loss predictions in the *mm-W* band.

Lastly, a new method based on a hybrid *UTD-PO* formulation for the evaluation of the propagation loss due to the diffraction that takes place at the top of a rectangular obstacle that is illuminated from a low source has been presented. The comparison with measurements at 60 GHz and a method based on the evaluation of a *Fresnel* surface integral has shown a solid agreement.

Chapter 4

Multidimensional Millimeter Channel Modeling and Characterization

---

4.1 Introduction

The *millimeter-wave* (*mm-W*) frequency band is nowadays seen as the most feasible wireless frequency band for transmitting several gigabits via radio. The interest in this band relies on it being an unlicensed band for commercial applications, and its ability to provide extremely high data rates due to the large bandwidth available [Park, 2007].

Moreover, both the high attenuation present at 60 GHz, which greatly reduces interference, and the small frequency re-use distance offered, allows the development of short-range indoor systems with low-power transmitters.

In order to understand and predict its behavior, a detailed analysis of the propagation characteristics is vital. In this sense, this chapter is devoted to presenting a set of analyses of the millimeter wave frequency band.

Firstly, characterization of the diffuse scatter phenomenon is treated in section 4.2. Improving the *3D ray tracing* model implies to take into account all the propagation phenomena. To achieve this goal, a diffuse scattering model is introduced into the deterministic model. A scattering model depends on the diffuse parameters estimated from experimental measurements for common materials found in indoor environments

Then, in Section 4.3, deterministic and experimental indoor mm-W channel modelling is detailed. The high resolution algorithm *RiMAX* is applied to both experiment and simulation data to extract the geometrical parameters of the multipath components (*MPC*). Then, several clustering techniques are implemented and applied over the *MPCs*. Furthermore, a new cluster estimation algorithm is proposed.

Centimeter- and millimeter-wave ultra-wideband radio channel characteristics in the same environment are compared in section 4.4.

Lastly, in Section 4.5, an experimental evaluation of an indoor *MIMO-OFDM* system is presented, taking into account the specifications of the *IEEE 802.15.3c* standard.

4.2 Diffuse Scattering Model at mm-W

The *Diffuse Scattering* phenomenon (see *Appendix A*), has been studied for years by [Beckmann, 1963] because of its relevance in the field of wave propagation and in many other fields of application as well (remote sensing, optics, physics, etc.) [Minghini, 2014].

Diffuse scattering concerns the interaction phenomena with irregular surfaces whose roughness is generally less than the wavelength, as can occur on an imperfectly flat building surface. This diffusion phenomenon also appears when there is penetration of waves in heterogeneous media, such as vegetation. Therefore, rays impinging this surface scatter in directions other than the specular reflected ray. In this case, geometric optic approximation cannot be applied [Balanis, 1989].

In the literature, few publications refer to the integration of measurement-based scattering model into *Ray Tracing (RT)* tools applied to the *mm-W* frequency band. The authors in [Järveläinen, 2014], use a point cloud-based full diffuse propagation prediction method, and the overall field is described as fully diffuse, back-scattered from the point cloud measured by a laser.

The models for *diffuse scatter* described in [Degli-Esposti, 2001], [Degli-Esposti, 2007] are suitable to easily introduce scattering in geometric optics tools. Among the three models proposed in these papers, the *directive* and *Lambertian* models are the most important. Usually, the model parameters are adjusted from the whole set of measurements for a given environment, regardless of the heterogeneous nature of materials.

However, it seems more interesting to start from independent material characterization for each element of the environment. We have thus followed the approach of [Kyro, 2013] to estimate the diffuse parameters for elements found in our indoor environment.

4.2.1 The Diffuse Scattering Modelling

Scattering occurs when the medium through which the wave travels consists of objects with dimensions that are small compared to the wavelength, and where the number of obstacles per unit volume is large. Scattered waves are produced by rough surfaces, small objects or by irregularities in the channel [Rappaport, 1996].

The actual received signal in a mobile radio environment is often stronger than that which is predicted by reflection and diffraction models alone. This is because when a radio wave impinges on a rough surface, the reflected energy is spread out (diffused) in all directions due to scattering. The energy scattered in all directions provides additional energy at the receiver.

Diffuse scattering involves the signals scattered in directions other than the specular direction as a result of deviations (surface or volume irregularities) in a reached wall [Degli-Esposti, 2007].

In Figure 4.1 reflection and diffuse scattering phenomena are drawn. The field scattered by the generic wall element dS is modeled as a non-uniform spherical wave which departs from the element and propagates in the upper half space.
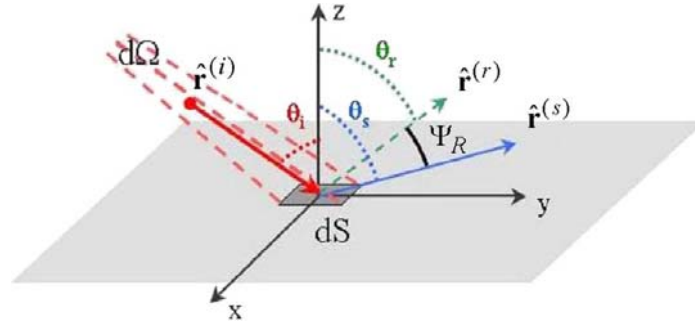
Figure 4.1: A generic surface element producing reflection and diffuse scattering [Degli-Esposti, 2007].

where $d\Omega$ is the solid angle of the ray tube impinging on the surface element dS, and $\hat{r}^{(i)}$, $\hat{r}^{(s)}$, $\hat{r}^{(r)}$ are the distances between dS, source and reception points, respectively. The scattering parameter is defined as:

$$S = \frac{|\overline{E}_S|}{|\overline{E}_i|}\Bigg|_{dS} \qquad (4.1)$$

where $|\overline{E}_S|$ and $|\overline{E}_i|$ are the norms of the scattered and incident fields on the surface element dS, respectively.

The following synthetic relation must be satisfied:

$$S^2 \cdot U^2 \cdot |\overline{E}_i|^2 \cdot d\Omega_i \cdot r_i^2 = \int_{2\pi} |\overline{E}_S|^2 d\Omega_S \cdot r_S^2 = \int_0^{\pi/2} \int_0^{2\pi} |\overline{E}_S|^2 \cdot r_S^2 \cdot \sin\theta_S d\theta_S d\phi_S \qquad (4.2)$$

U is a function depending on the definition adopted for the S parameter, and its value is:

$$U = \begin{cases} 1 \text{ if S=}|\overline{E}_S / \overline{E}_i| \\ \Gamma \text{ if S=}|\overline{E}_S / \overline{E}_R| \end{cases} \qquad (4.3)$$

Introducing the shape of the scattered wave $|\overline{E}_S(r_S,\theta_S,\phi_S)|$ (defined below), its maximum amplitude E_{S0} can be derived. The shape of the scattering patter of the wall is

affected by the characteristics of wall irregularities. There are two models which are used according to the scattering patterns and each one is representative of a practical situation:

- Model 1: *Lambertian Model* – This model assumes that the scattering radiation lobe has its maximum in the direction perpendicular to the wall.

$$\left|\overline{E}_S\right|^2 = E_{S0}^2 \cdot \cos\theta_S \tag{4.4}$$

Replacing E_{S0} for its value:

$$\left|\overline{E}_S\right|^2 = \left(\frac{K \cdot S}{r_i \cdot r_S}\right)^2 \cdot U^2 \cdot \frac{\cos\theta_i \cdot \cos\theta_S}{\pi} dS \tag{4.5}$$

where K is a constant depending on the amplitude of the impinging wave.

- Model 2: *Directive Model* – This model takes into account that the scattering lobe is steered towards the direction of the specular reflection.

$$\left|\overline{E}_S\right|^2 = E_{S0}^2 \cdot \left(\frac{1 + \cos\Psi_R}{2}\right)^{\alpha_R} \qquad \alpha_{R=1,2,..,N} \tag{4.6}$$

where Ψ_R is the angle between the direction of the reflected wave and the scattering direction (θ_S, ϕ_S). The exponent α_R is related to the width of the scattering lobe. The maximum amplitude E_{S0} can be computed by:

$$E_{S0}^2 = \left(\frac{SK}{r_i r_s}\right)^2 U^2 \frac{dS \cos\theta_i}{F_{\alpha_R}} \tag{4.7}$$

- Model 3: *Backscattering Lobe Model* – This model adds a term accounting for backscattering phenomena to the previous model. For characterization this, a scattering lobe in the incident direction is introduced. The expression of the double-lobe model is:

$$\left|\bar{E}_S\right|^2 = E_{S0}^2 \cdot \left[\Lambda \left(\frac{1+\cos\psi_R}{2} \right)^{\alpha_R} + (1-\Lambda)\left(\frac{1+\cos\psi_i}{2} \right)^{\alpha_i} \right] \qquad \alpha_i, \alpha_R = 1,2,..N; \Lambda \in [0,1]$$

(4.8)

Doing some calculation, we obtain:

$$\vec{E} = \left[\frac{1}{\sqrt{2}} \left|\vec{E}_S\right| e^{j\chi\theta_S} \right] \hat{\theta}_S + \left[\frac{1}{\sqrt{2}} \left|\vec{E}_S\right| e^{j\chi\phi_S} \right] \hat{\phi}_S$$

(4.9)

4.2.2 Objective and Simulation Set-up

The objective is thus to estimate the S and α_R parameters at 60 GHz for several materials. To achieve this goal, the interaction of an *mm-W* transmission will be measured, and the different propagation mechanisms will be studied.

A top view of the simulation set-up is shown in Figure 4.2 and a transverse view in Figure 4.3. A directive lens transmitting antenna in *mm-W* has been used to successively illuminate the material at different angles of incidence. The *Tx* antenna always illuminates the same area: the center of the measured material. Thus, the component scattered from the center of the material always travels at a constant distance.

a)   b)
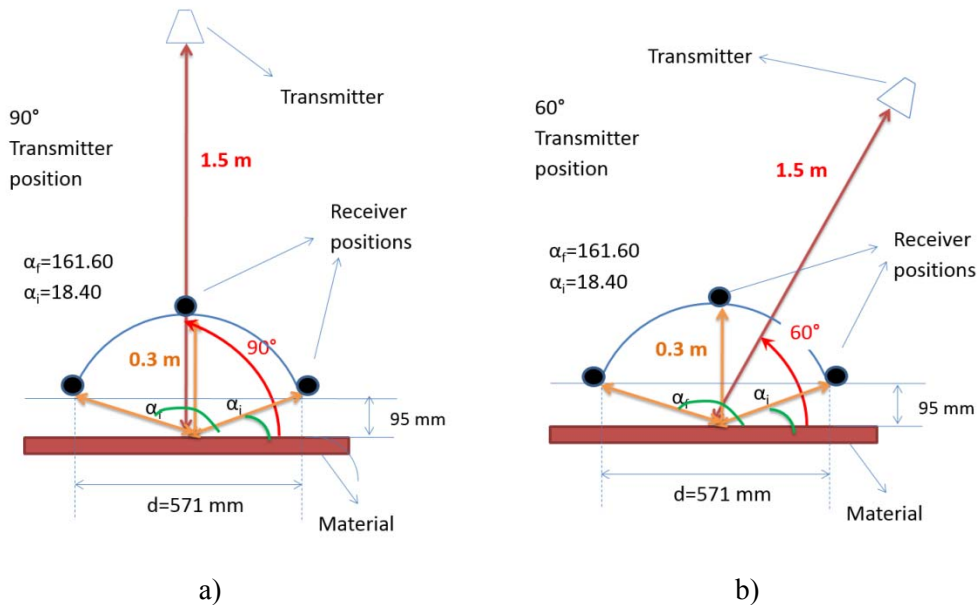
Figure 4.2: Top view of the simulation set-up: scheme for *Tx* antenna position a) 90 ° and b) 60°. The direction of polarization of the antennas is parallel to the air-material interface.
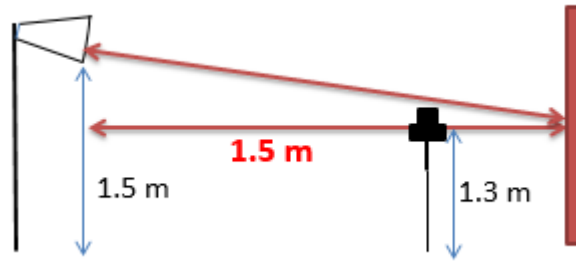
Figure 4.3: Transverse view of the set-up and heights of the transmitter and receiver above ground.

The electric field is measured by moving the receiving antenna on a half circle centered on the specular reflection point. The diffuse pattern is observed for a given angle of incidence.

Both antennas are linearly polarized, the direction of polarization being parallel to the interface, as detailed in the next paragraph. The measured E$_{\text{field}}$ component, E_i, is the sum of three components: the diffuse scattering field, the reflected field in the specular direction, and the direct field (line of sight (*LoS*) component), noted $E_i^{scattering}$ $E_i^{reflected}$ and E_i^{direct}, respectively. One can thus write:

$$E_i(m) = E_i^{scattering}(m) + E_i^{reflected}(m) + E_i^{direct}(m) \qquad (4.10)$$

where *m* and *i* are the frequency index and receiver position respectively. Note that $E_i^{scattering}$ in (4.10) is the sum of all diffuse components coming from the material. This is done by discretizing the material as will be seen later.

We have simulated this configuration in order to be able to easily interpret the experimental results. In this simulation, the radiation pattern of the *Tx* antennas has been introduced. For $E_i^{scattering}$, the material is discretized into a series of small surfaces, *dS* having a length of 10 λ in both directions and a random phase is added to the diffuse scattering components as suggested in [Järveläinen, 2013]. The depolarization was shown to be almost negligible at 60 GHz [Järveläinen, 2013], and thus has not been considered in the simulation.

The configuration of the experiments is the following:

- All receiver positions are at a constant distance of 0.3 m from the center of the material.

- The beam of the *Tx* antenna is oriented towards the center of the material.

- Three different angles (90°, 120° and 60°) have been selected for the *Tx* antenna orientations.

The *Tx* antenna is a lens antenna manufactured by *Q-PAR* (Ref. *H3445 25810-TA UG-385/U Comp*), with the following characteristics:

o   Frequency band: 51.5 GHz to 75 GHz

o   VSWR: 1.5 max

o   Lens Diameter: 100 mm

o   Nominal mid-band gain: 34 dBi

o   3 dB beamwidth E-plane: 3.5°

o   3 dB beamwidth H-plane: 4°

The *Rx* antenna is omnidirectional in a plane and presents a total gain of 4.5 dBi gain (*Q-par QOM55-65 VRA*).

4.2.3 Simulation Results

Based on geometrical consideration, the *ToA* of each contribution is computed and plotted in Figure 4.4 for an angle of incidence of 90° (this figure represents the delay of the contributions, without taking into account the amplitude). The *ToA* of the direct path (blue curve) presents a minimum value at $\alpha_i = 90°$ (see Figure 4.4) and then increases when *Rx* is moving on a circle towards the interface, i.e., when α_i tends to 0° or 180°. The same geometrical approach leads to an opposite variation of the reflected field (red curve), the *ToA* being maximum for $\alpha_i = 90°$. This is easily explained by the image theory. The *ToA* of the diffuse scattering component is constant whatever the *Rx* antenna position. It is represented in the figure as the vertical black line at 6 ns. This is true for the diffuse components created in the center of the material, since the delay is constant for a circle. From this line, we have plotted a vertical green line referring to the resolution delay of the measurements setup (1/9 GHz = 0.111 ns). This means that we will be able to time gate all energy between the black and green line taking into account that is not possible to resolve the diffusion and reflection at certain positions. It is thus necessary to simulate diffusion and reflection at those certain positions.

From these results, time gating appears as a technique to separate the diffuse component from the reflected path. This will be true where reflection does not overlap diffusion, where both contributions will be simulated.
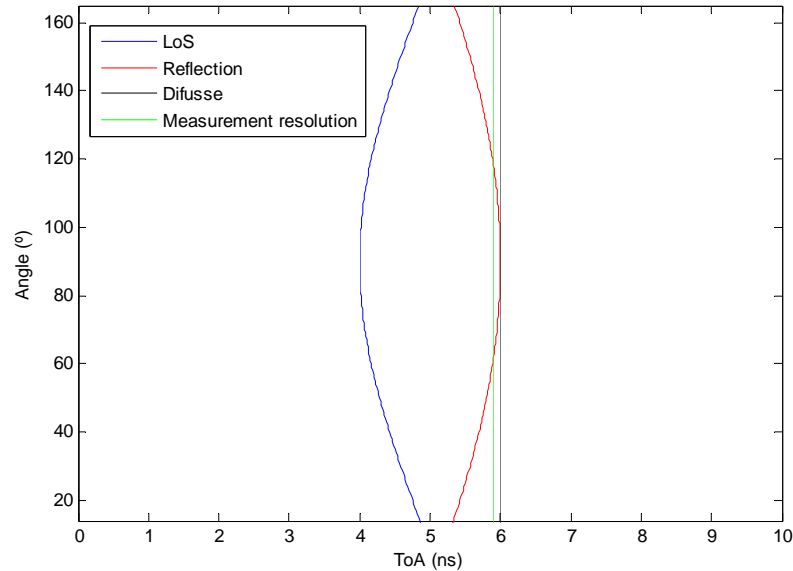
Figure 4.4: *ToA* of each contribution, deduced from the geometry of the configuration shown in Figure 4.2, depending on the angle α_i characterizing the angular position of the *Rx* antenna.

4.2.4 Experimental Set-up

A *Vector Network Analyzer* (ZVA 67 Rhode & Schwarz) is used to measure the frequency response (see *Appendix B*). Both antennas have vertical polarization. Figure 4.5 shows the scheme of the measurement setup. The movement of the receiver is controlled by a *2D step-motor* (C4 controller) as seen in the figure. This makes possible the movement the *Rx* antenna along a half circle. The *Tx* antenna is fixed on a tripod. Three different materials will be considered: glass, plasterboard and chipboard.
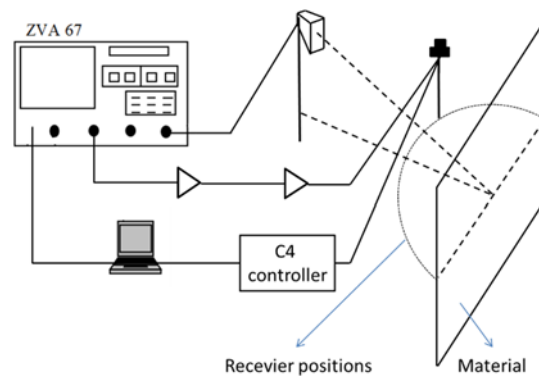
Figure 4.5: Measurement scheme.

In Figures 4.6a, 4.6b, and 4.6c we can see photographs of the measurement setup for glass, plasterboard, and chipboard.

a)   b)

c)

Figure 4.6: Measurement setup for a) glass b) plasterboard and c) chipboard.

The electrical parameters of the measurements are:

- o   Initial frequency: 57 GHz.
- o   Final frequency: 66 GHz.
- o   Number of frequency points: 2048.
- o   IF: 10 Hz.
- o   Transmitted Power = -10 dBm.

Firstly, all frequency responses are collected for all receiver positions within the semi-circle (H_i, i = 1,2,…303). Then, time domain responses for each position are obtained through the inverse Fourier transform. In Figure 4.7 we can see time channel responses evaluated when the material is glass and the position of the transmitter is α_i = 90°. The x-axis indicates the *ToA* while the y-axis is the angular position α_i of the *Rx* antenna. The colors show the received relative power in dB.
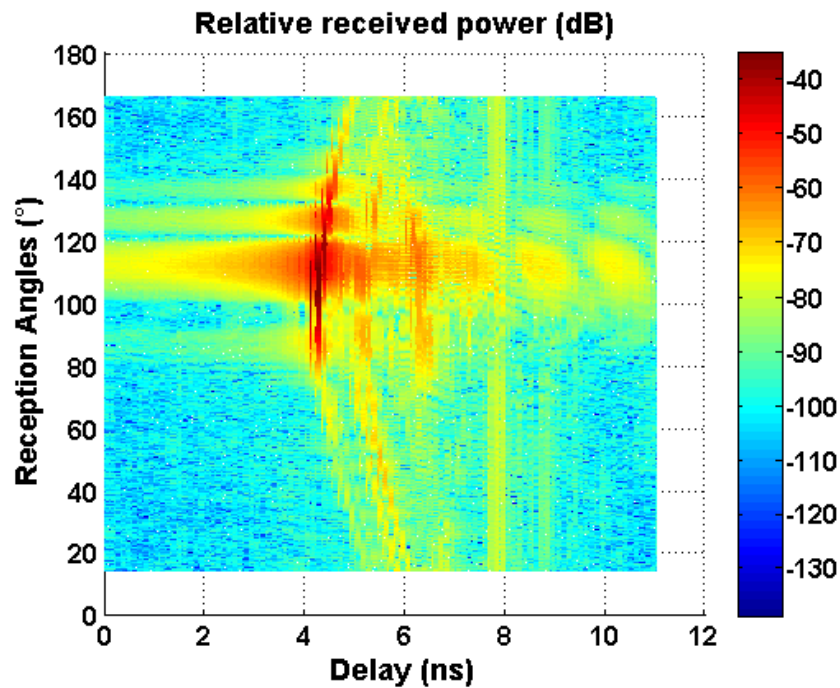
Figure 4.7: Time response of glass and 90°.

From Figure 4.7 and owing to the simulation results of Figure 4.4, we can easily identify from the shape of the curves the different contributions: direct ray, reflected ray, diffuse scattering and other components. However an offset angle is observed. Since this could be explained by an offset of the radiation pattern of the *Tx*, measurements of this pattern having been made in an anechoic room. Results presented in Figure 4.8 show, indeed, that the maximum of the main lobe occurs for an angle of -5°.

The consequence of this error in the manufacturing process is that the position where energy is diffused/reflected changes slightly from the center, as is illustrated in Figure 4.9.
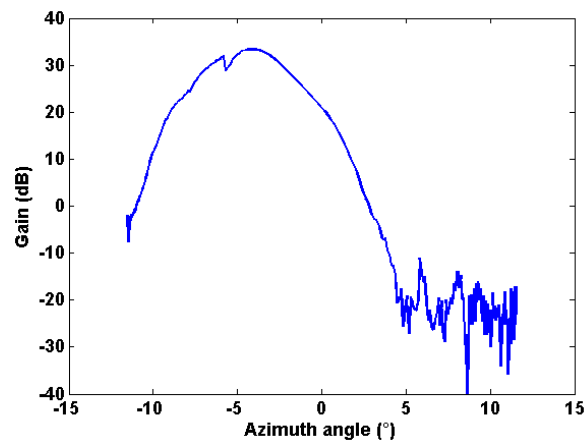
Figure 4.8: Radiation pattern of the directive (transmitter) antenna.
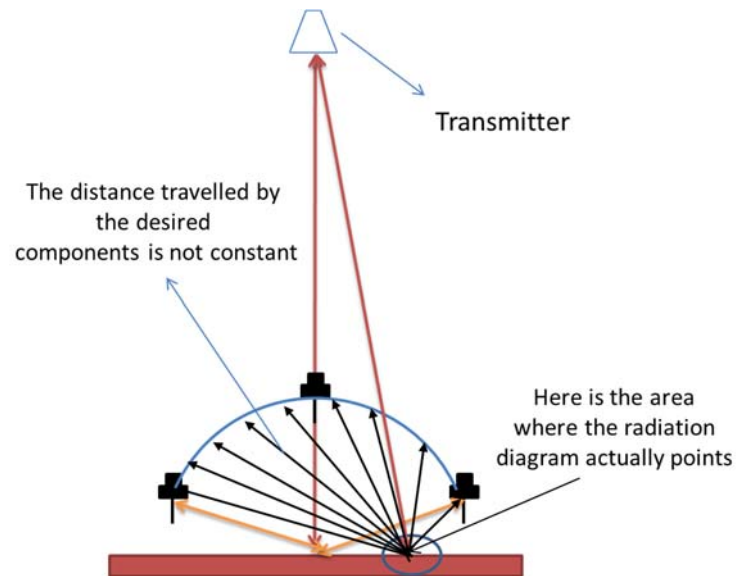
Figure 4.9: Consequence of an offset of the radiation pattern.

Fortunately, this effect can be easily corrected in the model by taking into account the real radiation pattern of the antenna. Furthermore, in the simulation, *LoS*, reflection and diffuse scatter are considered. Then, by applying a time gating technique each component can be separated in both cases, i.e. simulation and measurements.

In Figure 4.10, this technique allows the identification of *LoS* and reflected components, both in a range of the reception angle between 100 and 120°. The diffuse component is estimated between the two black lines, approximately at 110º for reception angle and 6.5 ns for *ToA*, and the overlaps' reflected path. One can note that these black lines are no more vertical, as for predicted curves shown in Figure. 4.4, due to the offset of the radiation pattern. The direct ray is located at the same reception angle but at 4 ns for *ToA*.
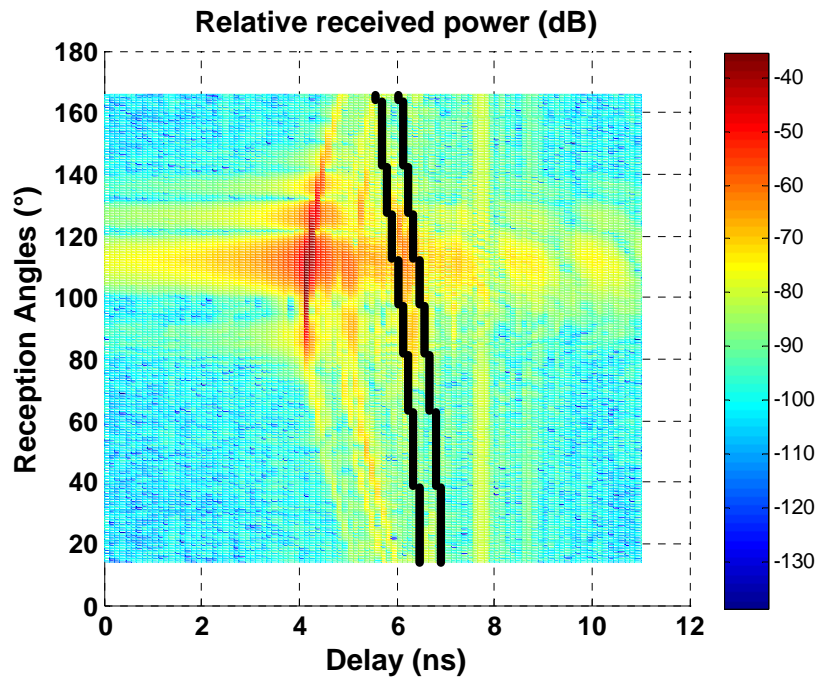
Figure 4.10: Measurements and selected components.

Once we have selected the desired components by time gating the black selection shown in Figure 4.10, we can extract the relative received power of these components, which will content diffusion in all cases and reflection in certain angles. Only in some angles does reflection overlap diffusion, and even in this case it is also considered in the simulations.

For example, the time-gated relative received power is shown for the crystal material when the transmitter is in place with an angle of 90º, as in Figure 4.11. In order to reduce the variability of the received power, we have windowed using 11 consecutive positions. Now, simulations will be performed in the same way as the measurements have been taken, and then the diffuse scattering parameters will be optimized.
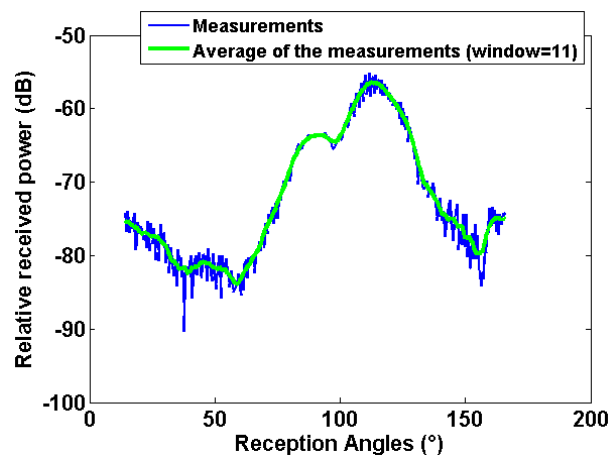
Figure 4.11: Measurements for glass and 90°.

4.2.5 Diffuse Scattering Parameters Estimation

As explained before, simulations have been performed by discretizing the material under study in squares of 10λx10λ. Then ray tracing is applied and *LoS*, reflection and diffuse scattering has been taken into account. Since diffuse scattering has a random phase, 40 iterations have been taken into account to account for this variability for each frequency and for each position. This phase corresponds to θ_s in (4.9). The *α* and *s* parameters from the model are varied from 2 to 10 and from 0.05 to 0.8. As we will see later, this will let us see the optimum value for each material.

We have used two functions to measure how similar the measurements and simulations are. Even if it is not usual and with no physical meaning, these functions with the variable expressed in dB give an accurate value of the minimum error.

The first function is simply the mean of the difference between measurements and simulations:

$$Mean = \frac{1}{N}\sum_{n=1}^{N}\left|Attenuation\_measured(dB)_n - Attenuation\_simul(dB)_n\right| \quad (4.11)$$

where *N* is 303 (all angular positions). The second function is the *Normalized Mean Squared Error (NMSE)*:

$$NMSE = \sqrt{\frac{\sum_{n=1}^{N}\left|Attenuation\_measured(dB)_n - Attenuation\_simul(dB)_n\right|^2}{\sum_{n=1}^{N}\left|Attenuation\_measured(dB)_n - \overline{Attenuation\_simul(dB)_n}\right|^2}} \quad (4.12)$$

4.2.6 Results and conclusion

The parametric analysis was performed for the three materials and for values of *S* and *α* in the range of [0.05–0.8] and [2–10] respectively. The results are given in *Appendix D*.

Table 4.1 summarizes the best fitting values. It is observed how glass has a very diffuse effect, which was expected since it does not have any rugosity. On the other hand, the plasterboard is the material which generates more diffuse scattering due to the

irregularities in its construction. With these results, accurate simulations can be made, taking into account each material and not the whole set of data, as is normally done in the literature.

Material	Directive		Lambertian
	S	α_R	S
Plasterboard (Ceiling)	0.5-0.6	5	0.5-0.6
Glass (Window)	0.07-0.1	2-10	0.07-0.1
Chipwood (from a cupboard)	0.4-0.5	2-5	0.4-0.5

Table 4.1: Best fitting diffuse scattering parameters for the three materials.

4.3 Indoor Multidimensional mm-w Channel Modeling and Characterization

In this Section, an extensive multidimensional analysis of Line-of-Sight (*LoS*) experimental data and ray tracing simulations at 60 GHz over a 9 GHz bandwidth are presented.

MIMO (Multiple-Input Multiple-Output) channel transfer functions were measured for 20 transmitting positions in an 80m^3 office. In addition, the *MIMO* channels were simulated in the frequency domain with the *3D ray tracing* tool taking description of the office and single-order diffuse scattering into account. For the sake of comparison, the Multipath Components (*MPC*) were extracted from both set of data using the high resolution estimator *RiMAX*. The main propagation parameters, such as the *RMS delay spread* and angular spread, are presented, and compared to other results published in the scientific literature.

Following this step, several clustering techniques such as visual inspection, *K-means*, and multipath component distance (*MCD*) were implemented and analyzed. Furthermore, a new clustering algorithm is proposed.

4.3.1 Scenario

The measurement scenario was a laboratory located on the first floor of the research building of the Universidad Politécnica de Cartagena, Spain. The laboratory size is approximately 4.5 x 7 x 2.5 m, and it is furnished with several closets, shelves, desktops, and chairs. In addition, the laboratory is equipped with several computers and electronic devices. The walls are typical interior walls made of plasterboard, and the floor and ceiling are made of concrete. In Figure 4.12, a top-view of the measured scenario is depicted, as well as the measured positions. 20 separated transmitter (*Tx*) locations and one receiver position (*Rx*) were considered for this study.

For all positions, a 0.5 m and 1 m distance was selected between each *Tx* row and column, respectively. All distances were measured with a laser to obtain the most accurate precision. It is noteworthy that a *LoS* existed for all positions.
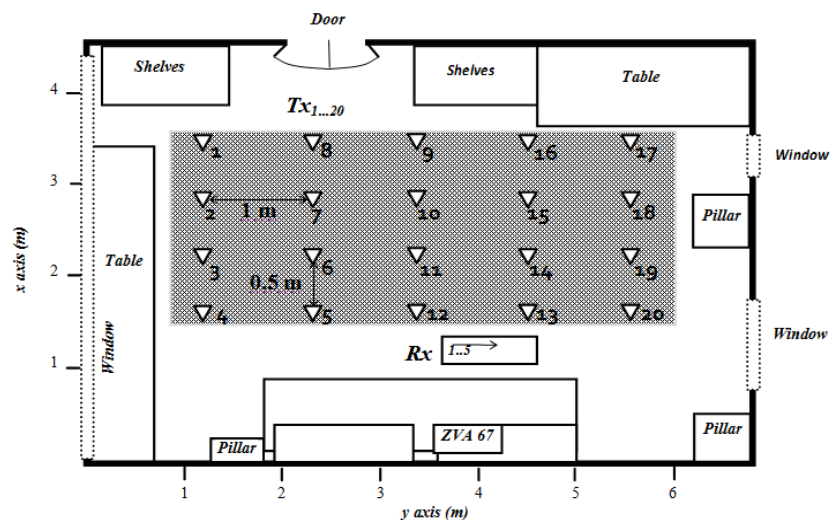
Figure 4.12: Indoor scenario of the measurements.

Figure 4.13: Photo of the indoor scenario of the measurements.

4.3.2 Experimental Set-up

The measurements were conducted using a channel sounder based on the Rhode ZVA67 *vector network analyzer* (*VNA*).

The measured frequency range was 57–66 GHz, using 4096 frequency points, with a 10 Hz intermediate frequency and a dynamic range of more than 100 dB. Two 25 dB gain low noise amplifiers are used in the transmission to compensate the attenuation of the cables (HXI HLNA-465). A scheme of the channel sounder is shown in Figure 4.14. The system is THROUGH calibrated to eliminate the effect of cables and amplifiers. The *Tx* and *Rx* antennas (Q-par QOM55-65 VRA) have omnidirectional patterns in the H-plane and 40°, 28°, and 21° beamwidth at half power in the E-plane at 55 GHz, 60 GHz, and 65 GHz respectively. The gain of the antennas increases from 4 dB to 5.4 dB in the 57-66 GHz frequency band (see Figure B.6 in the *Appendix B*). Their polarization is always vertical. The heights of the *Tx* and *Rx* antennas are 1.44 m and 1.54 m, respectively.
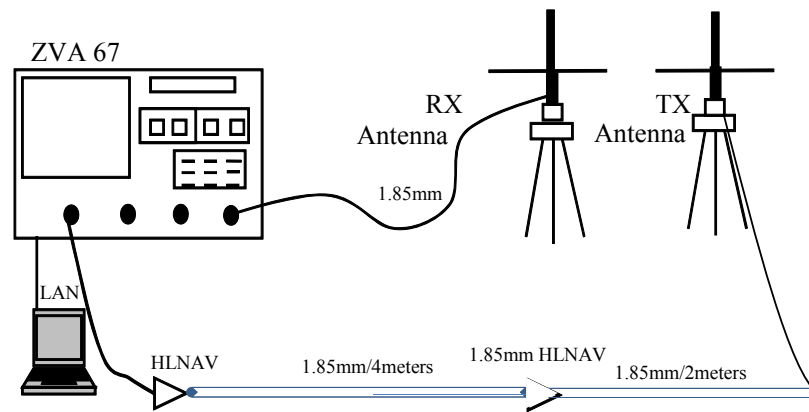
Figure 4.14: Scheme of the channel sounder.

A virtual uniform linear array (*ULA*) with 5 positions is used for *Rx* (y-axis orientation) whereas a 6 x 6 virtual uniform rectangular array (*URA*) is used in the *Tx*. This results in 180 possible channels. The inter element distance was set to 2 mm for both arrays. Figure 4.15 shows, on the right, the virtual transmitted matrix antennas and on the left, the five positions for the received antenna.
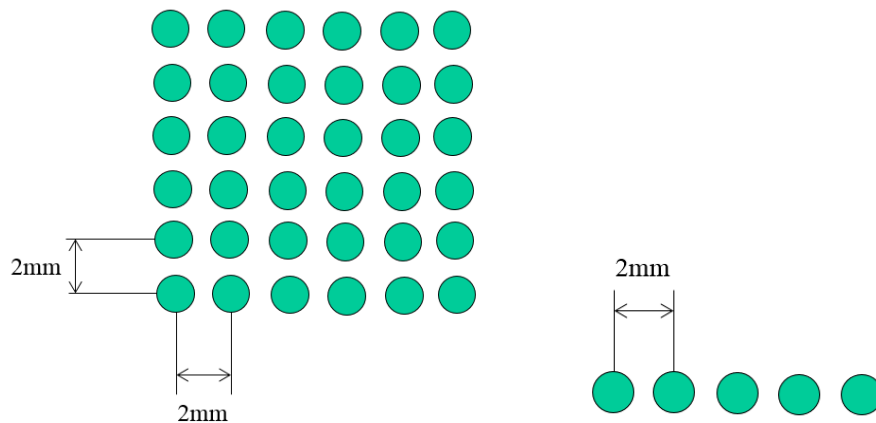
Figure 4.15: *Tx URA* and *Rx ULA*.

4.3.3 3D Ray Tracing Tool Simulations Parameters

A simplified, yet faithful, numerical model of the scenario has been developed and in which the main furniture is introduced. Suitable permittivity and conductivity values, constant through the whole bandwidth, were assigned to the scenario elements [Correia, 1994].
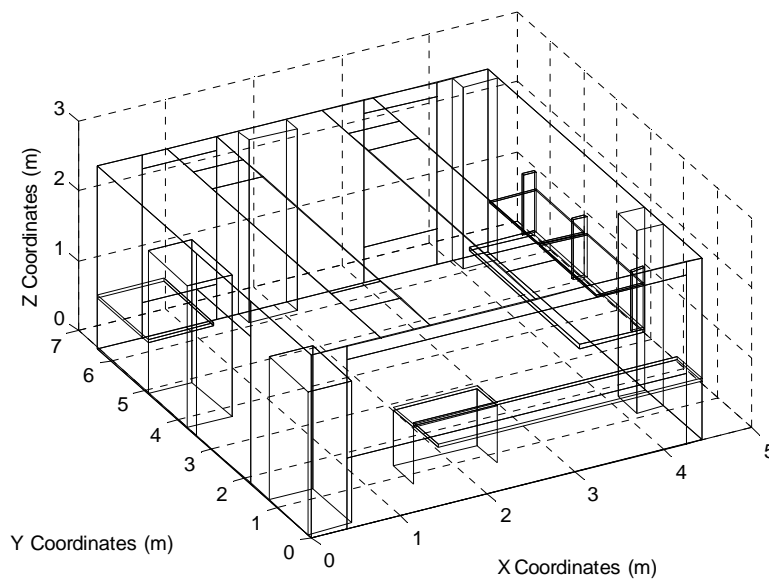
Figure 4.16: Simulated Office environment.

The *3D ray tracing (3D RT)* technique employed in this work is fully written in Matlab and provides the computation of the usual reflected and diffracted components. Furthermore, single-order diffuse components have been simulated with the optimum parameters for the directive model ($S = 0.6$ and $\alpha_R = 2$) found in section 4.1.5. The maximum number of reflections was set to 2, whereas the maximum number of reflections after diffraction was set to one. It must be outlined that no substantial difference was found between two and three reflections. Finally, we note that the radiating pattern of the antennas was included to adjust the complex gain of each path. However, the precision stage platform and mounting bracket were not included into the model.

For each *Tx – Rx* pair, *3D RT* simulations were performed over the same frequency points as for the *VNA*. This is simply done by summing the contribution of all waves for each frequency value to reconstruct the transfer functions *H* in the frequency domain. This simplifies the comparison between measurements and simulations. The classical *MPC* data model used in the literature and in this work is wideband in the time-delay domain. However, it is narrowband for the spatial domain (i.e. single frequency). Indeed, a wideband description of the spatial domain would imply measuring the radiation pattern for each frequency point which is simply not feasible. Hence, a sub-band could be selected from both measured and simulated channels to perform a parametric estimation of the *MPCs*.

In Table 4.2, a summary of the values used for the permittivity and conductivity is given.

Element	Material	Permittivity	Conductivity
Ceiling/Wall	Plasterboard [Lostan 2002]	2.81-0.046i	0.15
Floor	Concrete [Vaini 2010]	6.5-0.43i	1.43
Window	Crystal [Lostan 2002]	6.94-0.176i	0.59
Door	Wood [Correia 94]	1.54-0.095i	0.32
Closet/Table	Chipboard [Correia 94]	2.86-0.016j	0.32

Table 4.2: Used values for each element for *3D ray* tracing simulations.

In *Appendix A*, the reader could read more details about the *3D ray tracing tool*.

4.3.4 MPC Parameters Estimation

Both measured and simulated *MIMO* radio channels were processed with the *RiMAX* maximum-likelihood algorithm. This algorithm is a recently developed multidimensional maximum-likelihood high-resolution channel parameters estimator. It is based on the assumption that the radio channel can be modeled as a superposition of a number of finite specular-alike propagation paths (*MPC*) and dense multipath components (*DMC*). The algorithm iteratively seeks propagation paths and optimizes their characteristics. It does not require a prior knowledge of the number of dominant propagation paths [Richter, 2005].

The *DMC* is stochastic by nature and includes both diffuse scattering and paths that cannot be resolved. The incorporation of the *DMC* components into the data model was shown to improve the accuracy and validity of the estimated propagation paths [Richter, 2005]. The accuracy of the estimated parameters depends on the data model and on the calibration errors.

Hence, the purpose of estimating the parameters from the simulated channels instead of actually using those directly predicted by the *3D RT* is to make a fair comparison between measured and simulated data.

The variance of the measured noise was deduced from the measured channels for each position and added to the simulated channels since it is used in the estimator data model.

The following set of parameters is obtained for each multipath component *MPCi*:

$$MPC_i\left\{a_i, \theta_{TX,i}, \theta_{RX,i}, \varphi_{TX,i}, \varphi_{RX,i}, \tau_i\right\} \qquad (4.13)$$

where a_i $\theta_{TX,i}$ $\theta_{RX,i}$ $\varphi_{TX,i}$ $\varphi_{RX,i}$ τ_i are the complex amplitude, elevation angle of arrival and departure, azimuth angle of arrival and departure , and delay respectively.

To comply with the narrowband spatial model hypothesis discussed earlier, a 1.12 GHz bandwidth around 57.56 GHz (512 frequency points) was selected out of the 9 GHz available bandwidth. In addition, the whole *MIMO* array was selected to perform the estimation (6 x 6 uniform rectangular array (*URA*) for *Tx* and 5-element uniform linear array (*ULA*) for *Rx*). The 5-element *ULA* restricts the azimuth angular estimation between -90° and 90° but is here sufficient to grasp the physics of the propagation mechanisms. The elevation information, hidden within the *ULA* spatial steering array, is retrieved with a two-dimensional azimuth-elevation maximum likelihood approach.

Finally, we note that the radiation pattern of the antennas was not included into the estimator data model. Preliminary estimations from *3D RT* simulated transfer functions have shown that the azimuth and elevation angles are correctly estimated when using omnidirectional antennas at both *Tx* and *Rx* part. Also, the *MMSE* between the *3D RT* transfer function and estimated transfer functions by *RiMAX* was in the order of 0.05 dB. Due to the configuration of the room, simulation results have shown that the most energetic paths arrive with low elevation angles where the antenna gain is almost maximal.

4.3.5 Deterministic and Experimental mm-W Channel Modeling

4.3.5.1 Wideband Analysis

The wideband relative received power in dB can be computed from the *PDP* as the sum of all *PDP* components:

$$P_r = 10\log 10\left(\sum_i PDP(\tau_i)\right) \qquad (4.14)$$

where the *PDP* is computed as the mean value of the square of the 180 *inverse Fourier transform* of *H* obtained either from measurements or simulations. Simulation were performed by considering or not the scattering components. As an example, Figure 4.17 presents the *PDP* for position 3 with 9 GHz bandwidth. For the sake of clarity, no noise was added to the simulations. It is visually shown that the shape of the simulated *PDP*, where diffuse scattering has been introduced as indicated in section 4.2, matches well the measured one between 10 and 30 ns. However, the baseline of the simulated *PDP* diverges beyond 30 ns because the noise had not been taken into account in the simulation.
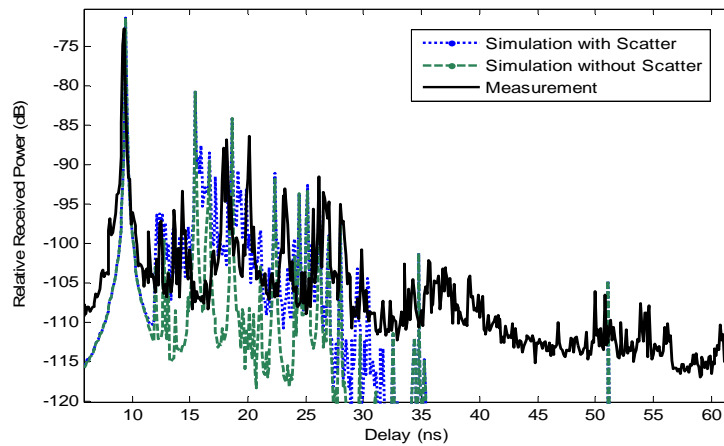
Figure 4.17: *PDP* for measurements, simulations w and w/o scatters.

Table 4.3 presents the wideband received power, *DS*, and *MED* for simulations (with and without diffuse scattering) and measurements with 9 GHz bandwidth for the first five *Tx* positions depicted in Fig 4.12. A 30 dB threshold was used to eliminate noise and low-power contributions for the computation of P_R, *DS*, and *MED*. A mean *RMS DS* of 4.1 ns was computed from the measured and simulated data using all positions. In

comparison with the literature, a 4.8 ns *RMS DS* was reported in [Fu, 2013] for a 28.2 m^2 room (3.7 ns for 32.9 m^2 in this work). A maximum excess delay of 29.8 ns and 27.2 ns were obtained using (2.8) from the measurements and simulations, respectively.

Furthermore, the results show that including diffuse scattering improves the accuracy of the simulations, the energy of the scattering component estimated by *RiMAX* being 10% of the total energy for all simulated positions. Evidently, the relative part of scattering energy would strongly increase for obstructed or non-line-of sight (*OLoS* or *NLoS*) scenarios since in *LoS* scenario, the *LoS* component is found to be 10 – 15 dB more energetic than multipath component.

The received power computed using (4.14) is displayed in Figure 4.18 for both measurements and simulations. From the averaged received power, a typical one-slope model was fitted to the data:

$$Pr(dBm) = PR_0 - n \cdot 10 \cdot log_{10}(d) \qquad (4.15)$$

where *PR$_0$* is the received power for a 1 m reference distance, *n* the decay factor, and *d* the distance between *Tx* and *Rx*.
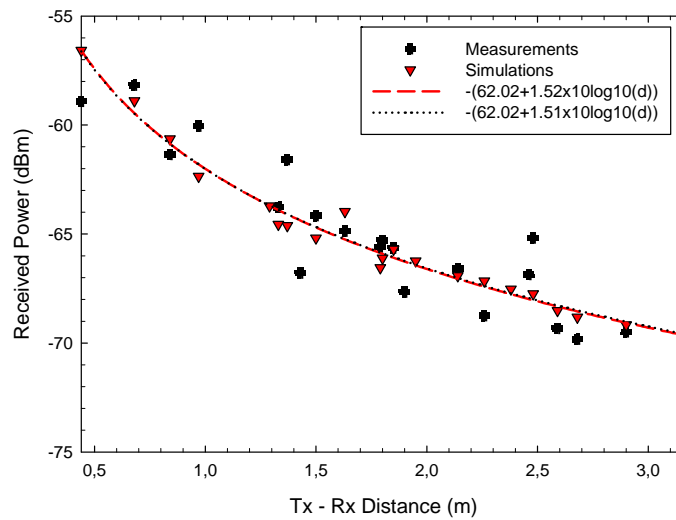
Figure 4.18: Simulated and Measured received power.

The one-slope models obtained from the measured and simulated data are in good agreement with a computed *decay factor* of 1.52 and 1.51, respectively. Values reported in [IEEE802.15.3, 2009] and [Fu, 2013] for *mm-W LoS* measurements are in the range of 1.2 and 2.0 respectively. Indeed, the authors in [IEEE802.15.3, 2009] explained that *n* can be

smaller than 2 when wave-guiding and reverberation effects are present resulting in power levels increase by multipath aggregation. In addition, a distribution of the measured and simulated results around the average received power Pr can be modeled by a zero mean Gaussian distribution X_{Pr}. A 2.17 dB and 0.23 dB standard deviation for X_{Pr} was found for the measurements and simulations, respectively.

4.3.5.2 Spatial Domain Analysis

The *MPCs* were extracted by *RiMAX* algorithm from both measured and simulated channel transfer functions over a 1.12 GHz bandwidth (Relative bandwidth less than 2% and thus satisfying the narrowband assumption). Once all *MPCs* are estimated, the total number of rays (*TNR*) is obtained after applying a 30 dB threshold to remove the weaker paths.

When computing the *RMS AS* with formula (2.12) an ambiguity can arise when the mean value of angle is around π, therefore the method consist of subtracting the mean angular value of estimated angular to centered the power angular spectrum around 0°.

Table 4.4 summarizes in details the parameters for the positions 1 to 5 extracted from both simulated and measured data, as well as the averaged values and standard deviation for the 20 positions. The average number of extracted *MPCs* (*TNR*) using *RiMAX* is 15 for the simulations and 60 for measurements. Here, the difference is attributed to the simplified modeling of the propagation scenario.

Finally, an AS value of 41.5° (63.6°) and 55.1° (65.5°) was computed for φ_{RX} $\left(\varphi_{TX}\right)$ from the simulations and measurements, respectively. Similarly, an AS value of 14.8° (24.3°) and 18.4° (16.6°) was computed for θ_{RX} (θ_{TX}) from the simulations and measurements, respectively.   In general, a larger spread is obtained from the measurements than the simulations due to the modeling of the room, as discussed previously. Nevertheless, the results can be considered quite satisfactory.

Authors from [Gustafson, 2014] measured AS φ_{TX}, AS φ_{RX}, AS θ_{TX}, AS θ_{RX} values of 40°, 17.2°, 11.4° and 17.2° degrees while we have measured 55.1°, 65.6°, 24.3° and 16.6° degrees. A large difference is observed between both AS φ_{RX}. This is attributed to the fact

that the authors in [Gustafson, 2014] used a URA for Rx whereas a ULA was chosen in this work. Hence, all rays are folded back into]-90°,90°[which results into increasing its angular spread.

Position	P_R(dB)			DS(ns)			MED(ns)		
	Meas	Sim w/o S	Sim w/ S	Meas	Sim w/o S	Sim w/ S	Meas	Sim w/o S	Sim w/ S
1	-68,1	-70,4	-69,6	4,0	4,0	4,2	27,1	39,9	39,9
2	-68,8	-69,9	-69,2	4,4	3,5	4,1	27,7	25,9	25,9
3	-68,4	-69,4	-68,7	4,3	3,5	4,1	30,0	22,9	22,9
4	-64,3	-68,5	-67,8	4,4	4,0	4,4	29,6	27,2	27,2
5	-65,4	-64,5	-64,1	3,3	2,8	3,4	36,6	25,3	25,3
<1-20>	-67,1	-67,8	-67,2	4,1	3,5	4,1	29,8	27,2	27,2
Std <1-20>	2,0	2,0	1,9	0,5	0,5	0,4	6,5	6,7	6,7

Table 4.3: Relative received power $P_R(dB)$, DS, and MED in 9 GHz from measured and simulated (w/ & w/o diffuse scattering) channels.

Position	Simulated Data w/ Diffuse Scattering				
	TNR	$AS_{\varphi_{RX}}$ (º)	$AS_{\varphi_{TX}}$ (º)	$AS_{\theta_{RX}}$ (º)	$AS_{\theta_{TX}}$ (º)
1	17	34,9	63,3	12,3	23,4
2	24	42,9	67,6	9,5	20,2
3	17	46,7	65,0	20,4	23,8
4	23	52,2	73,2	12,7	28,9
5	18	56,4	71,3	10,3	12,4
<1-20>	15	41,5	63,6	14,7	18,4
Std <1-20>	4,4	6,3	10,4	3,4	7,3
	Measured Data				
Position	TNR	$AS_{\varphi_{RX}}$ (º)	$AS_{\varphi_{TX}}$ (º)	$AS_{\theta_{RX}}$ (º)	$AS_{\theta_{TX}}$ (º)
1	79	53,9	80,6	26,5	17,9
2	37	42,4	86,7	20,1	14,6
3	51	47,3	85,2	21,8	17,8
4	34	50,6	75,6	19,0	12,6
5	82	73,0	58,2	26,8	16,6
<1-20>	59	55,1	65,5	24,3	16,5
Std <1-20>	19,8	10,1	16,2	3,0	3,3

Table 4.4 Extracted Parameters for Simulated and Measured Data.

4.3.6 Clustering

In this section, three classical clustering approaches have been applied to *MPCs* extracted from measurements and *3D ray tracing* simulations: visual inspection, *K-means* and *MCD* distance. Position 2 will be analyzed in detail as an arbitrary example. Since powers of the extracted *MPCs* exhibit a large dynamic range, our analysis was limited to *MPCs* with powers within 30 dB of the strongest component. For the measurements, there were 194 *MPCs* and 51 after using the threshold, and for simulations 90 *MPCs* and 17 after the threshold.

4.3.6.1 Visual Inspection

To begin with, the first step is to visually observe the data in order to classify the distribution of *MPCs*. For the visual inspection, a cluster can be identified as a set of *MPCs* with correlated *ToA*, *AoA* and *AoD*. Angles are defined with their azimuth and elevation. As shown in Table 4.4 the elevation angle spread for *AoA* and *AoD* are below 28.9° for most of positions showing that the elevation angular spectrum is very narrow. Therefore, the elevation will not be a useful parameter to distinguish cluster. In the following, *AoA* and *AoD* will be defined by their azimuth angle.

By observing the data, *MPCs* can be grouped by assuming a maximum deviation in the *ToA* and *AoA/AoD*. Let note *Cj*, the cluster *j* defined by its mean parameters as follow:

$$C_j = \left\{ \overline{TOA_j}, \overline{AOA_j}, \overline{AOD_j} \right\} \qquad (4.16)$$

$$MPC_i \in C_j; \left\{ \left| TOA_i - \overline{TOA_j} \right| < \Delta\tau \, \& \left| AOA_i - \overline{AOA_j} \right| < \Delta\theta^o \, \& \left| AOD_i - \overline{AOD_j} \right| < \Delta\theta^o \right\} \quad (4.17)$$

where in the simulation, $\Delta\tau = 5$ ns and $\Delta\theta^o = 20^o$.

Figure 4.19 presents the clustering results following the previous constraints for a) the simulated data, and b) the measured data for the third position. The different clusters are highlighted with either color circles or crosses or asterisks.
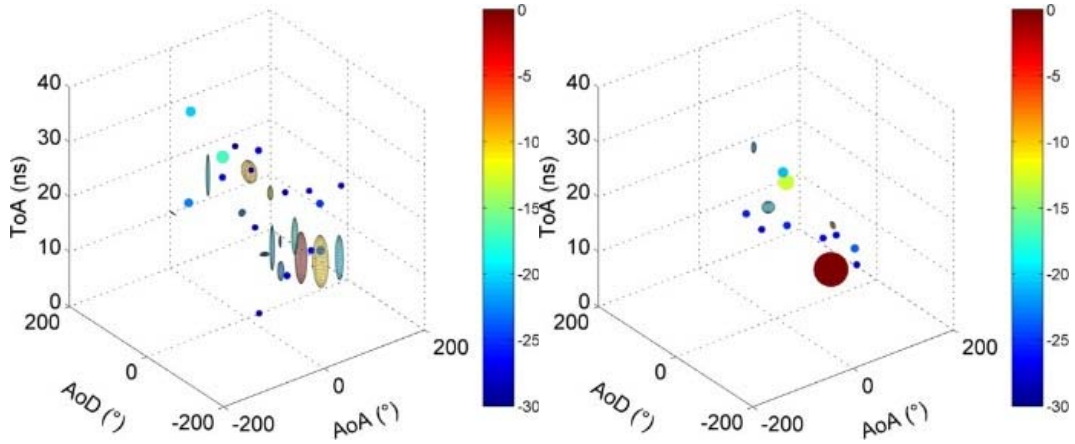
Figure 4.19: Clustering a) measured and b) simulated data in position 2 using visual inspection.

We see in Table 4.5 that 30 and 13 clusters are identified for measurements and simulations respectively. In Table 4.5 the maximum size of a cluster, as well as the mean size are summarized for all algorithms. The size of a cluster has 3 dimension, being *AoA*, *AoD* and *ToA*.

4.3.6.2 K-Means

This is one of the most commonly used clustering algorithms. It classifies groups of rays based on similar features into *K* clusters which are previously defined by the user. This aspect is one of the problems of this algorithm since we do not know exactly *a-priori* the number of clusters. The *KMeans* algorithm identifies each cluster by its centroid position in the parameter space. Each *MPC* is assigned to the cluster centroid with smallest distance. The algorithm iteratively optimizes the positions of the centroids in order to minimize the total distance from each *MPC*. A common used distance is the well-known Euclidean distance where the distance is calculated for each dimension (*ToA, AoA, AoD*) separately. Another distance is the multipath component distance (*MCD*) where the metric scales the data to enable joint clustering [Czink, 2006].

For our goal, this is alleviated by applying the *MCD* distance since it is more accurate for *MPCs* [Wang, 2006]. This distance is computed as:

$$MCD_{ij} = \sqrt{\left\|MCD_{AoA,ij}\right\|^2 + \left\|MCD_{AoD,ij}\right\|^2 + MCD_{\tau,ij}^2} \qquad (4.18)$$

Where the angular data can be expressed as:

$$MCD_{AoA/AoD,ij} = \frac{1}{2} \left\| \begin{pmatrix} \sin(\theta_i)\cos(\varphi_i) \\ \sin(\theta_i)\sin(\varphi_i) \\ \cos(\theta_i) \end{pmatrix} - \begin{pmatrix} \sin(\theta_j)\cos(\varphi_j) \\ \sin(\theta_j)\sin(\varphi_j) \\ \cos(\theta_j) \end{pmatrix} \right\| \qquad (4.19)$$

And the delay distance:

$$MCD_{\tau,ij} = \xi \cdot \frac{|\tau_i - \tau_j|}{\Delta\tau_{max}} \cdot \frac{\tau_{std}}{\Delta\tau_{max}} \qquad (4.20)$$

with $\zeta = 2.5$ as a typical delay scaling factor [Gustafson, 2014], τ_{std} is the standard deviation of the delays and $\Delta\tau_{max} = \max_{ij}\left\{|\tau_i - \tau_j|\right\}$.

Basically, the algorithm involves the random selection of K initial centroids. Then, each point is assigned to a closest centroid by *MCD* distance and the collection of points close to a centroid form a cluster. The centroid is changed according to the rays in the cluster and this process finishes when the rays stop changing their clusters.

One important point is that the number of clusters must be fixed at the beginning. For example, Figure 4.20 shows the results for $K=11$ for measurements, and $K=4$ for simulations. We have run the maximum number of centroids for which the algorithm converges, and the results are shown in Table 4.5, i.e. 11 and 4 clusters for measurements and simulations, respectively.

The problem of non-convergence is that *K-means* is very sensitive to outliers and noise. It does not work well with non-circular cluster shape and clusters which do not have well defined centers. For this reason, and taking into account that clusters should group *MPC* within a reasonable delay and angular spread, it was found that *K-means* cannot be applied to the investigated measurements.
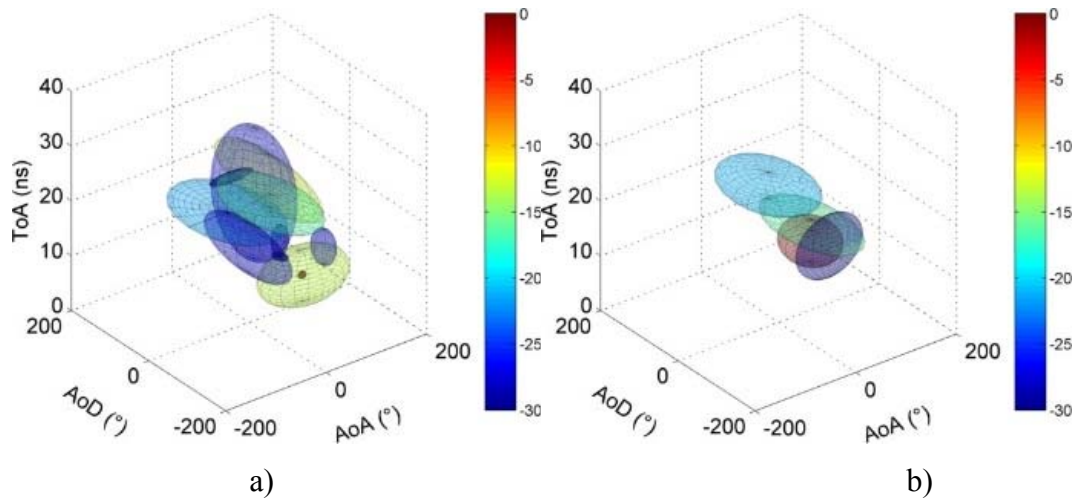
Figure 4.20: Clustering from measured data a) and simulated data b) at Position 2 using *K-means*.

We have also included the results for *K-means power*, a variation of *K-means* that takes into account the amplitude of the rays, but which present the same convergence problems.
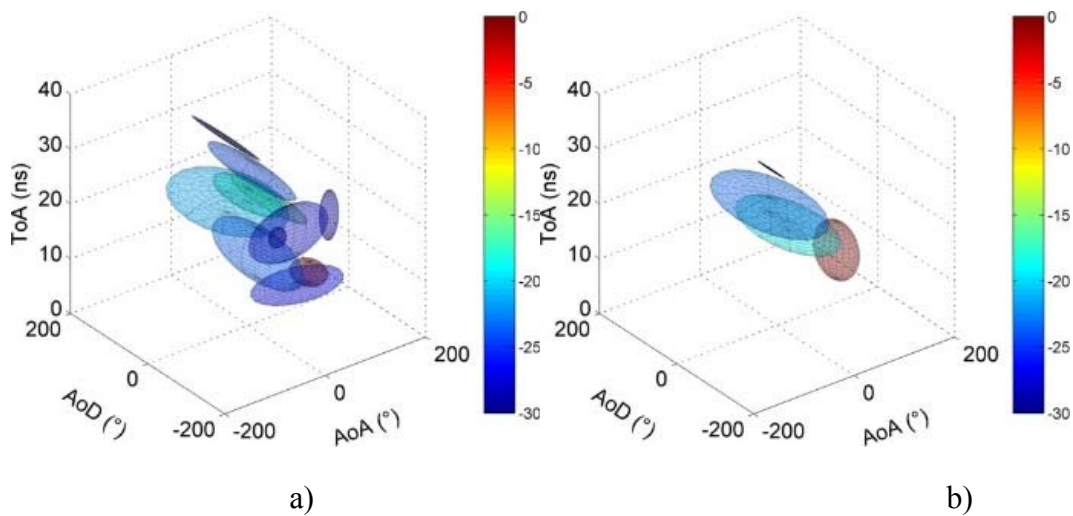
Figure 4.21: Clustering from measured data a) and simulated data b) at Position 2 using *K-means Power*.

4.3.6.3 MCD Distance

Another option for clustering is to obtain the clusters as presented in [Gustafson, 2014], using the *MCD* distance. First, this method consists of sorting the rays with respect to their delays. Second, the *MCD* is computed between rays with shortest delay. Third, a threshold of 0.25 is used to group rays. In other words, they group rays with *MCD* less than 0.25 making up a new cluster. Steps are repeated until all rays are grouped. The results are displayed in Figure 4.22 with $\zeta = 3$.

a)   b)
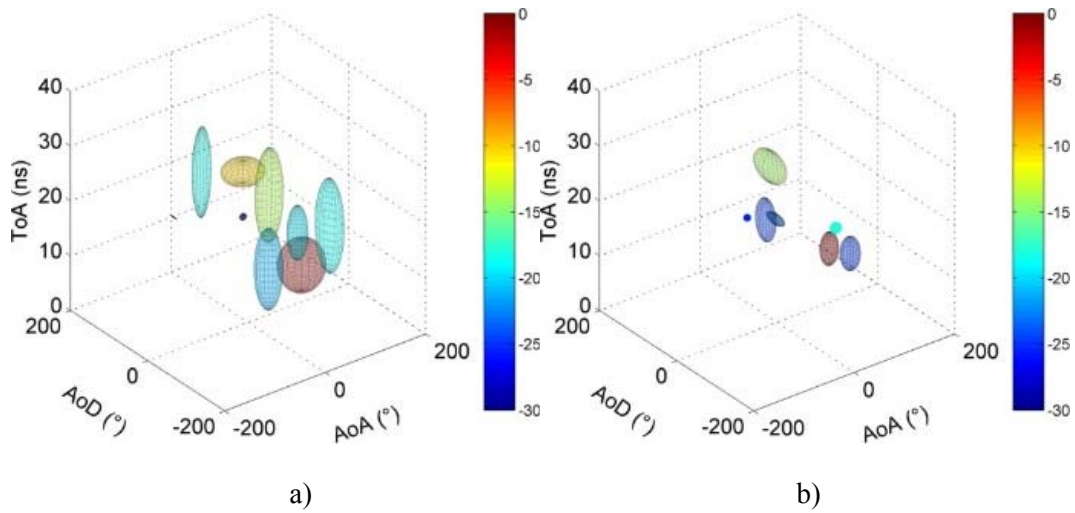
Figure 4.22: Clustering from measured a) and simulated b) data at Position 2 using *MCD<0.25*.

In Table 4.5, it is showed a total number of clusters of 9 and 7 for measurements and simulations respectively, i.e. it groups very different *MPCs* in one cluster. Let us now analyze the *CDF* of all *MCD* distances for all positions using the simulated data, and showed in Figure 4.23.
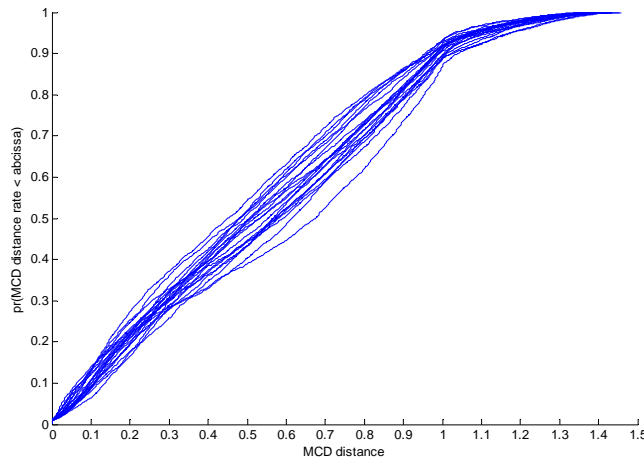
Figure 4.23: CDF of the MCD distance from simulated data with all positions.

As we can see, if we choose a unique *MCD* distance for all positions (as 0.25 used by the authors of [Gustafson, 2014]), it leads to different statistics in the distribution, this means that at different distances we have different *CDFs*. Hence, a threshold for every position must be computed. This threshold is calculated as the maximum distance from which two *MPCs* are considered independent (i.e. belong to two different clusters). Based on the earlier visual inspection study, the threshold was set such that 2 rays separated by 40° for both *AoA* and *AoD* and 10 ns for time-delay. A 0.1 and 0.08 threshold is obtained

for Position 2 from the measurement and simulated data, respectively, and results are presented in Figure 4.24 using these thresholds

a)   b)
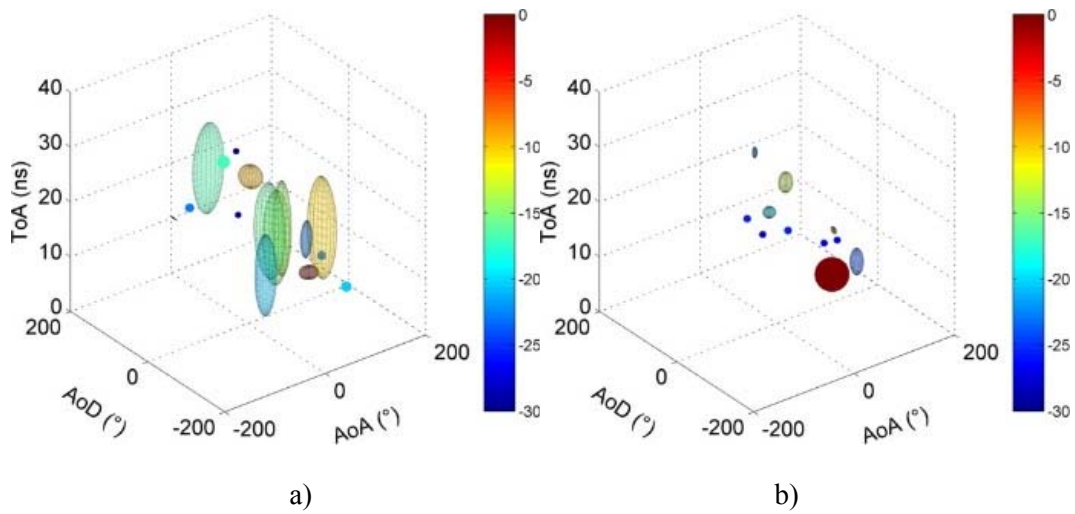
Figure 4.24: Clustering from measured a) and simulated b) data at Position 2 using *MCD<0.1* and 0.08 respectively.

The number of clusters is presented in Table 4.5 and it has increased to 16 and 11 for measurements and simulations respectively.

4.3.6.4 New Algorithm for Automated Identification of Clusters

First, the ray with maximum amplitude is chosen. Then, rays that fall within a given *MCD* distance are searched for. This distance is defined according to the scenario and physical assumption. In our case, it is a *MCD* distance of two rays differing by 40 º and 10 ns. If no such rays are found, a new cluster is defined with that single ray. If a ray is found, it is checked whether it has not been already assigned to another cluster. Depending on the *MCD* distance to the new ray or old cluster, its correspondence can be modified. The flowchart in Figure 4.14 gives an overview of our approach.
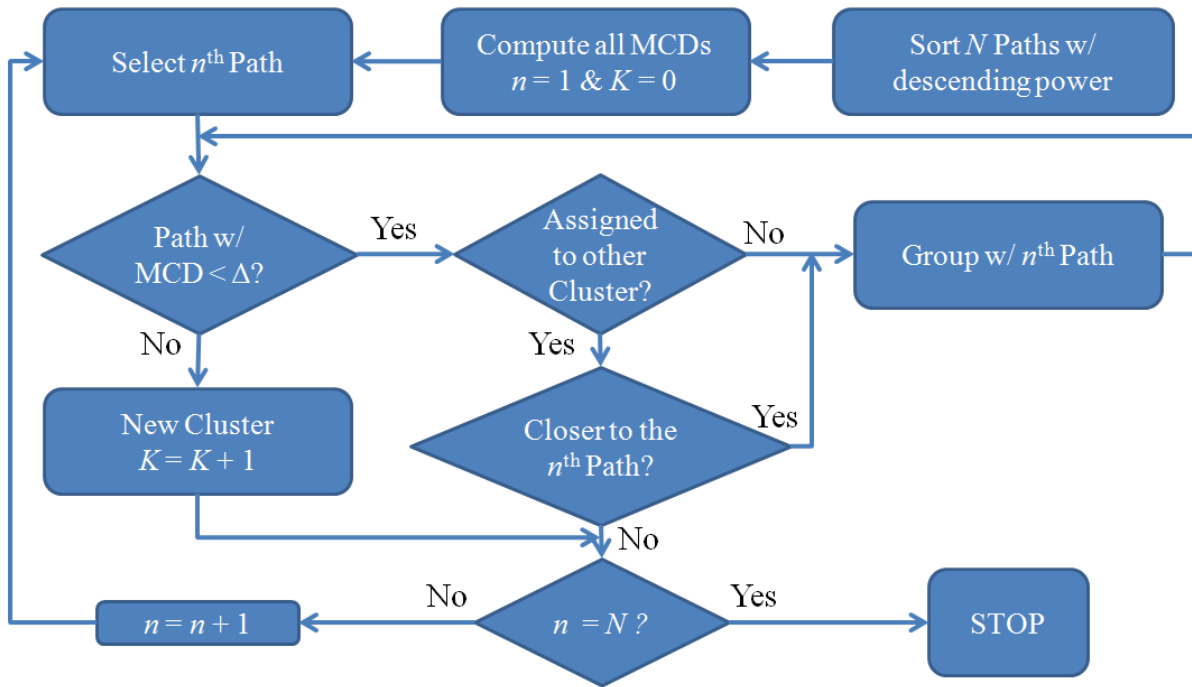
Figure 4.25: Flowchart of the new clustering algorithm.

In Figure 4.26 the clustering results using our algorithm are shown for Position 2. It gives results quite similar to those obtain with visual inspection (Table 4.5). 29 and 13 clusters are found for measurements and simulations, respectively.

a)   b)
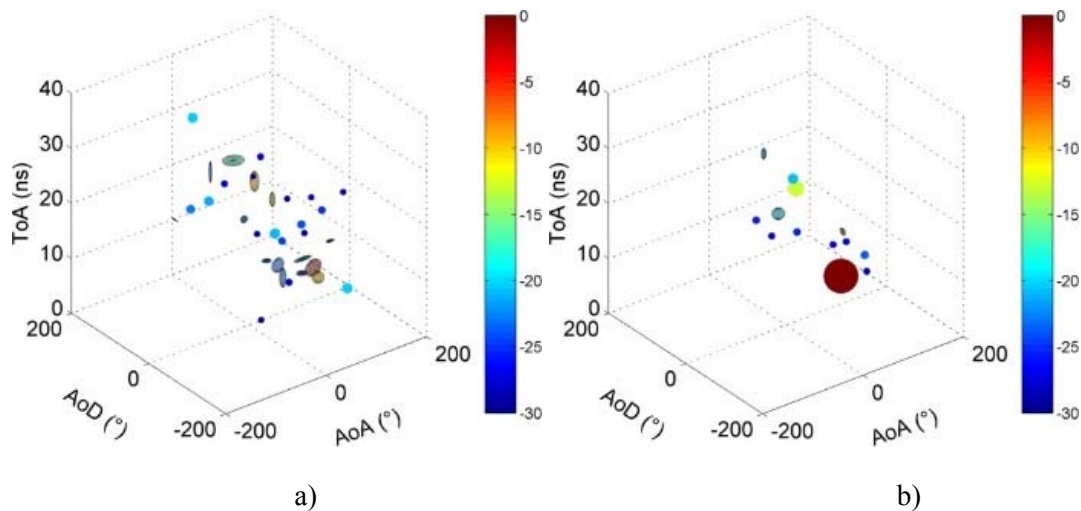
Figure 4.26: Clustering from measured a) and simulated data b) at Position 2 using the new algorithm.

		AoA Range (º)		AoD Range (º)		ToA Range (ns)		N of Clusters
		Mean	Max	Mean	Max	Mean	Max	
K-means	Measurements	76,9	168,6	127,1	276,2	6,4	23,9	11
	Simulations	19,8	141,3	20,6	229,3	1,2	11,6	4
K-means Power	Measurements	74,7	168,6	134,2	242,9	4,3	9,9	11
	Simulations	84,6	168,6	134,5	256,9	4,7	10,3	4
MCD distance	Measurements ($\Delta 0,25$)	63,0	161,5	57,0	243,9	9,5	17,3	9
	Simulations ($\Delta 0,25$)	46,6	161,5	49,6	242,9	5,4	17,2	7
	Measurements ($\Delta 0,1$)	21,4	62,8	20,8	65,5	7,2	18,6	16
	Simulations ($\Delta 0,08$)	8,7	38,3	9,6	65,5	2,35	17,4	11
Visual Inspection (angle<40º and tau<10ns)	Measurements	4,6	21,2	6,9	34,7	2,1	9,4	30
	Simulations	1,7	21,1	2,5	20,5	0,28	2,2	13
New Approach	Measurements ($\Delta 0,1$)	7,41	36,7	5,9	33,3	0,7	3,8	32
	Simulations ($\Delta 0,08$)	4,7	33,7	3,4	20,5	0,5	3,8	13

Table 4.5: Clustering results from measured and simulated data for all positions with K-means, K-means Power, MCD, Visual Inspection, and new algorithm. Mean and Max refer to the averaged and maximum dimension of the cluster.

At this point, we have shown from indoor measurements and ray tracing simulations results how different clustering approaches bring different statistical results. From Table 4.5 we can compare the number of clusters, identified by each approach, as well as the range of *ToA/AoA/AoD*. From the authors' point of view, the key point is the definition of a cluster or, in other words, what spreads can be used for the *ToA/AoA/AoD* in a cluster. For example, tens of degrees seem reasonable for the localization technique.

4.3.7 Conclusions

In this Section, it has been presented an extensive multidimensional analysis of *LoS* experimental data and ray tracing simulations including single-order diffuse scattering in the millimeter-wave frequency band for 20 transmitting positions in an office.

The results support the idea that diffuse scattering, which accounts for 10% of the total energy, must be taken into account in simulations to faithfully reconstruct channel transfer functions. However, second-order scattering might not be necessary to assess the propagation parameters of the *mm-W* channels. The *RiMAX* algorithm was used to extract the *MPC* parameters from both measured and simulated data set.

From this analysis, a good agreement is reached between the time-delays and power angular spreads computed from the *RT* and measured channels. Those values are also found to be similar to other results published in the scientific literature.

The results show that even a raw description of the environment can be used to predict *mm-W* propagation with ray tracing.

Moreover, the classical clustering approaches such as visual inspection, *K-means* and *MCD* distance have been used to analyze *MPCs* extracted from measurements and *3D* ray tracing simulations. Finally, a new method for automated identification of clusters for indoor *mm-W* channel has been proposed. The novel algorithm has showed the good agreement with results from visual inspection.

4.4 Experimental Comparison between Centimeter- and Millimeter-Wave Ultra-Wideband Radio Channels

This Section analyses, in an indoor environment, propagation issues of centimeter- and millimeter-wave ultra-wideband radio channels to determine the precise differences between them. From the point of view of propagation, these two frequency bands have been compared using the highest possible bandwidth, regardless of system constraints.

Firstly, line-of-sight (*LoS*) is considered and later, obstructed line-of-sight (*OLoS*) situations are considered by studying the effects of cardboard and metallic obstacles. A

vector network analyzer was used as a part of a channel sounder and the measurements were performed using similar conditions and equipment (antennas have a slightly different gain but similar radiation patterns for both frequency bands). Thus, we compared both propagation channels within several GHz in terms of wideband *path loss*, *delay spread*, *Rician K factor* and *spatial correlation*.

4.4.1 Scenario

The measurements were performed in a laboratory located on the first floor of the research building of the Technical University of Cartagena, in Spain. In Figure 4.16, the measurement scenario is depicted. The laboratory size is approximately 4.5 m ×7 m ×2.5 m (length, width and height) cubic meters and it is furnished with several closets, shelves, desk and chairs. Moreover, the laboratory is equipped with several computers and electronic devices. The walls are typical interior walls made of plasterboard and the floor and ceiling are made of concrete.

We have measured *LoS* situations for positions *Tx1*, *Tx2* and *Tx3*, as shown in Figure 4.27 and we have blocked the *LoS* component for *Tx2* using cardboard and metal obstacles. In both cases, the surface dimensions of the blocking material were around 1.5 × 1.5 m in the *LoS* propagation direction. During the measurements, the laboratory was unoccupied.
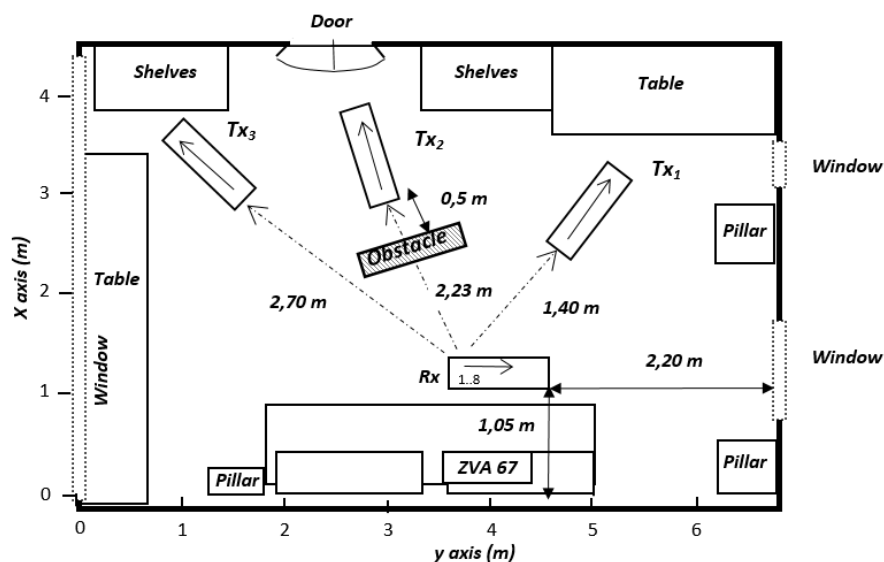
Figure 4.27: Measurement scenario.

Figure 4.28: Photos of the measurement scenario.

4.4.2 Channel Sounder

A vector network analyzer was chosen as the main instrument of the channel sounder for the two frequency bands. For the *mm-W* frequency band measurements, the measured frequency range was 57–66 GHz, using 2048 frequency points; 10 Hz being the intermediate frequency. For the *cm-W* frequency band, the measured frequency range was 2–10 GHz, also using 2048 frequency points with an intermediate frequency of 100 Hz.

In both cases, we used omnidirectional antennas with nearly similar radiation patterns and gains. For 2–10 GHz, we used two omnidirectional Electrometrics EM6116 [Electrometric, 2014] with a measured gain of 0.1, 3.4 and 3.7 dBi at 2, 6 and 10 GHz, respectively. At mm-W, we used two omnidirectional antennas Q-par QOM55-65 VRA [Q-PAR, 2014] with gain of 3.3, 3.1 and 3.0 dBi at 55, 60 and 65 GHz, respectively. The polarization of the antennas was always vertical.

In the 57–66 GHz measurements, we used two 25-dB amplifiers to compensate the attenuation of the cables. The insertion losses of the cables were around 6 dB/m at 66 GHz but they are smaller at 2–10 GHz (2.13 dB/m at 10 GHz, continuous line in Figure 4.18). The power transmitted by the vector network analyzer was set to -10 dBm in both cases and the dynamic range was greater than 100 dB. Back-to-back measurements were performed to compensate the frequency response of cables and amplifiers. The height of the antennas was 1.5 m.

Three blocks of positions with *LoS* condition were measured, as shown in Figure 4.27: *Tx1*, *Tx2* and *Tx3*. Every block involves the transmitter antenna which was placed in a

1-m-long linear positioned. The antenna moved along 950 mm (controlled by the dashed line in Figure 4.18). In the case of 2–10 GHz, the chosen spacing was 10 mm (95 positions per block every $0.33*\lambda_{10GHz}$) and for 57–66 GHz it was 2 mm ($0.44*\lambda_{66GHz}$). The latter was measured in groups of nine positions (along 18 mm) and every 36 mm (a total of 171 positions per block, 19 groups of 9 positions) to reduce the measuring time. Figure 4.29 give an overview of antennas position at *mm-W* and in *UWB* bandwidth.
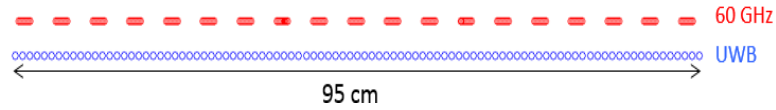
Figure 4.29: Scheme of a block: 19 groups of 9 positions at 60 GHz and 95 positions at 2-10 GHz.

For *Tx2*, additional measurements were performed by obstructing the *LoS* component by means of cardboard boxes and metallic obstacles. This was performed for *Tx2* only for convenience in the scenario, keeping the *OLoS* condition along the 1-m-long array. We will denote *OLoS1* and *OLoS2* for the cardboard and metallic obstacles, respectively. The position of the successive obstacles 1.5 × 1.5 m is shown in Figure 4.16.

In all cases (*LoS* and *OLoS*), for the receiver antenna which was placed in another 1-m-long linear positioned, eight positions were chosen for each transmitter block (*Tx1*, *Tx2*, *Tx3*). Each pair of receiver positions was separated by an electrical distance below λ/2; for the 57–66 GHz frequency band, 2 mm was chosen, whereas 10 mm was chosen for the 2–10 GHz band. During the measurements the room was unoccupied, and each one meter measurement took nearly 24 hours.

4.4.3 Results

$H_{p,m}(f)$ is the frequency transfer function measured for the three blocks of measurements (where the antenna gain has been removed), where *m* is the number of transmitting positions (95 and 171 for the 2–10 and 57–66 GHz, respectively), the number of receiving antennas *p = 8* and the sampled frequency *f = 2048* (for both bands).

Let us then define the channel impulse response $h_{p,m}(\tau_n)$:

$$h_{p,m}(\tau_n) = \frac{1}{N_F} \sum_{i=1}^{F} H_{p,m}(f_i) e^{j2\pi f_i \tau_n} \qquad (4.21)$$

where τ_n is the delay ranging from 0 to 255.88 ns for 2–10 GHz and 227.44 ns for 57–66 GHz and N_F is the total number of measured frequencies (i.e., the total number of sampled frequencies). The Power Delay Profile (*PDP*) is defined as the ensemble of different impulse responses, which in our case, is within the receiver positions:

$$PDP_m(\tau_n) = \frac{1}{P} \sum_{p=1}^{P} \left| h_{p,m}(\tau_n) \right|^2 \qquad (4.22)$$

where *P* is the number of channel impulse responses (i.e., total number of receiving antennas).

4.4.3.1 Path Loss

The mean wideband path loss can be defined either in the time domain or in the frequency domain as given in (2.1).

Figure 4.30 shows the continuous wideband path loss for the two frequency bands for *LoS*, *OLoS1* and *OLoS2* because *Tx2* overlaps *Tx1* and *Tx3* in the final and initial positions respectively. The average values are summarized in the Table 4.6. The mean path loss is a continuing increasing function with similar path loss exponent of 1.29 and 1.31 for *UWB* and *mm-W* respectively. In the previous section 4.3.5.1, we obtained path loss exponents 1.52 and 1.51 for the measured and simulated data. They are different due to the fact that before, the 20 positions were spread over all the room, while here less positions are measured (with more spatial resolution).

A low variability in the measurements is observed, especially for *LoS*, even if the three blocks are located randomly within the room (we have not measured in a straight line, i.e., see Figure 4.27). This low variability relies on the very large bandwidth and the ease of resolving multipath components, contrary to what occurs with narrowband systems. A typical one-slope model was given in (2.3).
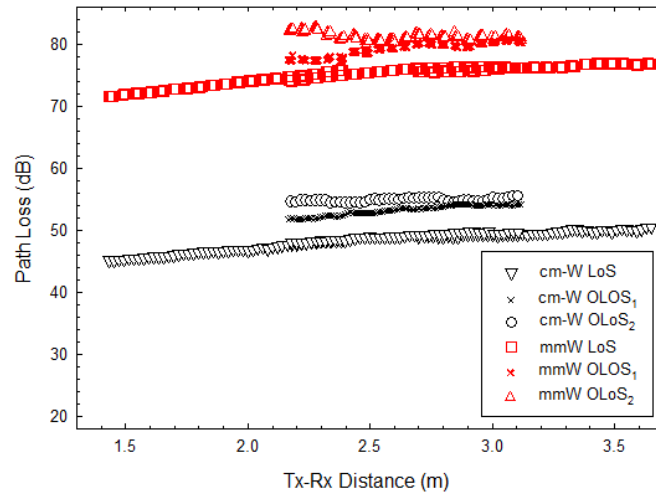
Figure 4.30: Measured wideband *path loss*.

Regarding *LoS*, Table 4.6 summarizes the best fitting parameters for the one slope model presented in (2.3), as well as the mean values of the path loss for *Tx2* under *LoS* and *OLoS* conditions.

	MEAN PATH LOSS MODEL (dB) USING (2.3)	
	2–10 GHz	**57–66 GHz**
LoS (Tx1-2-3)	$PL_0 = 43.2$ dB, n = 1.31	$PL_0 = 69.9$ dB, n = 1.29
	Tx2 MEAN PATH LOSS (dB)	
	2–10 GHz	**57–66 GHz**
LoS	49.6	73.6
OLoS$_1$	52.7	79.1
OLoS$_2$	54.8	81.3

Table 4.6: *Path Loss Model* parameters for *LoS* scenario and for *Tx2* for *LoS*, *OLoS$_1$* and *OLoS$_2$* scenario.

A slope of 1.31 for 2–10 GHz and 1.29 for 57–66 GHz are obtained. In the case of *mm-W*, these values are within the range of 1.2 and 2.0 reported in [IEEE 802.15.3, 2009] and [Garcia-Pardo, 2012] for *mm-W LoS* measurements.

For *cm-W* with vertical polarization, in [Garcia-Pardo, 2012], the measured slope is 1.3 for *LoS*. In [Peter and Keusge, 2009], the measured slopes are similar at 1.33 and 1.31 for 60 and 5 GHz, respectively. The measured standard deviations are 0.28 dB and 0.33, respectively.

Regarding *OLoS* scenario, the situation is clearly different to *LoS*, because close to the obstructing object, the *LoS* component is totally blocked, whereas when the antenna is further removed, some energy arrives at the receiver. This explains a constant or even decreasing path loss effect.

Furthermore, we found it more interesting to compute the average values within block two for *OLoS* scenario, such that we could see the additional losses due to some materials and the results are also summarized in Table 4.6 (last 3 rows). Furthermore, the length of *Tx2* is insufficient to construct a distance-dependent model. In the Table 4.6, it is observed that the additional attenuation due to the cardboard box is 3.1 dB for *cm-W* and 5.5 dB for *mm-W*, whereas for the metallic obstacle the attenuation is 5.2 and 7.7 dB for *cm-W* and *mm-W*, respectively. For *cm-W*, the cardboard does not eliminate completely the *LoS* component, which will be observed in the *K factor* and in the *RMS delay spread* later.

4.4.3.2 RMS Delay Spread

In this subsection, we study the time dispersion of the *PDPs*. In Figure 4.31, we observe the *PDP* averaged over the first 10 cm for *Tx2* in *LoS* scenario.
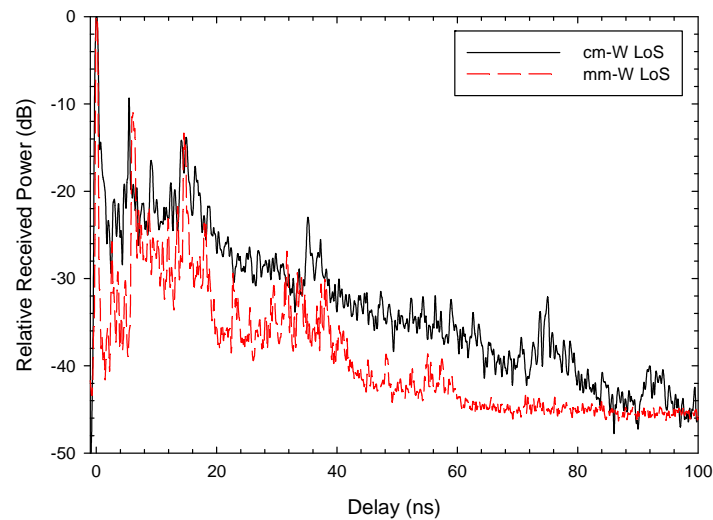
Figure 4.31: *LoS PDPs* for Tx2 in cm-W and mm-W, PDP averaged within 10 cm.

Visually, it is observed how the main specular components fit the same delays. Note that, for visual comparison, we have normalized the *LoS* contribution to 0 dB and 0 ns in both cases. The decrease of the power in delay is higher at 60 GHz, as well as the amplitude of the peaks compared with the diffuse component, due to the higher

attenuation in the *mm-W* frequency band. This means that multiple reflections have more influence in the *cm-W* band and thus that in the simulation tool, the reflection coefficient must be frequency dependent.

From the *PDP*, we can compute the *RMS delay spread* which gives us a measure of the maximum data throughput without any equalization at *Rx*. We have used a threshold to eliminate noise and low-power contributions (20 and 30 dB), such that comparison with other publications is easiest. We have also computed the maximum excess delay.

Firstly, it is important to clarify that our measurement setup has 8- and 9-GHz bandwidth for 2–10 and 66–57 GHz, respectively, which leads to a time resolution of 0.125 and 0.11 ns, respectively. Most other references measure with a 1-GHz frequency band with 1-ns resolution.

In Figure 4.32, the measured *RMS DS* is shown for *LoS* and *OLoS*, using a 30-dB threshold, as in [Peter and Keusge, 2009].
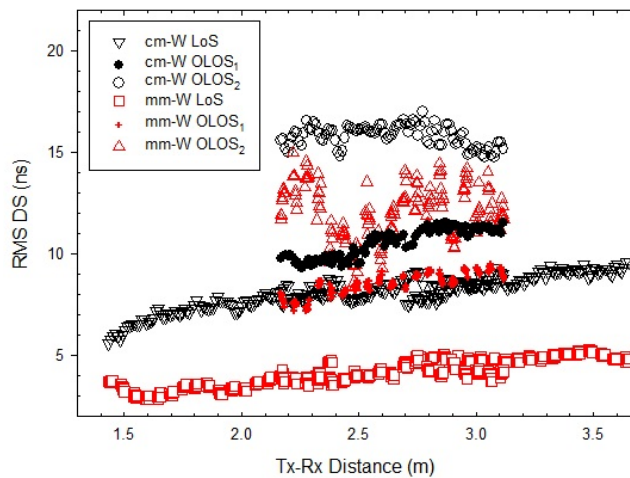
Figure 4.32: Measured *RMS DS* for a 30-dB threshold.

A one-slope model was used to fit the measurements [Rappaport, 2002]:

$$RMS_{DS}(ns) = RMS_0 + n_{DS} \cdot 10 \cdot \log_{10}(d) + X_{RMS} \qquad (4.23)$$

where RMS_0 is the *RMS DS* at a reference distance (1 m in this case), n_{DS} is the *RMS DS* decay factor and X_{RMS} is the standard deviation of the centered Gaussian distribution; the obtained values are summarized in Table 4.7.

In [Peter and Keusge, 2009], for *LoS*, the mean *RMS DS* was 6.29 ns for 60 GHz and 14.7 ns for 2 GHz. Our mean values, for similar distances, are around 4 and 8 ns for 57–66 GHz and, 2–10 GHz respectively (for a 30-dB threshold). These smaller values of *RMS DS* could possibly be attributed to the wider bandwidth in our experiment and to the arrangement of furniture in the office. Indeed, the tables in our laboratory were situated against the walls, whereas in [Peter and Keusge, 2009] the tables were arranged in the center of the room. The standard deviations for the two frequency bands using (4.23), for *LoS*, are 0.34 and 0.3 ns for *cm-W* and *mm-W*, respectively.

In Table 4.7, we also have included the mean values of *RMS DS* for *LoS* and *OLoS*, for block 2, for the 20- and 30-dB thresholds. The cardboard increases by 2 ns the spread for *cm-W*, because some energy is still transmitted at those frequencies, contrary to what happens for *mm-W*, where it increases by 4 ns. This will be justified in the next section by analyzing the *K factor*. Regarding *OLoS$_2$*, the delay values show a considerable increase in both bands.

		2–10 GHz	57–66 GHz
RMS Delay Spread LoS (Tx1-2-3) Fitting Curve Model (30 dB)		$D_0 = 5.44$ $n_d = 0.67$	$D_0 = 2.08$ $n_d = 0.52$
LoS-Tx2	**20 dB**	4.2	2.8
	30 dB	8.3	4.1
OLoS$_1$-Tx2	**20 dB**	6.7	6.1
	30 dB	10.4	8.1
OLoS$_2$-Tx2	**20 dB**	12.3	8.5
	30 dB	15.8	12.1

Table 4.7: *RMS delay Spread* (ns) Model using (4.23) for *LoS* with Threshold of 30 dB and Average *RMS delay spread* (ns) for Threshold of 20 and 30 dB for *Tx2*.

In Table 4.8, we can observe the maximum excess delay for the 20- and 30-dB thresholds. For example, for 20 dB, we see that in *OLoS$_2$*, the length of the response is multiplied by *3.5* for both frequency bands. However, for cardboard, it is not affected much for *cm-W* but is affected for *mm-W*.

		2–10 GHz	57–66 GHz
LoS-Tx2	**20 dB**	25	14.3
	30 dB	63.6	30.7
OLoS₁-Tx2	**20 dB**	27.1	32.2
	30 dB	68.7	67.4
OLoS₂-Tx2	**20 dB**	75.4	53.1
	30 dB	114	110.1

Table 4.8: Maximum excess delay (ns) for threshold of 20 and 30 dB in Block 2.

4.4.3.3 Fast Fading Distribution – Rician K factor

We have compared the measured data with *Rayleigh*, *Weibull*, *Rician*, *Nakagami* and a *Log-normal* distribution in the frequency domain within a certain bandwidth and then used the *Kolmogorov–Smirnov* [Papoulis, 2002] test to decide the distribution that best fits the experimental results. By analyzing the entire bandwidth in bands of 500 MHz, a *Rician* distribution appears to be the optimum for all distances and frequencies [Martinez-Ingles, 2013]. This bandwidth has been chosen since *UWB* channeling is around this order [Molisch, 2005]; and in case of *mm-W*, a coherence bandwidth for a value of 0.9 was measured for 58.7 MHz [Al-Nuaimi, 2002], therefore it guaranties 10 independent blocks for each measured transfer function. We have checked that propagation characteristics of the distribution of the amplitude of the electric field do not change within this bandwidth. We have to take into account that:

$$x = H(f, position), \qquad 0 < f < 500 MHz \qquad (4.24)$$

Furthermore, the results are almost independent of the frequency throughout the measured frequency band.

The mathematical expression of the *Rician* probability density function is:

$$f\left(x \mid v, \sigma_{RICE}\right) = \frac{x}{\sigma_{RICE}^2} \exp\left(\frac{-\left(x^2 + v^2\right)}{2\sigma_{RICE}^2}\right) I_0\left(\frac{xv}{\sigma_{RICE}^2}\right) \qquad (4.25)$$

where $I_0(\ )$ is the modified *Bessel function* of the first kind with order zero and v and σ_{RICE} are parameters to be adjusted. The best-fitting resulted in a *Rician* distribution. From the mean and variance of the *Rician* distribution, it is possible to estimate the *Rician*

K factor, which is defined as the quotient of the signal power in the dominant component by the (local mean) scattered power [Abdi, 2001].

For computing *K factors*, a Matlab function *MLE* is used. This function returns maximum likelihood estimates for the parameters of a *Rician* distribution. Then, (4.26) is used to obtain the *K factor*.

$$K_{Factor}\left(dB\right) = 10\log\left(\frac{X_{param1}^{\,2}}{2X_{param2}^{\,2}}\right) \qquad (4.26)$$

where X_{param1} and X_{param2} are the returned parameters by the *MLE* function.

We have plotted the estimated *K factors* for *LoS* and for the central frequencies of 6 and 60 GHz over 500 MHz in Figure 4.33.

A decrease of the *K factor* is found of more than 10 dB for 60 GHz and around 8 dB for 6 GHz at 1.5 m. These values decrease to 3 dB in block 3 (further positions), where both scatter plots converge. It is comprehensible that multiple reflections are attenuated much more in the *mm-W* frequency band and therefore, when *LoS* is dominant, the *K factor* will be greater.
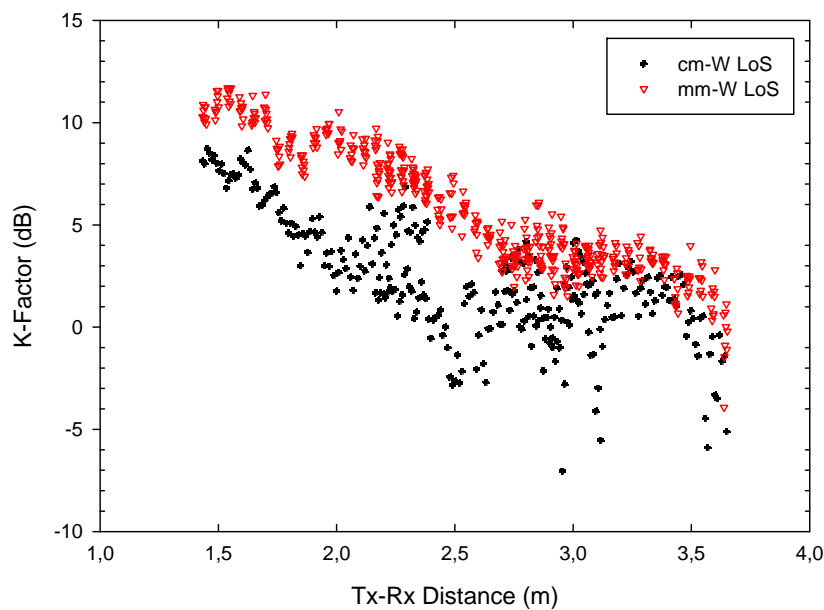
Figure 4.33: Measured *K factor* for 6 and 60 GHz.

In Table 4.9, the averaged measured *K factor* for block 2 is shown. We observe that the cardboard does not modify the statistical distribution for *cm-W* but it does for *mm-W*. This is related to previous results due to the penetrability of waves through the cardboard in the lower band (see *K factor*). For metal obstacles, the *K factor* decreases to values close to -20 dB in both cases, which implies *Rayleigh* distributions.

	6 GHz	60 GHz
	K (dB)	K (dB)
LoS	4.6	6.7
OLoS₁	3.8	-2.7
OLoS₂	-19	-17.5

Table 4.9: Averaged *K-factor* for Block 2 at 6 and 60 GHz.

4.4.3.4 Spatial Correlation

Finally, we compute the *spatial correlation* in the frequency domain (correlating the measured channel transfer functions), which measures the similarity between two received signals separated by a certain distance. For the three blocks and scenario (*LoS, OLoS₁* and *OLoS₂* in block 2) we define the reference frequency channel response at the first position of the array $H_{1,m}(f)$, ($m = 8$ different channel transfer functions and one for the first position of each block *Tx1,Tx2* and *Tx3*) and we compute the complex correlation with all measured frequency channel responses $H_{p,m}(f)$ within the linear positioner (at each position p) with $H_{1,m}(f)$, i.e., $\left| corr\left(H_{1,m}(f), H_{p,m}(f) \right) \right|$. Note that the observation is in frequency domain. Table 4.10 summarizes the distances where the correlation drops to 0.9, 0.7 and 0.5 expressed in millimeters, interpolating to extract the exact distances (the distance between antenna elements is 2 mm).

$$\rho^{1,p}(f) = \frac{E\left[\overline{H_{1,m}(f)} \cdot \overline{H_{p,m}(f)}^* \right]}{\sqrt{E\left[\overline{H_{1,m}(f)}^2 \right] \cdot E\left[\overline{H_{p,m}(f)}^2 \right]}} \qquad (4.27)$$

Where $\overline{H_{1,m}(f)}$ and $\overline{H_{p,m}(f)}$ are the centered $H_{1,m}(f)$ and $H_{p,m}(f)$ respectively.

	2–10 GHz			57–66 GHz		
	0.9	0.7	0.5	0.9	0.7	0.5
Block 1 LoS	13.1	28.7	93.5	4.3	11.1	18.7
Block 2 LoS	12.5	26.9	85.9	1.33	10.6	15.4
Block 2 NLoS$_1$	11.5	22.9	35.7	0.72	4.6	14.4
Block 2 NLoS$_2$	5.6	13.1	18.2	0.30	0.9	1.5
Block 3 LoS	12.1	24.4	75.2	0.79	6.2	13.5

Table 4.10: Correlation Distance expressed in millimeters.

From the Table 4.10, we can see that in *LoS*, by increasing the distance between the *Tx* and *Rx* (block 3 is further than block 2 and this is further than block 1), the distance to obtain a certain correlation decreases. For example, we need 28.7, 26.9 and 24.4 mm for each block (from 1 to 3) for 2–10 GHz and 11.1, 10.6 and 6.2 mm for 57–66 GHz, to obtain a correlation of 0.7. We can see that this distance is around half that for the *mm-W* frequency band. This means that by increasing to *mm-W* frequency from *cm-W* (nearly increasing the frequency by 10), it is possible to reduce the physical distance by half and still obtain the same de-correlation. This distance is only double in *mm-W* because in *cm-W*, multiple reflections are less attenuated. This is explained also by the smaller *RMS DS* values and higher *K* values (see 4.3.3.2 and 4.3.3.3 for *RMS DS* and *K* values respectively).

On the other hand, the mean wavelength in the frequency band 2–10 GHz $\lambda_{2-10GHz}$ is 50 mm, whereas at 57–66 GHz $\lambda_{57-66GHz}$ is 4.9 mm. If we convert the distances presented in Table 4.10 to electrical distances, we obtain Table 4.11. Now by fixing again a *correlation* of 0.7, which is the generally accepted value for considering de-correlation in *MIMO* systems [Verdone, 2002], the electrical distance for *LoS* for blocks 1, 2 and 3 is 0.57, 0.54 and 0.49 times $\lambda_{2-10GHz}$, respectively, for *cm-W* and 2.26, 2.16 and 1.26 times $\lambda_{57-66GHz}$, respectively, for *mm-W*. This means that at *mm-W*, the multipath components are much less important and the distance to de-correlate two signals in *LoS* is around five times greater in terms of the electrical distance.

	2–10 GHz $(\lambda_{2-10GHz})$			57–66 GHz $(\lambda_{57-66GHz})$		
	0.9	**0.7**	**0.5**	**0.9**	**0.7**	**0.5**
Block 1 LoS	0.26	0.57	1.87	0.87	2.26	3.82
Block 2 LoS	0.25	0.54	1.72	0.27	2.16	3.14
Block 2 OLoS$_1$	0.23	0.46	0.71	0.15	0.94	2.94
Block 2 OLoS$_2$	0.11	0.26	0.36	0.06	0.18	0.30
Block 3 LoS	0.24	0.49	1.5	0.16	1.26	2.75

Table 4.11: Correlation Distance expressed in wavelength.

Then, if we focus on block 2 we can compare *LoS*, *OLoS$_1$* and *OLoS$_2$* (values in Table 4.10, block 2). For example, with a *correlation* of 0.7, in block 2 we need 26.9 mm for *cm-W* for *LoS*. If a cardboard box interferes with the *LoS* component, this distance is reduced to 22.9 mm and to 13.1 mm if the obstacle is metal. The reduction for the cardboard is not large because we have seen before that the *K factor* decreases by only 1 dB and the *RMS DS* by 2 ns, i.e., the cardboard does not block completely the *LoS* component. However, for *mm-W*, it decreases from 10.6 mm for *LoS* to 4.6 mm with cardboard and to 0.9 mm with metal. These results are consistent with values of *RMS DS* and *K factor*.

If we perform the same analysis for block 2 in terms of wavelengths (Table 4.11), we find that the relationship (correlation distance in *cm-W* compared with distance in *mm-W*) is around 2.5 for the cardboard and around 1 for the metal obstacle, i.e., there is not much difference between them. The same result/conclusion was observed in the *K factor* calculation. *OLoS$_2$* is approximately *Rayleigh* at *mm-W* and *cm-W*; therefore, the de-correlation distance in terms of electrical distance is the same, whereas for *OLoS$_1$* we have a situation in between *LoS* and *NLoS*.

4.4.4 Conclusions

In this Section, we have studied indoor propagation phenomena at two different frequency bandwidths: 2–10 (*cm-W*) and 57–66 GHz (*mm-W*). Using similar conditions and equipment, we have measured the radio channel using omnidirectional antennas in an indoor environment for *LoS* and *OLoS* by obstructing the *LoS* component with cardboard boxes and metal obstacles. *Path loss*, *delay spread*, *spatial correlation* and *statistical distribution* were subsequently used to assess the major difference in the propagation

mechanisms from one band to the other. Thus the relative amplitude of the *LoS* component compared to the other ones (reflected ad diffused ones) is more important for *mm-W* than for *cm-W* due to the strongest attenuation of the multipath component. In the *mm-W* frequency band, this leads to smaller *RMS DS* values, higher *K factors* and higher de-correlation electrical distances. Also, we have found that the propagation in presence of some materials, such as cardboard, behave differently in the two frequency bands. For *LoS*, at *mm-W*, the multipath components are much less important and the distance to de-correlate two signals is around five times greater in terms of electrical distance and two times greater in physical distance to obtain the desired de-correlation.

In *OLoS*, the electrical distances to de-correlate two signals when metal obstacles are present is the same and is around 0.2λ for a correlation of 0.7, whereas with the cardboard boxes, the situation is closer to *LoS* in *cm-W* and closer to metal for *mm-W*.

4.5 Experimental Evaluation of an Indoor MIMO-OFDM System at 60 GHz Based on the IEEE 802.15.3c Standard

This section presents an evaluation of the performance of a *MIMO-OFDM* millimeter-wave system based on the standard *802.15.3c* and by considering experimental *MIMO* channel transfer functions.

The environment and experimental set-up are the same as those described in 4.3.1 and 4.3.2, respectively.

Prior to *PHY* layer simulation, channel parameters such as wideband path loss, correlation and capacity are assessed in the frequency band specified in *IEEE 802.15.3c*. These parameters will be useful to help in the interpretation of the *PHY* layer performances described in the second part of this section. Finally, the throughput for different space-time *MIMO* strategies following the *IEEE802.15.3c* standard is studied for different antenna element configurations.

4.5.1 Transmitter and Receiver System Configurations

From the transmitting 6x6 *MIMO* array, four configurations for the transmitter have been studied, named Conf 1, Conf 2, Conf 3, and Conf 4, selecting four antennas among the 36 positions. In Table 4.12, a schematic draw summarizes the position of the four selected *Tx* antennas among the 36 available. At the receiver, the 4 elements of the *ULA* are in the same orientation than the one in Conf 2.

Conf 1	Conf 2	Conf 3	Conf 4
X O O O O O	X X X X O O	X O O O O X	O O O O O O
X O O O O O	O O O O O O	O O O O O O	O O O O O O
X O O O O O	O O O O O O	O O O O O O	O O X X O O
X O O O O O	O O O O O O	O O O O O O	O O X X O O
O O O O O O	O O O O O O	O O O O O O	O O O O O O
O O O O O O	O O O O O O	X O O O O X	O O O O O O

Table 4.12: Transmitter System Configurations.

4.5.2 IEEE 802.15.3c Frequency Bands

Among the 9 GHz bandwidth, we have considered the four frequency bands proposed in the *IEEE 802.15.3c* standard [IEEE 802.15.3, 2009]. A preliminary study has shown that the channel characteristics computed in each subband are similar, so we will show the results related to channel 4: 63.720–64.800 GHz, which operates in the higher frequency range. From the measurements, we have interpolated the exact 512 frequencies.
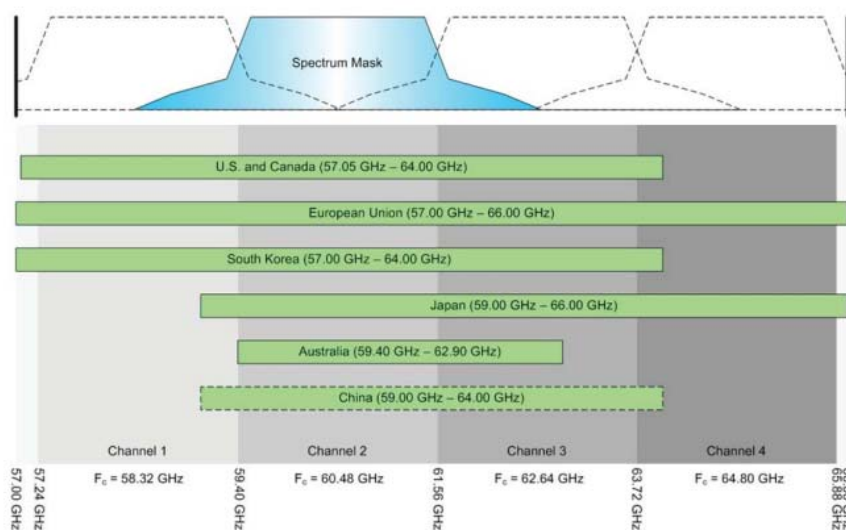
Figure 4.34: The 4 frequency bands considered in the *IEEE 802.15.3c* standard [IEEE 802.15.3, 2009].

4.5.3 Received Power, Correlation and Capacity

Figure 4.35 shows the *measured relative received power* for channel 4 (computed using 4.14). A 13 dB attenuation is observed at distance *Tx-Rx* of 3 m, and the one slope path loss model is also given in the figure (measuring a decay factor of 1.51) taking into account that the transfer function is store on 20 positions of the *Rx* array. In the following, the noise floor is assumed to be at -79.8 dBm leading to a *SNR* in *SISO* case varying from 12 dB at 0.5 m to 0 dB at 3 m. It would be important to mention that the transmitting power corresponds to the upper limit of -78 dBm/Hz given by the standards.
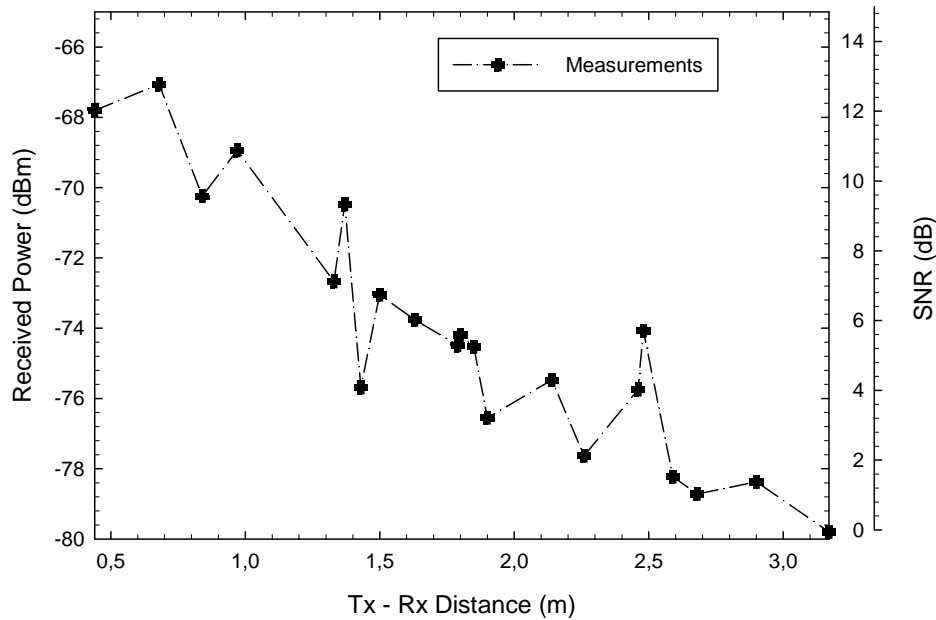
Figure 4.35: Relative Received Power and SNR for channel 4.

The mean *correlation* between all transmitting antenna elements [Sanchis, 2012] is shown in Figure 4.36. (Since *Rx* is kept constant for all configurations, we only show the *Tx correlation*.)
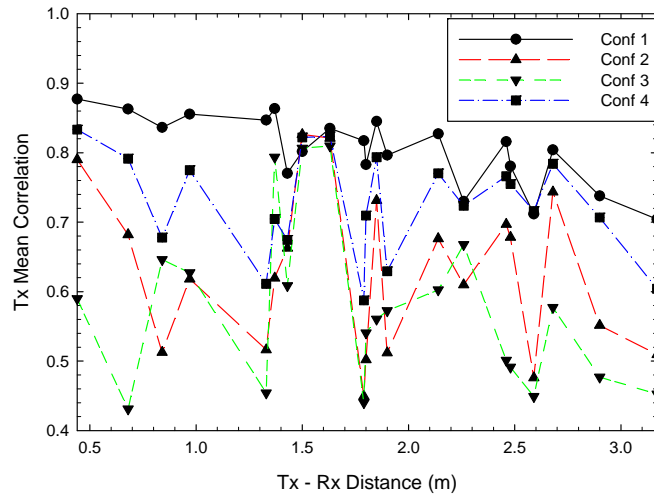
Figure 4.36: Mean Transmitter Correlation for channel 4.

Conf 3 has the lowest *correlation* which was not surprising since the distance between antennas is the largest, equal to 10 mm or 20λ. If we now compare Conf 1 and Conf 2, it appears that this last configuration presents a higher *correlation*, despite the fact that the distance between array elements is the same. A possible interpretation is that the *LoS* component presents a phase variation must larger in Conf 1 than in Conf 2 due to the alignment of the successive positions of the *Tx* antenna relative to the direction *Tx-Rx* (Table 4.12) .

Lastly Conf 4 has all elements very closed (see Table 4.12), so the *correlation* is very high but remains smaller than Conf 1.

The theoretical channel *capacity* depends both on *correlation* and *SNR*. However, if a constant *SNR* of 10 dB is considered, the variation of the *capacity* would be analysis only by the *correlation* (Figure 4.37).
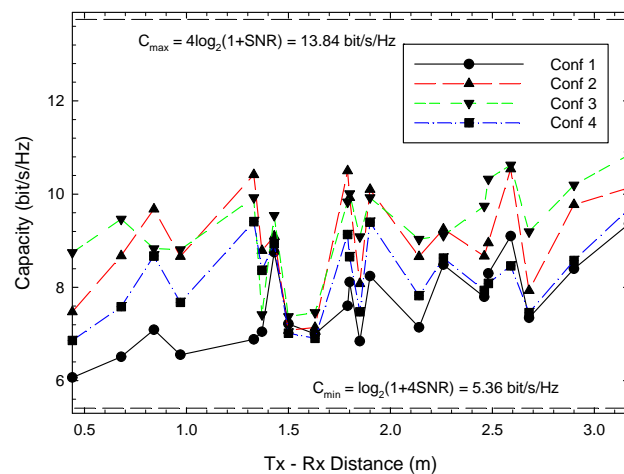
Figure 4.37: Capacity for a fixed SNR of 10 dB for channel 4.

As expected, the *capacity* is between the maximun and minimum theoretical capacities, i.e. that resulting from an i.i.d 4x1 *MISO* system (5.36 bit/s/Hz) and that resulting from an i.i.d 4x4 *MIMO* system (13.84 bit/s/Hz). The *capacity* and *correlation* have mirrored shapes, as the *correlation* increases the *capacity* decreases and vice versa. Similarly to the *correlation*, one can conclude that the maximum *capacity* is obtained with Conf 3 and the worst with Conf 1. Moreover, the *capacity* is an increasing function with distance.

However, a real system depends on the *SNR*, so we also compute the *capacity* using the measured *SNR* (Figure 4.35). We see that *capacity* is now a decreasing function with distance, the *SNR* having a stronger effect than the *correlation* on the *capacity* (Figure 4.38).
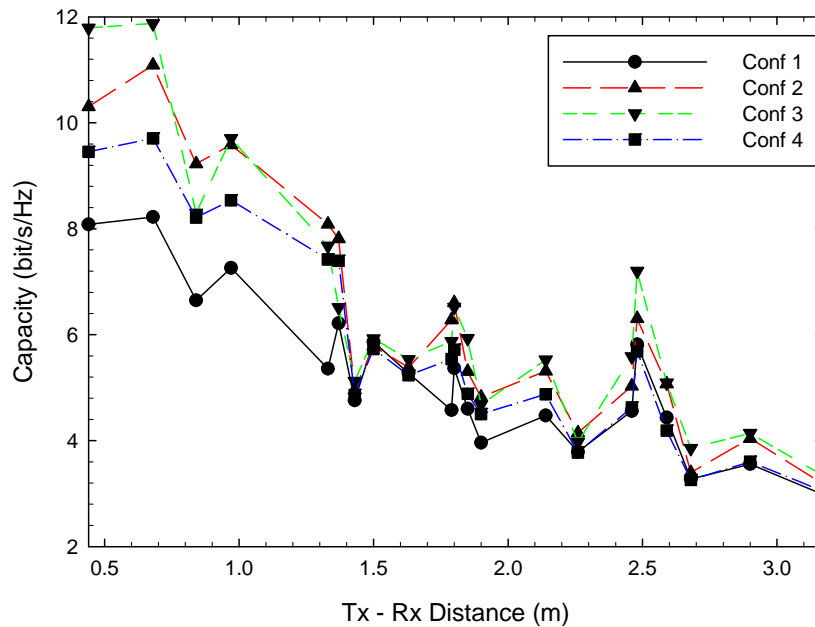
Figure 4.38: Capacity for the measured SNR for channel 4.

Comparing the configuration of the antennas, at short distances Conf 2 and Conf 3 outperform the others, and as we move away from the receiver the *SNR* decreases and beyond 1.5 m, the differences between the *capacities* becomes less noticeable.

4.5.4 Evaluation of the Throughput

Now the performance of systems based on *IEEE 802.15.3c* associated with different space-time coding strategies for indoor environments will be evaluated in terms of the throughput.

A summary of the specifications of *OFDM* based radio systems are summarized in Table 4.13. Two different modulation schemes are considered, i.e. quadrature phase shift keying (*QPSK*) and 64 quadrature amplitude modulation (*64QAM*), with two coding rates: 1/2 and 5/8.

Parameter	Value
Sampling Rate	2640 MHz
FFT points	512
# of subcarriers used for data	352
CP points	64
Modulation type	QPSK, 64QAM
Forward error correction	Structured LDPC
Coding rate	1/2, 5/8

Table 4.13: System parameters from the IEEE802.15.3c Standard for Throughput Evaluation.

Two *STBC* architectures are considered, either Orthogonal (*OSTBC*) or Quasi-Orthogonal (*QSTBC*) for *4x4 MIMO*, whose rates are 1/2 and 1, respectively. The symbol detection method is based on the Minimum Mean Squared Error (*MMSE*) algorithm. We will consider the *4x4 MIMO* and compare it with the *SISO* to study the benefits of the multi-antenna system.

The throughput of the system is calculated based on *OFDM* transmission. It is simply given by *Rb(1-PER)*, where *Rb* is the bit rate at the physical layer, and *PER* is the packet error ratio derived by the simulations. The *PER* is evaluated after the transmission of 1000 packets, in which each packet contains a payload of 1000 bits, leading to a minimum detectable $PER \leq 10^{-3}$. The available throughputs are defined as the maximum throughput from among all the standardized specifications for the coding rates and modulation schemes. The *Rb* at the physical layer used according to the modulation and coding scheme (*MCS*) is displayed in Table 4.14.

MCS	Coding Rate Modulation	SISO /4x4-QSTBC (Gbps)	4x4-OSTBC (Gbps)
1	1/2 QPSK	1.54	0.77
7	5/8 64QAM	5.77	2.88

Table 4.14: Theoretical Bit Rate for each Modulation and Coding Scheme Used.

The *PER* depends on the *SNR*, on the modulation and coding scheme, and on the characteristics of the channel matrices. All matrices have been normalized, assuming a fixed transmitting power as in Figure 4.38 using the *SNR* from Figure 4.35.
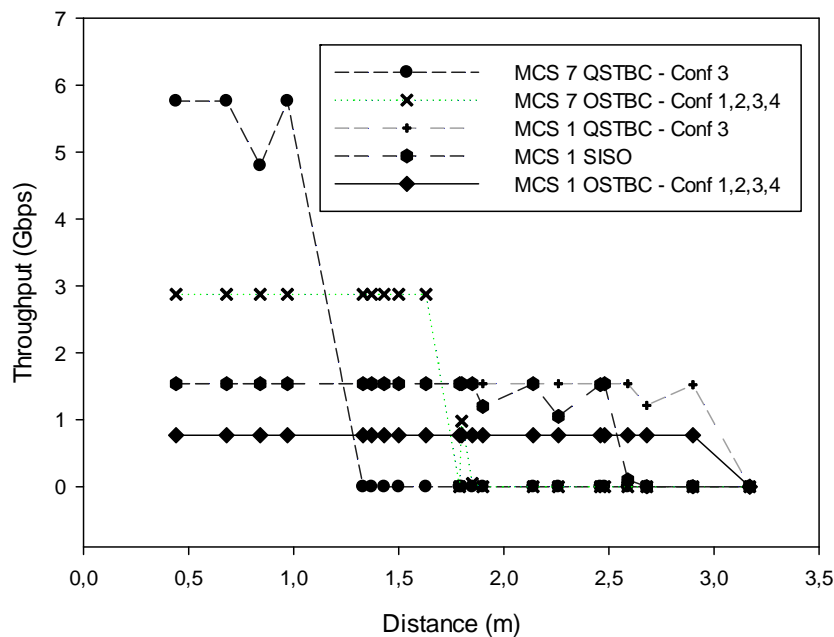
Figure 4.39: Best throughput for SISO and for MIMO (4,4) using either QSTBC or OSTBC architecture and both MCS 1 as MCS 7.

In Figure 4.39, the best throughputs for 4x4 *MIMO* have been plotted for both *QSTBC* as *OSTBC* architectures. We focus on *MCS* 1 and 7 to show the worst and best case in terms of achievable throughput. Furthermore, we have computed the best configurations in Table 4.15 for each case. The *SISO* case shows the throughput for *MCS* 1, since for *MCS* 7 it is zero for all distances because the SNR is too small to respect the constraint of $PER<10^{-3}$ with a 64 *QAM* modulation scheme.

As shown in Figure 4.36 the channels for Conf 1 and 4 are highly correlated; in [Sanchis, 2012] it is demonstrated that correlation influences the *QSTBC* case, while it is

not influential in the *OSTBC* case due to its orthogonality. So for *QSTBC*, the chosen configuration of the antennas is crucial, Conf 2 and 3 offering the best configurations.

Observing Figure 4.39 we can define for each curve the maximum distance (range) and minimum *SNR* to achieve the maximum throughput for each *MCS / MIMO* architecture. Table 4.15 summarizes the best configurations and all these parameters. Note that the relationship between distance and *SNR* is independent.

MCS / MIMO architecture	Best Configuration	Max. Distance (m)	Min. SNR (dB)
MCS 7 QSTBC	Conf 3	1	9.5
MCS 7 OSTBC	Conf 1,2,3,4	1.7	6
MCS 1 QSTBC	Conf 3	3	1
MCS 1 OSTBC	Conf 1,2,3,4	3	1
MCS 1 SISO	--	2.5	3.5

Table 4.15: Best Configuration, Max Distance and SNR for each Architecture.

We note that up to 1 m the *MCS* 7 *QSTBC* – Conf 3 case is the best, achieving a throughput of 5.77 Gbps, however the minimum *SNR* needed is 9.5 dB since *MCS* 7 uses a *64QAM* modulation and in addition the correlation increases at short distances. Between 1 and 1.7 m it is better to use *MCS* 7 *OSTBC*, with a throughput of 2.88 Gbps and an improved minimum *SNR* of about 3.5 dB because the correlation does not influence this case. Further, between 1.7 and 3 m the best case is *MCS* 1 *QSTBC* Conf 3, with the minimum *SNR* needed being 1 dB, because *MCS* 1 uses a *QPSK* modulation. The throughput obtained with *OSTBC* architecture is reduced by a factor of 2 compared to the *QSTBC* architecture, because the coding scheme used in *OSTBC* offers a rate of 1/2.

Lastly, in Figure 4.39 we see that the *MIMO* architecture gives better results compared to *SISO*, with the best schemes being *MCS7 QSTBC* and *MCS1 QSTBC* for short and long distances respectively. In the case of *MCS7 QSTBC*, the throughput is increased by a factor of 3.7 compared to the *SISO* case, while *MCS1 QSTBC* presents the same throughput as *SISO* but extends nearly 1 m further.

4.5.5 Conclusion

In this Section, the performance of *IEEE 802.15.3c MIMO-OFDM* systems for 4 configurations of antennas has been experimentally studied. The *correlation* is highly

influenced by the antennas configuration, since the arrangement of the antenna has a large impact on the performance, especially over short distances. Also *MIMO* seems a reasonable solution for both increasing the throughput and the communication distance, increasing the data bit rate by a factor of 3.7 with a 4x4 *QSTBC-MIMO* system, and also increasing the maximum achievable distance by 1 meter.

4.6 Conclusions

In this chapter, an extensive multidimensional analysis of experimental data and ray tracing simulations including single-order *diffuse scattering* in the *mm-W* frequency band was presented.

First, the *diffuse scattering* model was introduced in the *3D ray tracing tool*; this model takes into account the scattering coefficient of each material found in the environment, contrary to what can be found in the literature, where a global diffuse scattering coefficient is suggested for all environments. The diffuse scattering parameters for three materials usually found in indoor environments, i.e. plasterboard, glass and chipboard, were assessed. This enhanced ray tracing tool was subsequently used to compared simulation and experimental channel characterization in *mm-W*.

An analysis of *LoS* experimental data and the ray tracing simulations band for 20 transmitting positions in an 80 m^3 office showed that the results supported the idea that *diffuse scattering*, which accounts for 10% of the total energy, must be taken into account in simulations to faithfully reconstruct channel transfer functions. The *RiMAX* algorithm was used to extract the *MPC* parameters from both measured and simulated data set. From this analysis, a good agreement is reached between the time-delays and power angular spreads computed from the *RT* and measured channels. Those values are also found to be similar to other results published in the scientific literature.

Next, clustering methods such as visual inspection, K-means algorithms with several initializations, and grouping *MPCs* under a threshold have been presented using the previous extracted *MPC* parameters. A new method for automated identification of clusters for indoor *mm-W* channel was proposed. Our novel algorithm shows good agreement with results deduced from visual inspection.

In the second section, the indoor propagation phenomena for two different frequency bandwidths 2–10 (*cm-W*) and 57–66 GHz (*mm-W*) were analyzed. Using similar conditions and equipment, we measured the radio channel using omnidirectional antennas in an indoor environment for *LoS* and for *OLoS* using cardboard boxes and metal obstacles. The relative importance of the different propagation mechanisms varied from one band to the other. For example, *LoS* was much more important in *mm-W*, whereas multipath components are more significant in *cm-W*. This led to smaller *RMS DS* values, higher *K factors*, and higher de-correlation electrical distances in the *mm-W* frequency band. Also, some materials, such as cardboard, behaved differently in the two frequency bands.

Finally, the last part of this chapter dealt with the study of the performance of IEEE *802.15.3c MIMO-OFDM* systems for 4 configurations of antennas. The *Tx* antenna correlation was highly influenced by the antenna arrangement inside the array and its orientation referring to the *Rx* array, and therefore had a large impact on the performance, especially for short distances. Also *MIMO* seemed a reasonable solution for both, increasing the throughput and the communication distance, increasing the data bit rate by a factor of 3.7 with a 4x4 *QSTBC-MIMO* system, and also increasing the maximum achievable distance by 1 meter.

Chapter 5

Conclusions and Perspectives

The use of the license-free 60-GHz frequency band will allow multi-Gb/s data transmission over short distances. The design of these future wireless communication systems strongly depends on the propagation channel. The propagation channel can be modeled theoretically or experimentally. In contrast with theoretical characterization, experimental characterization provides a precise knowledge of the real scenario under analysis. However, experimental characterization requires not only undertaking measurements in the desired environment, but also developing adequate channel sounders.

The work presented in this thesis is aimed at theoretically and experimentally characterizing and modeling the propagation channel with large bandwidth at the millimeter band by means of the analysis of measurements in different scenarios as well as the development of a channel sounder. Apart from that, ray tracing is also used to predict propagation at such frequencies. Moreover, the formulation for multiple diffraction in the millimeter band has been studied and validated by measurements.

The main contributions of this thesis are presented in Section 5.1, while future research work is proposed in section 5.2.

5.1 Conclusions

As mentioned before, this thesis is focused in the theoretical and experimental characterization and modeling of the radio channel for 60 GHz systems and for large bandwidth channels.

Chapter 2 addressed the issue of propagation in the *mm-W* frequency band. In this state-of-the-art, the main aspects which characterize the 60-GHz band and previous works related with this band were highlighted. This chapter thus introduces the starting research point of this thesis.

Chapter 3 dealt with the validations of several *UTD-PO* solutions for the analysis of radiowave multiple diffraction through measurements performed at 60 GHz. Firstly, for the series of rectangular blocks as obstacles, a solid agreement was found between predicted data by the hybrid *UTD-PO* formulation and measured attenuation values at 62 GHz. Consequently, since the series of rectangular blocks can be assumed as scaled-models of an urban environment, the proposed *UTD-PO* formulation could be applied in the analysis of urban radiowave propagation. Secondly, multiple-cylinder diffraction was analyzed by performing another campaign of measurements at 60 GHz. A *UTD-PO* solution for this analysis was validated with these measurements. A parametric study was carried out both theoretically and experimentally in which the influence of: the number of cylinders, the radius of curvature, the distance from the transmitter to the array of rounded surfaces, and the polarization were analyzed. A small error ranging from 0.12 dB to 0.71 dB was found between the predicted and measured results. Thirdly, a comparison of cylindrical against rectangular obstacles in radiowave multiple diffraction evaluation was studied. A firm agreement between the predicted results by the *UTD-PO* solution and measured results was found. The rectangular modeling showed higher attenuation than the cylindrical obstacle representation for all the cases evaluated and a constant difference with H – of up to 1.82 dB – arose when comparing the two types of models (for a given number of diffracting elements n). Thus, the choice of appropriate obstacle modeling can be significant for obtaining realistic multiple diffraction loss predictions in the *mm-W*

band. Finally, a new method based on a hybrid *UTD-PO* formulation for the evaluation of the propagation loss due to the diffraction that takes place at the top of a rectangular obstacle which was illuminated from a low source was presented. The comparison with measurements at 60 GHz and a method based on the evaluation of a *Fresnel* surface integral showed a solid agreement.

In Chapter 4, results from an extensive multidimensional analysis of experimental data from three measurement campaigns at the *mm-W frequency band* were reported. These data have also been compared to deterministic models, such as *ray tracing*, including the experimental characterization of *diffuse scatter* in *mm-W*.

First of all, a first measurement campaign was made in order to quantify the diffuse parameters for three materials usually found in indoor environments, i.e. plasterboard, glass and chipboard. It was shown that introducing the contribution of *diffuse scattering* improves the accuracy of the *RT tool* unlike what it can be found in the literature where an average diffuse scattering parameter is proposed for a given environment. The characterization of diffuse parameters can be considering as a pioneering work.

The analysis of *LoS* experimental data shows that *DMC* represent 10% of the total energy. *Diffuse scatter* must be introduced in the *RT tool* to faithfully reproduce the propagation channel. By introducing diffuse components into the *RT tool*, it was demonstrated that second-order scattering might not be necessary to assess the propagation parameters of the *mm-W* channels.

The second measurement campaign was performed in an 80 m^3 office with 20 transmitting positions. The *RiMAX* algorithm was used to extract the *MPC* parameters from both measured and simulated data set. From this analysis, a good agreement was reached between the time-delays and power angular spreads computed from the *RT* and measured channels. Those values were also found to be similar to other results published in the scientific literature. In summary, results show that even a raw description of the environment can be used to predict *mm-W* propagation with ray tracing.

Next, clustering methods such as *Visual Inspection*, *K-means* algorithms with several initializations and grouping *MPCs* according to a threshold were compared. A new method for automated identification of clusters for indoor *mm-W* channel was proposed.

Our novel algorithm exhibits similar clusters than the *Visual Inspection* which is considered as the reference.

The third measurement campaign was carrying out in order to compare the indoor propagation phenomena at two different frequency bandwidths: 2–10 (*cm-W*) and 57–66 GHz (*mm-W*). Using similar conditions and equipment, the radio channel was measured using omnidirectional antennas in an indoor environment for *LoS* and for *OLoS* using cardboard boxes and metal obstacles. The importance of different propagation mechanisms varied from one band to the other. For example, *LoS* was much more important in *mm-W*, whereas multipath components were more significant in *cm-W*. This led to smaller *RMS DS* values, higher *K-factors* and higher *de-correlation* electrical distances in the *mm-W frequency band*. Also, some materials, such as cardboard, behaved differently in the two frequency bands.

Finally, the performance of *IEEE 802.15.3c MIMO-OFDM* systems was studied for four configurations of antennas using experimental data from the second measurement campaign. The correlation was highly influenced by the configuration (orientation of the antennas), and those which did not depend on the orientation seem to be the most appropriate solutions (symmetry configurations such as squares); therefore the design of the antenna configuration had a large impact on the performance, especially over short distances. Also *MIMO* technique seems to be a reasonable solution for both increasing the throughput and the communication distance, increasing the data rate by a factor of 3.7 with a *4x4 QSTBC-MIMO* system, and also increasing the maximum achievable distance by 1 meter.

5.2 Perspectives

As in any research field, the realization of this thesis has led to new ideas which may contribute to the improvement and future extension of this work. Not limited to these lines, some of them are:

- Study of other configurations for multiple diffraction, not being limited to one type of obstacle (knife edges, cylinders, etc.).
- Comparison of *spherical* against *plane-wave* incidence assumption in the study of radiowave multiple diffraction in *mm-W* frequencies.

- Development of a real-time channel sounder in *mm-W* to analyze time-varying channels.
- Extension to other scenarios.
- Completion of the diffuse scatter characterization for other materials.
- Study the radio channel in the *mm-W frequency band* for different polarization of the antennas.
- Perform the analysis of the *XPD* and the analysis of the relation between the *XPD* and other parameters that characterizes the propagation channel.
- The development of an "easy-to-use" channel model based on trade off between accuracy and simplicity

Furthermore, the EU Horizon 2020 has as one of its priorities the extension of wireless technologies beyond 60 GHz. The use of frequency bands beyond 60 GHz is not restricted to communications, but it also find uses in radar, remote sensing and imaging with applications in security, non-destructive testing, earth observation among others.

Research groups (IEMN/TELICE and SICOMO) involved in the supervision of the thesis will continue the collaboration in a new project where new frequency bands will be considered, such as 94 GHz and 300 GHz. All results outlined in this thesis will have great value for this new project.

Appendices

Appendix A

Ray Tracing and main

propagation mechanism

The ray tracing is a deterministic model which is used for the prediction of the radio channel propagation. It is based on *Geometric Optic (GO)* and the *Uniform theory of diffraction (UTD)*.

The most of the energy is concentrated in the first *Fresnel zone* [Bello, 1963]. When the frequency rises, this zone tends to narrow and it is able to simulate as a ray [Deschamps, 1972]. Thus, the propagation of electromagnetic waves can be showed as the way propagation of an optic ray, which simplifies the analysis enormously.

The main propagation mechanisms are reflection, diffraction or scattering [Rappaport, 1996]. The reflection occurs when an electromagnetic wave reaches an object with dimensions are higher than wavelength. *GO* considers the reflection and uses the

Snell law [Balanis, 1989]. Diffraction is caused by the propagation of secondary wavelets into a shadowed region. This phenomenon can be explained by *Huygen's* principle and the *UTD* solves this problem. Scattering is described as the effect on the wave of objects with similar dimensions to wavelength or when the number of objects per unit of volume is high.

There are two ways of ray tracing. The first is *Ray Launching*, consisting on throwing rays from the position of the transmitter with an angular constant separation and its tracking [Zhang, 1998]. The second is called as *Ray Tracing*. It is based on generating images from the possible reflections in the environment [Mariage, 1994].

Thus, in this Appendix, the main features of the ray tracing and the main propagation mechanism are highlight to put in context to the reader.

A.1 Geometric Optic

The *Geometric Optic* is an approximated method applicable to high frequencies. The wavefronts are described as rays which represent a spherical wave [Balanis, 1989]. As a result, the problem is analyzed as a problem of ray theory instead of taking into account the wavy behavior of the electromagnetic fields. Taking into consideration the *GO*, the contributions of the fields of an incident, reflected or refracted waves can be studied in an easier way because it uses the *Snell law*.

A.1.1 Direct Ray

The waves are propagated in environments with a refraction index n. These environments are considered homogenous (n constant inside the same environment). This means that the way of a ray between two points will be a straight line. Therefore, the wavefront which represents the ray does not suffer from any additional propagation mechanism. The wavefront only suffers from the attenuation with the own distance of a spherical wave. This situation is called *Line of Sight* (*LoS*).

The electromagnetic field is defined by the direct ray is:

$$E_{DIR}(r) = E_0 \frac{e^{-jkr}}{r} \qquad\qquad (A.1)$$

where E_0 is a factor which depends on the transmitter, r is the distance between the transmitter and the receptor, and k is the number of wave $\left(k = \dfrac{2\pi}{\lambda} \right)$. The expression corresponds to the own field of the spherical wave, which is attenuated inversely with the distance between the transmitter and receiver. The exponential term shows the phase of the wave, which depends on the distance travelled.

A.1.2 Reflection

The reflection is produced when a wave reaches over a surface which separates two means with different electromagnetic properties with different refraction indices (n_1 and n_2). Following the *Snell law*, part of the reached wave is reflected and part is transmitted towards the second mean. *GO* allows the compute of the fields (rays) which are reflected in a specular way in a flat surface of any geometry. A reflection coefficient R is defined. R is the relation between the reached wave and the reflected wave. It depends on the electrical characteristics of the reflection surface (permittivity and conductivity) of the polarization of the reached wave, of reached angle and frequency of wave.

The electromagnetic properties of any surface are characterized by the definition of a dielectric complex relative constant [Balanis, 1989]:

$$\varepsilon_r = \frac{\varepsilon}{\varepsilon_0} = \varepsilon_r' - j\frac{\sigma}{\omega\varepsilon_0} = \varepsilon_r'(1 - j\tan\delta_e) \approx \varepsilon_r' - j60\lambda\sigma \qquad (A.2)$$

where ε_r' is the relative permittivity of the mean over the wave reaches, j is $\sqrt{-1}$, σ is the conductivity in Siemens/m, ω is the angular frequency, ε_0 is the permittivity in the vacuum, δ is the loss tangent and λ is the wavelength in which it is propagated the wave in meters.

A.1.2.1 Soft Polarization

This polarization is called *TE* or *horizontal polarization* also. It is produced when the vector of the electric field of the incident wave is perpendicular to the incident plane.

This plane is defined as the plane which contains the incident and reflected rays. The magnetic field of the wave is contented in the said plane due to the far field condition, $H \perp E$.
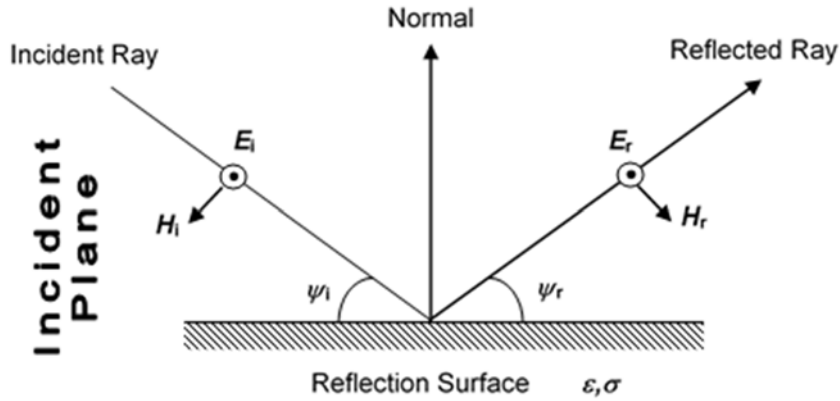
Figure A.1: Soft Incident. View from incident plane.

The incident angle ψ_i agrees with the reflected angle ψ_r according to *Snell's law* $(\psi_i = \psi_r = \psi)$. The reflection coefficient when the incidence is soft is:

$$R_\perp(\psi) = \frac{sen(\psi) - \sqrt{\varepsilon_r - \cos^2 \psi}}{sen(\psi) + \sqrt{\varepsilon_r - \cos^2 \psi}} \qquad (A.3)$$

A.1.2.2 Hard Polarization

This situation is when the electric field vector of the incident wave is in the incident plane. The magnetic field will be perpendicular to the electric field. It is known as *vertical polarization* or *TM*.
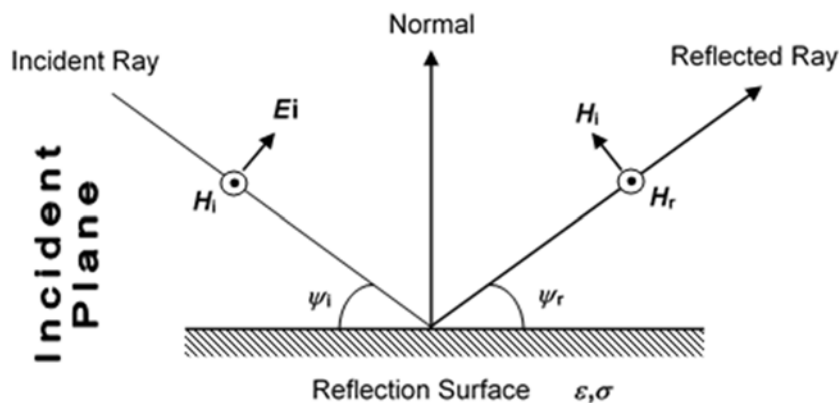
Figure A.2: Hard Incident. View from incident plane.

The reflection coefficient for the hard polarization is:

$$R_{\parallel}(\psi) = \frac{\varepsilon_r sen(\psi) - \sqrt{\varepsilon_r - \cos^2 \psi}}{\varepsilon_r sen(\psi) + \sqrt{\varepsilon_r - \cos^2 \psi}} \tag{A.4}$$

A.1.3 Electric Field Defined by a Reflected Ray

In the case of a mixed polarization, the incident field will be split into soft and hard components.

The electromagnetic field associated to the contribution of the reflected wave is:

$$E_R(r) = E_0 R \frac{e^{-jkr}}{r} \tag{A.5}$$

where E_0 is a factor which depends on the transmitter, k is the wave number, r is the total distance travelled by the reflected ray and R is the coefficient of reflection, (A.3) or (A.4) depending on the polarization. In the case of multiple reflections for the same wave, the value R would be the accumulated product of every value R_i of every reflection i:

$$R = \prod_i R_i \tag{A.6}$$

A.2 Uniform Theory of Diffraction

The diffraction of a wavefront occurs when it reaches a sharp obstacle, such as a corner of an urban environment. The corner becomes in a secondary focal emitter (*Huygen's principle*), creating a new wave front [Balanis, 1989].

The optic geometric is not used for computing the produced fields by the diffraction. Due to this fields have a very low amplitude, they do not influence on *LoS*, or in zones which the reflected fields are high. However, they are important in the shadow zones.

For high frequencies, it is used a model for diffraction where it depends only on the geometry of the object and the amplitude, phase, polarization and frequency of the

incident wave on the point of diffraction. It is developed the *Uniform Theory of Diffraction (UTD)* [Balanis, 1989] which comes from *Geometrical Theory of Diffraction (GTD)* [Keller, 1962].

GTD is an extension of *GO* for predicting the field in a shadow region caused by an edge. However, *GTD* can not apply to the neighborhood of the transition regions (see 2.4.2.1). *UTD* overcomes these singularities for the total field with transition borders [Balanis, 1989].

A.2.1 Transition Borders

There are three regions with borders which depend on the position of the source (ρ', ϕ'), of the observation point (ρ, ϕ), and the position of the edge (Figure A.3).
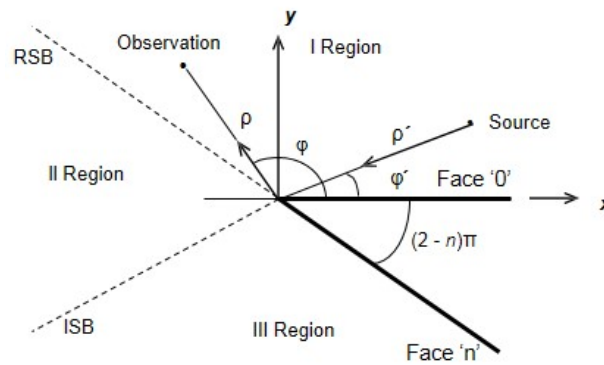
Figure A.3: Transition regions and coordinate system for edge.

Reflected Shadow Boundary (*RSB*) is the border between the region I and II and *Incident shadow boundary* (*ISB*) is the border between the regions II and III. The considered contributions for computing the total field in every region are:

I Region	II Region	III Region
$0 < \varphi < \pi - \varphi'$	$\pi - \varphi' < \varphi < \pi + \varphi'$	$\pi + \varphi' < \varphi < n\pi$
direct reflected diffracted	direct diffracted	diffracted

Table A.1: Border regions of the diffraction and associated contributions to everyone.

A.2.2 Diffracted Field

Two coordinate systems are defined (Figure A.4): (s', β', ϕ') in relation to the incident ray from the source in the diffraction point Q_D and (s, β, ϕ) regarding the diffracted ray from Q_D until the observation point. The diffracted field is showed as:

$$\bar{E}^d = \bar{E}^i(Q_D) \cdot \bar{D}(L; \phi, \phi'; \beta_0') A(s', s) e^{-jks} \tag{A.7}$$

$$A(s', s) \begin{cases} \dfrac{1}{\sqrt{s}} & \text{plane wave} \\[2ex] \dfrac{1}{\sqrt{ssen\beta_0}} & \text{cylindric wave} \\[2ex] \sqrt{\dfrac{s'}{s(s+s')}} & \text{spheric wave} \end{cases} \tag{A.8}$$
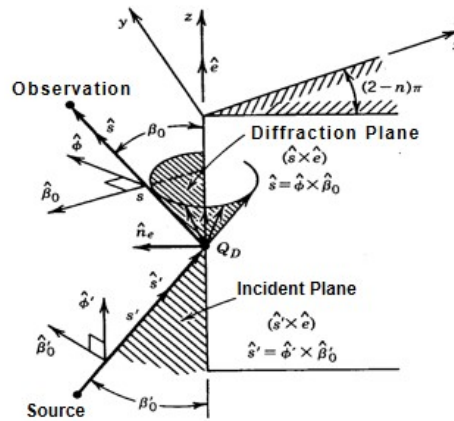
Figure A.4: Transition Oblique incident over an edge with conducted walls [Balanis, 1989].

where $\bar{E}^i(Q_D)$ is the incident field in Q_D, $\bar{D}(L; \phi, \phi'; \beta_0')$ is the diadict coefficient of diffraction and $A(s', s)$ is a term which takes into consideration the vary of the intensity of field along the diffracted ray. When a ray reaches over an edge, multiple rays are diffracted. Every ray has an associated field like (A.7).

A.2.3 The Diadict Coefficient of Diffraction

Following the geometry of the Figure A.4, β_0^i and ϕ' are two unit parallel vectors and perpendicular to the incident plane. $\hat{\beta}_0$ y $\hat{\phi}$ are two unit parallel vectors and perpendicular to the diffraction plane. Moreover, these vectors plus vectors $\hat{s}'$ and $\hat{s}$ follow the relation:

$$\hat{s}' = \hat{\varphi}' \times \hat{\beta}_0'$$
(A.9)

$$\hat{s} = \hat{\varphi} \times \hat{\beta}_0$$
(A.10)

The D coefficient is:

$$\bar{D} = -\hat{\beta}_0' \hat{\beta}_0 D_s - \hat{\varphi}' \hat{\varphi} D_h$$
(A.11)

Where D_s and D_h are the coefficients of diffraction for the case of *soft* polarization or *hard* polarization. If the fields are separated into parallel and perpendicular component:

$$\left.\begin{aligned}
\vec{E}^i &= E^i_{\beta_0} \hat{\beta}_0' + E^i_{\varphi'} \hat{\varphi}' \\
\vec{E}^d &= E^d_{\beta_0} \hat{\beta}_0 + E^d_{\varphi} \hat{\varphi}
\end{aligned}\right\}$$
(A.12)

In matricial form:

$$\begin{bmatrix} E^d_{\beta_0}(s) \\ E^d_{\varphi}(s) \end{bmatrix} = -\begin{bmatrix} D_s & 0 \\ 0 & D_h \end{bmatrix}\begin{bmatrix} E^i_{\beta_0}(Q_D) \\ E^i_{\varphi'}(Q_D) \end{bmatrix} A(s',s)\exp(-jks)$$
(A.13)

The coefficients of *Diffraction* are defined as:

$$\left.\begin{aligned}
D_s &= D^i - D^r \\
D_h &= D^i + D^r
\end{aligned}\right\}$$
(A.14)

where D^i and D^r are obtained by imposing the continuity conditions for the total field in the *ISB* and the *RSB* respectively. The expressions of these coefficients are:

$$D^i = \frac{-\exp(-j\pi/4)}{2n\sqrt{2\pi k}\,sen\beta_0}\left\{\cot\left[\frac{\pi+(\varphi-\varphi')}{2n}\right]F\left[kLa^+(\varphi-\varphi')\right]+\right.$$
$$\left.\cot\left[\frac{\pi-(\varphi-\varphi')}{2n}\right]F\left[kLa^-(\varphi-\varphi')\right]\right\} \qquad (A.15)$$

$$D^r = \frac{-\exp(-j\pi/4)}{2n\sqrt{2\pi k}\,sen\beta_0}\left\{\cot\left[\frac{\pi+(\varphi+\varphi')}{2n}\right]F\left[kLa^+(\varphi+\varphi')\right]+\right.$$
$$\left.\cot\left[\frac{\pi-(\varphi+\varphi')}{2n}\right]F\left[kLa^-(\varphi+\varphi')\right]\right\} \qquad (A.16)$$

L is a parameter of distance which can be find satisfying the condition of the total field should be continuous along the *ISB* and *RSB*. For the case of the incident plain, cylindrical or spherical wave in an edge of plain walls:

$$L = \begin{cases} s\,sen^2\beta_0 & plane\ wave \\ \dfrac{s'\,s\,sen\beta_0}{s'+s} & cylindrical\ wave \\ \dfrac{s'\,s\,sen^2\beta_0}{s'+s} & spherical\ wave \end{cases} \qquad (A.17)$$

The function *F(x)* is the *Fresnel Transition Function* and it is defined by terms of a *Fresnel integral*:

$$F(x) = 2j\sqrt{x}\,\exp(jx)\int_{\sqrt{x}}^{\infty}\exp(-j\tau^2)\,d\tau \qquad (A.18)$$

The function *F(x)* can be computed by *seno* and *coseno* integrals:

$$S(x) = \int_0^x sen\left(\frac{\pi}{2}\tau^2\right)d\tau \qquad (A.19)$$

$$C(x) = \int_0^x \cos\left(\frac{\pi}{2}\tau^2\right)d\tau \qquad (A.20)$$

As follow:

$$F(x) = j\sqrt{2\pi}\sqrt{x}\exp(jx)\left\{\left[\frac{1}{2} - C\left(\sqrt{\frac{2}{\pi}}\sqrt{x}\right)\right] - j\left[\frac{1}{2} - S\left(\sqrt{\frac{2}{\pi}}\sqrt{x}\right)\right]\right\} \tag{A.21}$$

In the expressions, the argument of $F(x)$ contains the function $a^{\pm}(\chi)$ which measures the angular separation between the observation point and the *ISB* or the *RSB*. Its expression is:

$$a^{\pm}(\chi) = 2\cos^2\left(\frac{2n\pi N^{\pm} - \chi}{2}\right), \quad \chi = \varphi \pm \varphi' \tag{A.22}$$

being N^+ and N^- the entered numbers which better satisfied this:

$$2\pi n N^+ - \chi = \pi \tag{A.23}$$

$$2\pi n N^- - \chi = -\pi \tag{A.24}$$

A.2.4 Diffraction Coefficients GTD

From the diffraction coefficients defined by *UTD* can be computing the diffraction coefficients defined by *GTD* taking into account that when the fields are evaluated in far enough points of the borders of transition *ISB* and *RSB*:

$$kLa^{\pm}(\varphi \pm \varphi') > 10 \tag{A.25}$$

Which implies $F(x) \approx 1$. With this condition and after some trigonometric transformations:

$$D^i = \frac{\exp(-j\pi/4)}{n\sqrt{2\pi k}\,sen\beta_0}\frac{sen\dfrac{\pi}{n}}{\cos\dfrac{\pi}{n} - \cos\dfrac{\varphi - \varphi'}{n}} \tag{A.26}$$

$$D^r = \frac{\exp(-j\pi/4)}{2\sqrt{2\pi k}\,sen\,\beta_0}\frac{sen\dfrac{\pi}{n}}{\cos\dfrac{\pi}{n} - \cos\dfrac{\phi + \phi'}{n}} \tag{A.27}$$

The *hard* or *soft* coefficients are calculated with (A.14).

A.2.5 Diffraction UTD in an Edge of Finite Conductivity Walls

If the diffraction phenomenon occurs in a not perfect conducted edge, the didactic coefficient of diffraction adopts a new form. Separating the didactic coefficient of diffraction into its soft and hard components from (A.14), (A.15) and (A.16). In the case of *soft* polarization, it is added the $R_0^{\perp}$ y $R_n^{\perp}$ and in the case of *hard* polarization $R_0^{//}$ y $R_n^{//}$. With this, a new diffraction coefficient is obtained taking into account the finite conductivity of the walls [Luebbers, 1984b]:

$$
\begin{aligned}
D_s = \frac{-\exp(-j\,\pi/4)}{2n\sqrt{2\pi k}\,sen\beta_0} \Bigg\{ \\
\cot\left[\frac{\pi+(\varphi-\varphi')}{2n}\right] F\left[kLa^+\left(\varphi-\varphi'\right)\right]+ \\
\cot\left[\frac{\pi-(\varphi-\varphi')}{2n}\right] F\left[kLa^-\left(\varphi-\varphi'\right)\right]+ \\
R_0^{\perp}\cot\left[\frac{\pi-(\varphi+\varphi')}{2n}\right] F\left[kLa^-\left(\varphi+\varphi'\right)\right]+ \\
R_n^{\perp}\cot\left[\frac{\pi+(\varphi+\varphi')}{2n}\right] F\left[kLa^+\left(\varphi+\varphi'\right)\right] \Bigg\}
\end{aligned}
\qquad (A.28)
$$

With *soft* incident and if the incident is *hard*:

$$
\begin{aligned}
D_h = \frac{-\exp\left(-j\,\pi/4\right)}{2n\sqrt{2\pi k}\,sen\beta_0} \Bigg\{ \\
\cot\left[\frac{\pi+(\varphi-\varphi')}{2n}\right] F\left[kLa^+\left(\varphi-\varphi'\right)\right]+ \\
\cot\left[\frac{\pi-(\varphi-\varphi')}{2n}\right] F\left[kLa^-\left(\varphi-\varphi'\right)\right]+ \\
R_0^{\|}\cot\left[\frac{\pi-(\varphi+\varphi')}{2n}\right] F\left[kLa^-\left(\varphi+\varphi'\right)\right]+ \\
R_n^{\|}\cot\left[\frac{\pi+(\varphi+\varphi')}{2n}\right] F\left[kLa^+\left(\varphi+\varphi'\right)\right] \Bigg\}
\end{aligned}
\qquad (A.29)
$$

If the incident has a mixed polarization, the incident field is separated into its *soft* and *hard* components, for then used D_s or D_H.

The parameters $R_0^{\perp,//}$ and $R_n^{\perp,//}$ which appears in (A.28) and in (A.29) represent the reflection coefficients of *Fresnel* for perpendicular and parallel polarization in the face '*0*' of the edge (Fig. A.3), with incident angle ϕ', and in the face '*n*' of the edge, with reflection angle *(nπ-ϕ)*.

The grazing incident occurs when incident wave in an edge has an incident angle ϕ'=0 or ϕ'= nπ. In this case, both for perfect conductivity walls and finite conductivity, the general diffraction coefficients *UTD* given by (A.28) and (A.29) are suitable. This field is corrected by a factor of $\dfrac{1}{2}$ [Kouyoumjian, 1974].

A.2.6 Electric Field Defined by a Diffracted Ray

In (A.30) it is showed the field defined by a diffracted ray which reaches the receiver and it does not suffer from any propagation mechanism.

$$E_{\mathrm{D}} = \frac{E_o}{s'} DA(s,s') \cdot e^{-jk(s+s')} \tag{A.30}$$

This expression is the same that (A.7). In the Figure A.4, *s'* is the distance travelled before reaching the diffraction point. In the same way, *s* is the distance travelled by the ray after the diffraction point. $D=D(n, \beta_0', \phi', \phi, L)$ is the diffraction coefficient. This coefficient can be defined by (A.28) in the case of *soft* polarization, or by A.29 for *hard* polarization. When incident ray represents a spherical wave, the distance value *L* is:

$$L = \frac{ss'}{s+s'} sen^2 \beta_0 \tag{A.31}$$

which is used for computing *D*.

For spherical waves, from (A.8), the value for *A*(*s*, *s'*) is:

$$A(s,s') = \sqrt{\frac{s'}{s(\,s'+s\,)}} \tag{A.32}$$

This factor represents the attenuation for the diffraction field with the distance. It is known as *Spreading Factor*.

A.3 Short About the Different Contributions of the Tracing

If the ray represents the contribution of the direct wave, its field is:

$$E_{DIR}(r) = E_o \frac{e^{-jkr}}{r} \tag{A.33}$$

When the ray is reflected one or several times in some surface, the field of the received wave is:

$$E_R(r) = E_o R \frac{e^{-jkr}}{r} \tag{A.34}$$

R is the total reflection coefficient. It is the product of the different coefficients regarding every individual reflection suffered by the ray. In the case of the presence of several diffraction phenomena in an edge and for the case of spherical waves, the field is:

$$E_D = \frac{E_o}{s'} D \sqrt{\frac{s'}{s(s'+s)}} \cdot e^{-jk(s+s')} \tag{A.35}$$

s' is the distance travelled by the ray before reaching the diffraction point, *s* is the distance travelled after the point of diffraction; and $D=D(n, \beta_o', \phi', \phi, L)$ is the coefficient of diffraction. This coefficient can be described by (A.28) if the polarization is *soft*, or by (A.29) if the polarization is *hard*.

In the case of simple diffraction combined with multiple reflections, the expression of the field of the ray is:

$$E_{R-D} = \frac{E_o}{s'} DR \sqrt{\frac{s'}{s(s'+s)}} e^{-jk(s+s')} \tag{A.36}$$

where *D* is the diffraction coefficient calculated by the considered corner and *R* is the coefficient of the total reflection (product of the corresponding to every individual reflection).

Appendix B

Frequency-Domain Channel

Sounder

In order to acquire a detailed knowledge of the propagation channel for the development of high data rate systems, measurements become an essential step and, therefore, channel sounders need to be designed in the 60 GHz frequency range to define the propagation characteristics. In this sense, examples of such sounders for the millimeter-wave band have been proposed for wideband indoor propagation [Guillouard, 1999] [Loyez, 2001][Zwick, 2005][Kivinen, 2007][Peter, 2007][Geng, 2009][Garcia, 2010] and MIMO configurations [Ranvier, 2005].

Channel sounding techniques can be classified according to the excitation signals that determine the characterization domain (time or frequency) and the multiplexing technique used to identify each antenna of the system [Gutierrez, 2011]. On the one hand, within the excitation signals, we can find continuous-wave signals, pseudorandom noise

[Ciccognani, 2005] signals, and multifrequency signals [Gutierrez, 2011]. On the other hand, three main multiplexing techniques exist: *time-division multiplexing (TDM)*, *frequency-division multiplexing (FDM)*, and code-division.

In the thesis, a frequency domain approach has been used to acquire a detailed knowledge of the propagation channel features for the development of high data rate systems. Virtual arrays are used to sample spatial characteristics of the electric field.

This Appendix deals with the description about the employed channel sounder in the thesis. Firstly, a system description is presented. Next, the hardware components are detailed and finally, the software program developed in *Matlab* is described.

B.1 System Description

The channel sounder used in this thesis is based on a Rhode ZVA67 *vector network analyser* (*VNA*), acquired by the Universidad Politécnica de Cartagena at the beginning of the present thesis. Two ports of the *VNA* are used to measure the transmission S_{21} parameter, which makes possible to measure in frequency domain the complex transfer function of a wireless system.

In Figure B.1 a general scheme is shown. It is observed that the receiving antenna (*Rx*) is directly connected to one port of the *VNA* through a coaxial cable while the signal of the transmitter port of the *VNA* is first amplified and then connected to the transmitting antenna (*Tx*) through a coaxial cable. The number of amplifiers used in each measurement depends on the characteristics of the scenario due to the required dynamic range and distance under analysis. The coaxial cables are suitable for working in millimetre wave frequency bands, even if the attenuation is not negligible, as it will be seen later.

For every measurement campaign, a *Matlab* software program was developed in order to control all the measurement process by a laptop which is connected to the *VNA* by a *LAN* (*Local Area Network*).
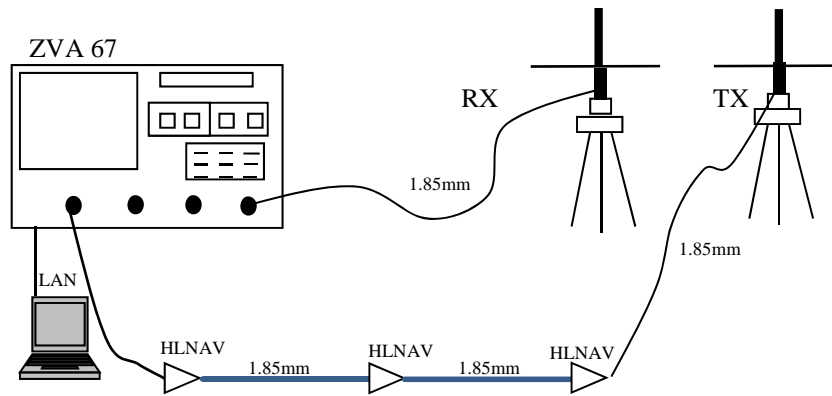
Figure B.1: Scheme of the frequency-domain channel sounder.

In the following sections, both the hardware and the software program used in the channel sounder are explained.

B.2 Hardware

This section is focused on the devices that compose the frequency-domain channel sounder: the *VNA*, the amplifiers, the antennas, controllers and some other elements.

B.2.1 Vector Network Analyzer

The used *VNA* is the Rhode ZVA67 with 4 ports. From a design point of view, the Rhode ZVA67 *VNA* has a dynamic range of 110 dB at 60 GHz using an intermediate frequency (*IF*) of 10 Hz between the two 1.85 mm female ports (this dynamic range can be increased to 120 dB for an *IF* of 1 Hz). In general, the use of a *VNA* is quite adequate, although it is restricted to static channels since the measurement time is high, and the channel must be static during the measurement.

Figure B.2: Rhode ZVA67 *VNA*.

B.2.2 Power Amplifiers

Amplifiers are used to compensate the cable attenuation, i.e. improve the dynamic range. The used amplifiers are *HXI HLNA-465* with 25 dB gain. Table B.1 summarizes its characteristics, and some photos are depicted in Figure B.3.

Model	HLNAVC-465
Description	57-66 GHz Low Noise Amplifier
Frequency range	57.0 a 66.0 GHz
Noise figure	5.5 dB typical (no measure)
P1dB	+12dBm typical
Gain	24dB typical
Maximum input power	-5dBm
BIAS	+6.5 VDC @ 300 mA Typical
RF INPUT/OUTPUT	1.85 mm female
BIAS CONNECTORS	Filtered Feedthroughs
Outline	HXI Darwing # 5473
Manufacturer	HXI

Table B.1: Specifications of the *HLNA-465* (1.85mm) Amplifiers.

Figure B.3: *HLNA-465* Amplifiers.

B.2.3 Power Sources

The power sources are essential for supplying the power to amplifiers. The used model is *EP613-A*, and it is shown in Figure B.4.

Figure B.4: Power Source EP613-A.

B.2.4 Antennas

Several antennas have been used for the different measurement campaigns, and are the following:

1) Millimetre wave omnidirectional antennas.

   Two antennas *Q-par QOM55-65 VRA* 55 to 65 GHz omni-directional V-type were used in some of the experiments. Figure B.5 depicts a photo of the antenna.

   The gain of the antennas varies from 3.8 to 5.3 dBi within the 55 to 65 GHz frequency band, and the typical 3 dB elevation beamwidth ranges from 23° to 28°, while being omnidirectional in the horizontal plane. The phase centre of these antennas is located at 16 mm above the bottom face of the antenna and has been used as the height reference.

   In Figure B.6 shows the manufactured data sheet for the antenna the gain in terms of frequency, 3dB beamwitdh, the return losses and three elevation patters for three frequencies: 55 GHz, 60 GHz and 65 GHz.

Figure B.5: Omnidirectional antenna QOM55-65 VRA.

Figure B.6: Omnidirectional Antenna characteristics.
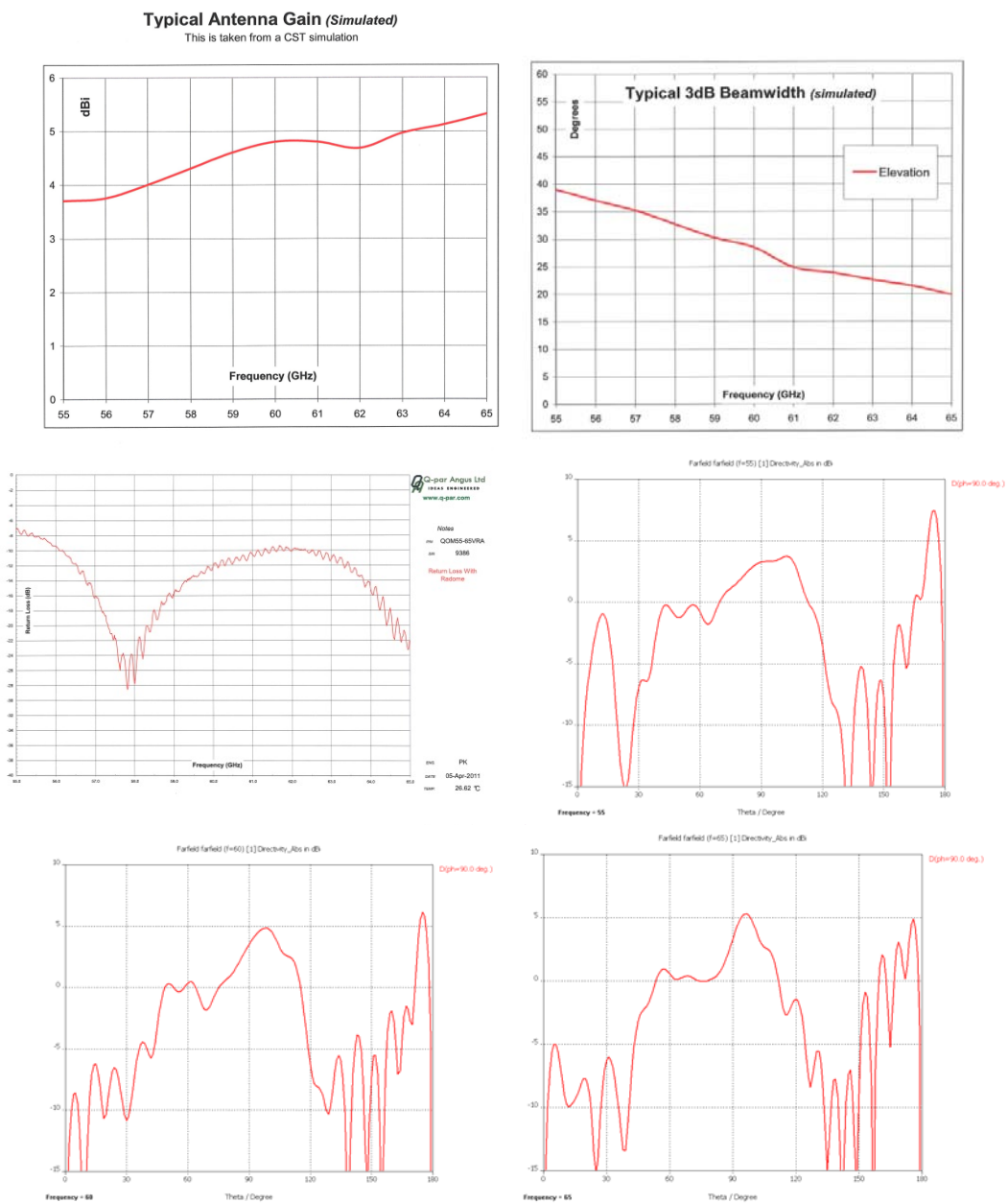
2) Millimetre wave horn antenna

The second antenna is a horn antenna *Q-par QSH25V20* (two antennas), being a millimetre horn V-type. The gain of the antenna ranges from 18 to 20.8 dBi within the 50 to 75 GHz frequency band and the typical 3 dB elevation beamwidth varies from 21° to 19° in the E-plane and from 19° to 18° in the H-plane. Figure B.7 shows a photo of the antenna.
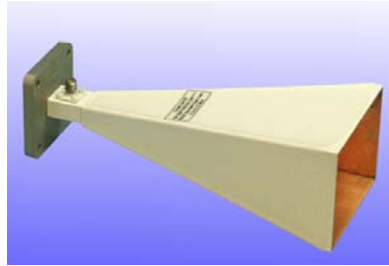
Figure B.7: Horn antenna.

In Figure B.8, manufacturer data sheets are shown. The antenna gain versus frequency, H-plane and E-plane 3-dB beamwidth and 10-dB beamwidth.
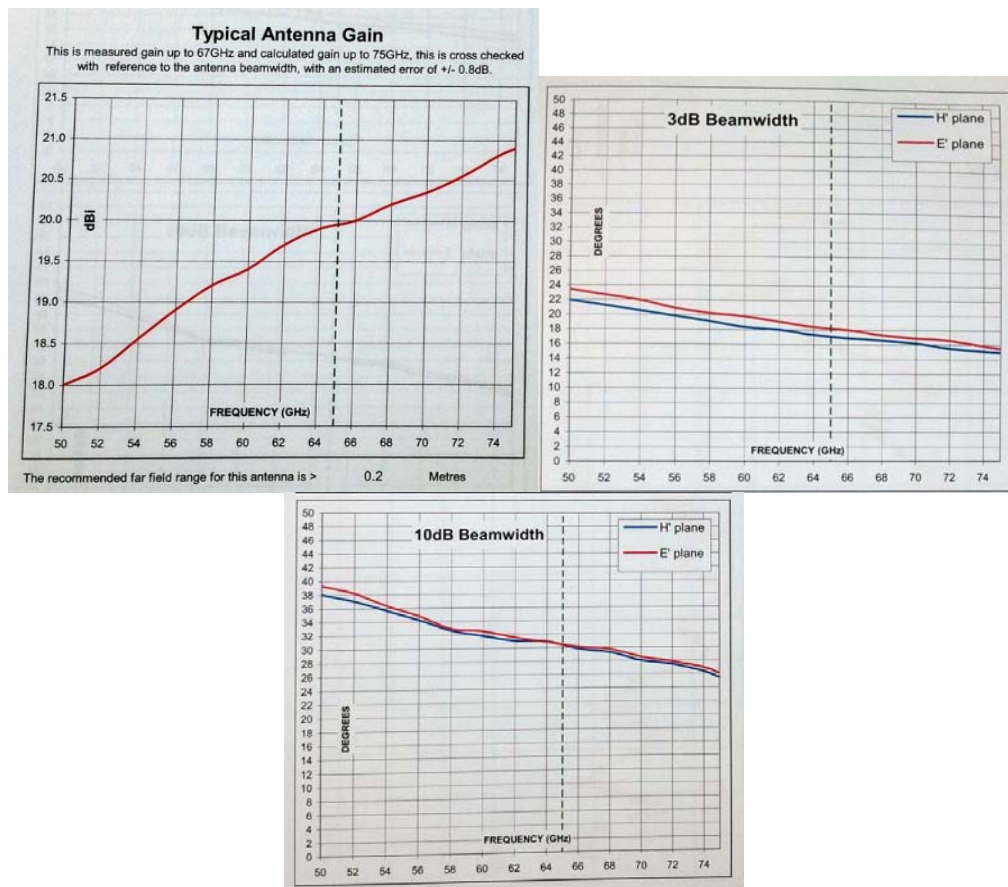
Figure B.8: Horn Antenna characteristics.

3) Millimetre wave Lens antenna

The third type of antenna is a lens antenna manufactured by *Q-PAR* (Ref. *H3445 25810-TA UG-385/U Comp*). It has the following characteristics:

- Frequency band: 51,5 GHz to 75 GHz
- VSWR: 1,5 max
- Lens Diameter: 100mm
- Nom mid-band gain: 34 dBi
- Nom 3 dB beamwidth E-plane: 3,5º
- Nom 3 dB beamwidth H-plane: 4º

A photo of the antenna can be seen in Figure B.9.

Figure B.9: Lens antenna H3445 25810-TA.

4) Centimetre wave omnidirectional antennas.

Finally, two omnidirectional *Electrometrics EM-6116* antennas have been used in one of the measurement campaigned explained in chapter 4. This antenna operates in the 2-10 GHz band and provides gain of 0.1, 3.4 and 3.7 dBi at 2, 6 and 10 GHz, respectively. Figure B.10 shows a picture of the antenna.

Figure B.10: Omnidirectional *Electrometrics EM-6116* antenna.

B.2.5 Coaxial Cables

Coaxial cables were used to connect different components of the set-up. The insertion losses of the coaxial cable are around 5 dB/m at 62 GHz and 6 dB/m at 66 GHz. In one of the measurements campaing, the *cm-W* channel was measured, being the insertion loss 2.13 dB/m at 10 GHz

In the laboratory, five cables with lengths of 0.5, 2, 3, 4 and 5 meters where used. In Figures B.11 and B.12, the datasheets of the 4 and 2 m cables are shown. In them, the four scattering parameters (S_{11}, S_{21} S_{12} and S_{22}) are plotted up to 60 GHz.

Figure B.11: Photo of the Coaxial cable.
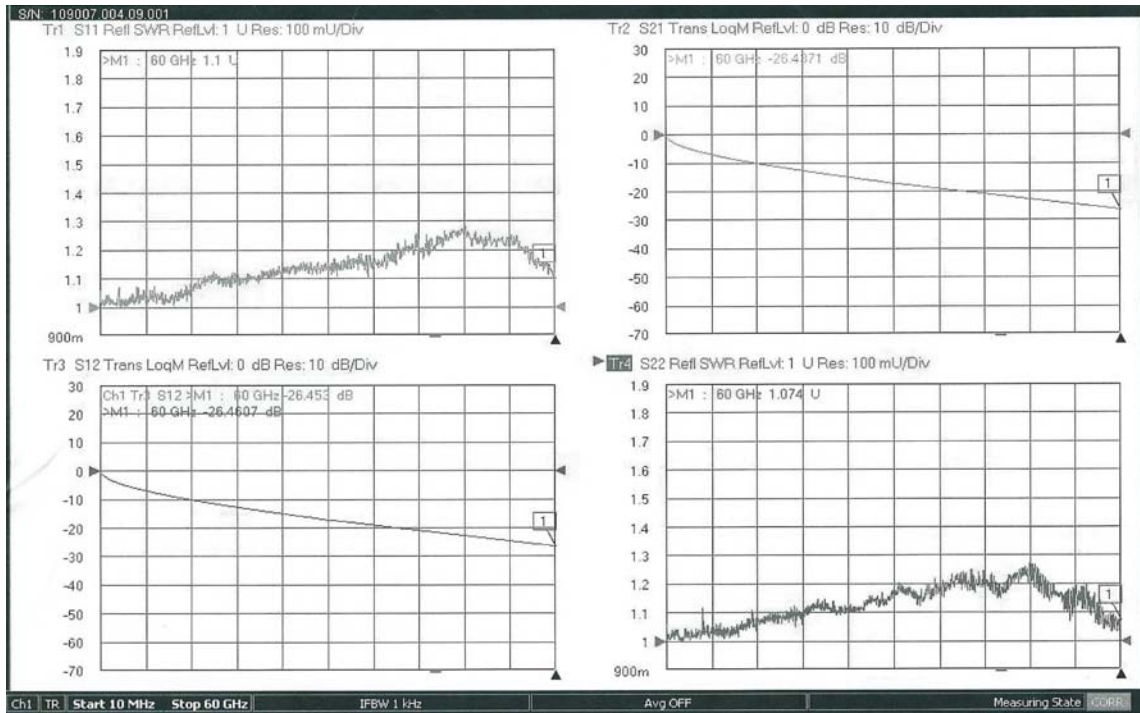
Figure B.12: Characteristics of the 4 m cable.
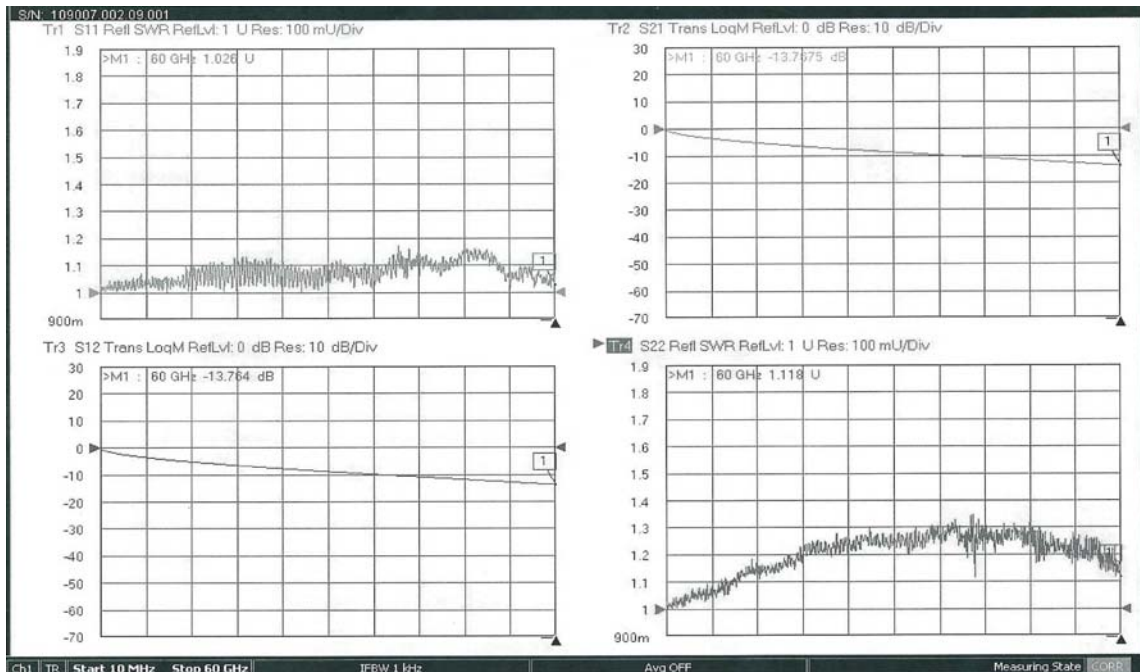
Figure B.13: Characteristics of the 2 m cable.

B.2.6 XY Positioning Board and Step Motors Linear Positioner

Two positioner have been used in the measurement campaigns, an *XY positioner* and a *liner positioner*.

The first one consists on a *XY positioning board* with two linear positioners (*X* and *Y*) that sample the two dimensions (Figure B14). This *XY* positioner (see Figure B.14) moves along *X* and *Y* axis by means of two *X* and *Y* step motors. The maximum area covered by these positioners is 70 cm × 70 cm. The accuracy is +/-.010" per foot [Robotics, 2014].
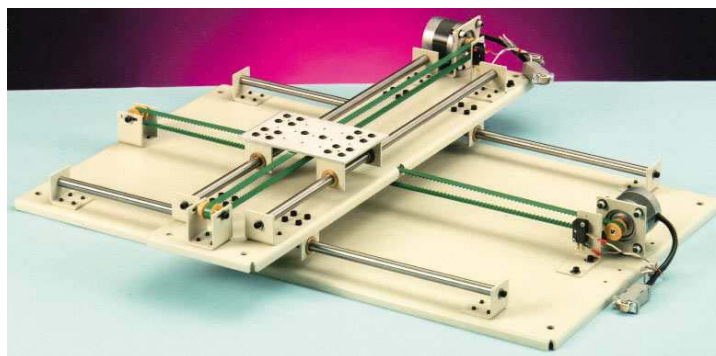
Figure B.14: *XY linear positioners* [Robotics, 2014].

The second positioner (Figure B.15) is a linear one, named *Single-axis tGlide* positioner. In this case, a step motor linear positioner moves along a single axis by means of one motor. The length covered is 1 meter, and two of them have been used in the measurements. The accuracy is similar to the *XY* one.

Figure B.15: *Single-axis tGlide positioner* [Robotics, 2014].

These two positioner (*XY* and *linear*), need to be moved and controlled. To accomplish this, two stepper motors (once per axis) are used for the *XY board*, and one for every linear positioner as shown in Figure B.16. Such motors are capable of moving the

linear positioners along its axis in two directions: forward or reverse. The step motors are controlled (and hence, the measurement procedure) by a driver, which is connected to the existing laptop via a parallel port. These movements have been fully integrated in the control software, which is described in next section.

Figure B.16: Step motors and controller [Robotics, 2014].

B.3 Software

The measurement procedure is controlled by an application developed in *Matlab* in this thesis. For every measurement campaign, the software is different because the scenario (either multiple diffraction or room characterization) and virtual array sampling (either linear or bidimensional) are different. These applications configure the equipment with the measurement parameters as well as it controls the measurement procedures.

As an example, the main interface of the used software in the measurement campaign shown in Chapter 4, Section 4.4, is shown in Figure B.17.

Figure B.17: Example of the software programm.

The main parameters that the user introduces in the software are:

- The initial and final frequencies over the band under analysis.

- The number of points to be sampled.

- The IF (Intermediate Frequency), that determines the noise floor.

- The transmitted power by the VNA (by default it was set to -10 dBm).

- Spatial sampling.

Once these parameters are set, the next step is the calibration process. The aim of this process is compensate the attenuation and phase shifts of cables, amplifiers and connectors. It should be remarked that since the antennas are not included in the calibration process, the effect of the antennas is included in measurement. Later, after a post processing this effect is eliminated. In the figure B.18, the connexion of the cables and the special tool for tightening are shown.
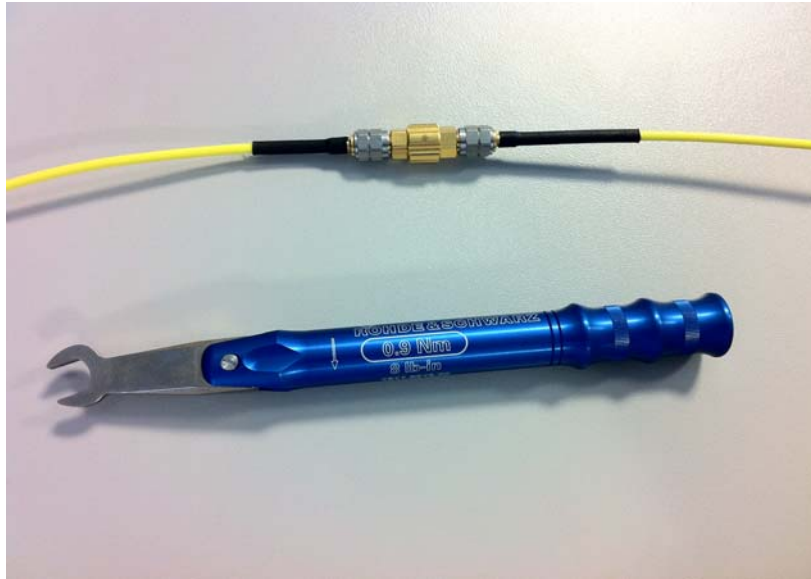
Figure B.18: Connexion of the cables for the calibration process.

The next step is to introduce the specific data of every measurement campaign. In the example of the Figure B.17, the *XY Positioning Board* is used for *Rx* antenna. In this case, a semicircular movement was implemented and all the data required by the software.

The last step is to start the measurements, when the acquisition process starts. First, the *VNA* saves the signal received by the receiving antenna. Then, the motors of the *XY Positioning Board* change the position to the next one. This process is repeated the number of times defined by the user in the software application.

Once the measurement routine has finished, the user can access to measured data in a PC folder. The calibration and the measurements are saved in different files, and the measurements are compensated in a post-processing.

Appendix C

Formulation for Radiowave

Multiple Diffraction

In Chapter 3, several formulation based on previous works have been used. This appendix addresses the preceding studies about radiowave multiple diffraction and it tries to context to the reader about it.

C.1 Introduction

The analysis of the multiple forward diffraction of radio waves past an array of buildings has been widely performed in order to predict the propagation of *UHF* signals in urban environments for cellular mobile radio and other personal communication networks [Maciel, 1993] [Erricolo, 2002bis]. This study has been realized for both the vertical plane [Bertoni, 2000] [COST 231, 1999] and the horizontal plane [Zhang, 2000] and, in order to

predict the above-mentioned multiple-building diffraction, many formulations have been proposed assuming a plane-wave incidence either based on *Physical Optics* (*PO*) [Vogler, 1982] [Walfisch, 1988] [Saunders, 1991] or the *Uniform Theory of Diffraction* (*UTD*) [Juan-Llácer, 1997] [Neve, 1994].

However, for microcellular mobile radio systems, in which the transmitting antenna is located at a certain distance from the array of buildings, a cylindrical or spherical-wave incidence assumption would be more appropriate for obtaining precise multiple diffraction loss predictions. In this sense, Xia and Bertoni proposed a *PO*-based solution, in which the field impinging over an array of successive absorbing knife edges of equal height which are modeling the buildings is represented by a multidimensional Fresnel integral expanded into a series of *Boersma's functions* [Xia, 1992]. Andersen gave a *UTD* solution for this multiple knife-edge diffraction, which includes slope diffraction, in order to solve the invalidity of a ray description when buildings are placed in the transition region near the shadow boundary [Andersen, 1994]. This solution can be applied for the analysis of a multiple diffraction caused by buildings of different heights; however, if a great number of the latter are considered, the computation time significantly increases. Zhang achieved an attenuation function for the prediction of the over-rooftop multiple forward diffraction, also replacing buildings by equal-height knife edges and defining a hybrid function which takes advantage of both *UTD* and *PO* [Zhang, 1999].

In the case of multiple diffraction caused by buildings modeled as wedges, Holm proposed a *UTD*-based formulation, deriving an expansion for higher order diffracted fields and removing some of the shortcomings of the original set from the *UTD* when the incident field is not ray-optical [Holm, 1996]. Tzaras and Saunders described a heuristic *UTD* approach for multiple-wedge diffraction modeling which incorporates slope diffraction terms, obtaining a balanced efficiency in terms of computation time and accuracy [Tzaras, 2001].

For the analysis of the multiple diffraction caused by buildings replaced by plateaux of rectangular crosssections, Luebbers proposed a solution which, presenting a heuristic wedge-diffraction coefficient extended to include slope diffraction, is valid for the case of lossy plateaux [Luebbers, 1989]. Moreover, Whitteker achieved a *PO* formulation for a multiple-rectangular plateau diffraction by creating a simple extension to the *Fresnel-Kirchhoff theory* of double knife-edge diffraction [Whitteker, 1990]. Haslett

proposed a *PO*-based method to predict the diffracted field strength in the shadow of a rectangular building [Haslett, 1994] Furthermore, a method based on the parabolic wave equation was given by Janaswamy and Andersen to predict path loss in an urban environment where buildings are assumed to be flat and reflective [Janaswamy, 2000]. Holm described a new heuristic *UTD* diffraction coefficient for non-perfectly conducting wedges, which allows the analysis of diffraction over rectangular plateaus that is, at the same time, valid deep in the shadow region, where the Luebbers coefficient fails [Holm, 2000]. Finally, Erricolo and Uslenghi have developed a two-dimensional, ray-tracing, polygonal line simulator to analyze multiple diffractions over a series of rectangular buildings, comparing the results with measurements and obtaining a solid agreement [Erricolo, 2001]. It should be pointed out that, in all of the above-mentioned works obtained for analyzing multiple diffraction caused by rectangular plateaux, there are only results considering a small number of buildings presented.

However, when considering that the objects obstructing the propagation path between the transmitter and the receiver have a rounded shape, such as hills, a cylindrical structure modeling the obstacles could be more appropriate in order to accurately predict radio signal path loss. In this sense, Koutitas and Tzaras have presented in [Koutitas, 2006] a *UTD*-based formulation which successfully analyzes multiplecylinder diffraction through the incorporation of the *slope diffraction* mechanism. This mechanism ensures continuous, accurate field predictions around the shadow region of the scenario under study. Nevertheless, such incorporation usually increases both the mathematical complexity and the computational efficiency of the solution.

In this Appendix, by considering the final solution for the study of the multiple diffraction caused by an array of wedges presented in [Rodríguez, 2007] and [Rodríguez, 2008], formulations expressed in terms of *UTD* coefficients for the prediction of the multiple diffraction produced by an array of rectangular plateaux and by a series of cylinders, considering spherical-wave incidence, are detailed.

The major advantage of the proposed solutions is that, as only single diffractions over obstacles are involved in the calculations, both the computation time and mathematical complexity are reduced over existing formulations, permitting a fast analysis of the multiple diffraction produced by a great number of buildings. Furthermore, the presented solution is valid for both the vertical and the horizontal plane.

C.2 Formulation for the Multiple Diffraction of Spherical Waves by a Series of Rectangular Plateaux

For this particular case, an idealized representation of the considered propagation environment can be observed in Figure C.1, where n buildings of the same height, which is relative to the base station antenna height *H*, having the same thickness *v*, have been taken into account, assuming that their cross sections are rectangular and that there is a constant inter-building spacing *w*.
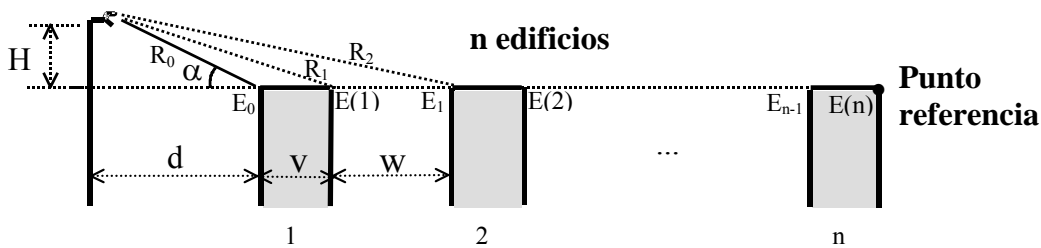
Figure C.1: Scheme of the considered propagation environment, assuming buildings modeled as rectangular plateaux.

For multiple diffraction analysis purposes, this configuration can be seen as in Figure C.2, where a series of wedges made of interior angle π/2 radians, joined two by two, forming the flat-roofed buildings.

Figure C.2: Rectangular obstacle seen as a combination of two joined wedges of interior angle π/2 rad.

Therefore, assuming this geometry, when *n = 1*, and being

$$E_0 = \frac{E_i}{R_0} \exp(-jkR_0) \quad (C.1)$$

the field which reaches the left-placed wedge forming the rooftop of the first building, as indicated in Figure C.3.
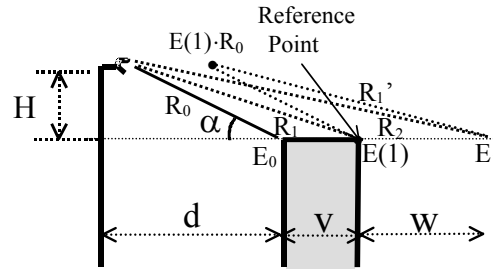
Figure C.3: Geometry of the propagation environment in Figure C.1, considering that n=1.

where E_i is the relative amplitude of the spherical source. $E(1)$ can be expressed as

$$
\begin{aligned}
E(1) &= \frac{E_i}{R_1}\exp(-jkR_1) + \frac{E_i}{R_0}\exp(-jkR_0)\sqrt{\frac{R_0}{v(R_0+v)}}D\left(\phi=\frac{3\pi}{2},\phi'=\frac{\pi}{2}+\alpha\right)\exp(-jkv) \\
&= E_0\left(\frac{R_0}{R_1}\exp(-jk(R_1-R_0)) + \sqrt{\frac{R_0}{v(R_0+v)}}D\left(\phi=\frac{3\pi}{2},\phi'=\frac{\pi}{2}+\alpha\right)\exp(-jkv)\right) \quad (C.2)
\end{aligned}
$$

where

$$
\begin{aligned}
E_1 &= \frac{1}{2}\left[\frac{E_i}{R_2}\exp(-jkR_2) + E_0\sqrt{\frac{R_0}{(v+w)(R_0+v+w)}}D\left(\phi=\frac{3\pi}{2},\phi'=\frac{\pi}{2}+\alpha\right)\exp(-jk(v+w))\right. \\
&\quad \left. + E(1)\left(\frac{R_0}{R_1{}'}\exp(-jk(R_2-R_1)) + \sqrt{\frac{R_0}{w(R_0+w)}}D(\phi=\pi,\phi'=\alpha)\exp(-jkw)\right)\right] \\
&= \frac{1}{2}\left[E_0\left(\frac{R_0}{R_2}\exp(-jk(R_2-R_0)) + \sqrt{\frac{R_0}{(v+w)(R_0+v+w)}}D\left(\phi=\frac{3\pi}{2},\phi'=\frac{\pi}{2}+\alpha\right)\exp(-jk(v+w))\right)\right. \\
&\quad \left. + E(1)\left(\frac{R_0}{R_1{}'}\exp(-jk(R_2-R_1)) + \sqrt{\frac{R_0}{w(R_0+w)}}D(\phi=\pi,\phi'=\alpha)\exp(-jkw)\right)\right] \quad (C.3)
\end{aligned}
$$

E_1 is the field impinging over the left corner of the second building, which has been calculated following the method based on virtual spherical sources. $D(\phi, \phi', L)$ is the diffraction coefficient for a finitely conducting wedge, as given in Luebbers [1984].

In Figure C.4, it is showed the scheme for *n=2*.
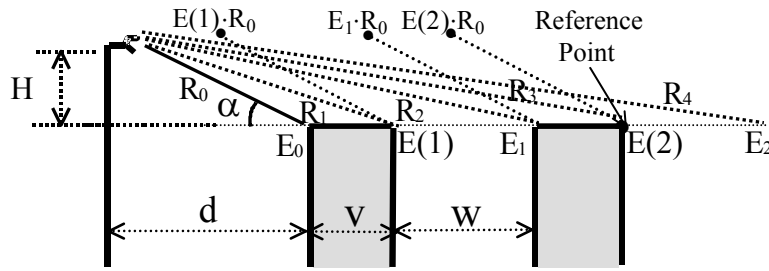
Figure C.4: Geometry of the propagation environment in Figure C.1, considering that n=2.

The field reaching the reference point of Figure C.4, *E(2)*, can be obtained as

$$E(2) = \frac{1}{3}\left[E_0\left(\frac{R_0}{R_3}\exp(-jk(R_3 - R_0)) \right.\right.$$

$$\left. + \sqrt{\frac{R_0}{(2v+w)(R_0 + 2v+w)}}D\left(\phi = \frac{3\pi}{2}, \phi' = \frac{\pi}{2} + \alpha \right)\exp(-jk(2v+w)) \right)$$

$$+ E(1)\left(\frac{R_0}{R_2}\exp(-jk(R_3 - R_1)) + \sqrt{\frac{R_0}{(v+w)(R_0 + v+w)}}D(\phi = \pi, \phi' = \alpha)\exp(-jk(v+w)) \right)$$

$$+ E_1\left(\frac{R_0}{R_1}\exp(-jk(R_3 - R_2)) + \sqrt{\frac{R_0}{v(R_0 + v)}}D\left(\phi = \frac{3\pi}{2}, \phi' = \frac{\pi}{2} + \alpha \right)\exp(-jkv) \right] \quad (C.4)$$

where

$$E_2 = \frac{1}{4}\left[E_0\left(\frac{R_0}{R_4}\exp(-jk(R_4 - R_0)) \right.\right.$$

$$\left. + \sqrt{\frac{R_0}{(2v+2w)(R_0 + 2v+2w)}}D\left(\phi = \frac{3\pi}{2}, \phi' = \frac{\pi}{2} + \alpha \right)\exp(-jk(2v+2w)) \right)$$

$$+ E(1)\left(\frac{R_0}{R_3'}\exp(-jk(R_4 - R_1)) + \sqrt{\frac{R_0}{(v+2w)(R_0 + v+2w)}}D(\phi = \pi, \phi' = \alpha)\exp(-jk(v+2w)) \right)$$

$$+ E_1\left(\frac{R_0}{R_2}\exp(-jk(R_4 - R_2)) + \sqrt{\frac{R_0}{(v+w)(R_0 + v+w)}}D\left(\phi = \frac{3\pi}{2}, \phi' = \frac{\pi}{2} + \alpha \right)\exp(-jk(v+w)) \right)$$

$$+ E(2)\left(\frac{R_0}{R_1'}\exp(-jk(R_4 - R_3)) + \sqrt{\frac{R_0}{w(R_0 + w)}}D(\phi = \pi, \phi' = \alpha)\exp(-jkw) \right) \right] \quad (C.5)$$

Therefore, the proposed formulation can now be written, for *n ≥ 1* and considering that *α > 0*, as

$$
\begin{aligned}
E(n) = \frac{1}{2n-1} \Bigg\{ & \sum_{m=0}^{n-1} E_m \Bigg[\frac{R_0}{R_{2(n-m)-1}} \exp[-jk(R_{2n-1} - R_{2m})] \\
& + \sqrt{\frac{R_0}{[(n-m)(v+w)-w][R_0 + (n-m)(v+w)-w]}} \\
& \cdot D\!\left(\phi' = \frac{\pi}{2} + \alpha, \phi = \frac{3\pi}{2}, L = \sqrt{\frac{R_0[(n-m)(v+w)-w]}{R_0 + [(n-m)(v+w)-w]}} \right) \cdot \exp[-jk[(n-m)(v+w)-w]] \Bigg] \\
& + \sum_{p=1}^{n-1} E(p) \Bigg[\frac{R_0}{R_{2(n-p)}} \exp[-jk(R_{2n-1} - R_{2p-1})] + \sqrt{\frac{R_0}{(n-p)(v+w)[R_0 + (n-p)(v+w)]}} \\
& \cdot D\!\left(\phi' = \alpha, \phi = \pi, L = \sqrt{\frac{R_0(n-p)(v+w)}{R_0 + (n-p)(v+w)}} \right) \cdot \exp[-jk(n-p)(v+w)] \Bigg] \Bigg\} \quad (C.6)
\end{aligned}
$$

where

$$
R_x = \begin{cases} \sqrt{\left[d + \dfrac{x}{2}(v+w) \right]^2 + H^2}, & x \quad par \\[4mm] \sqrt{\left[d + \dfrac{x-1}{2}(v+w) + v \right]^2 + H^2}, & x \quad impar \end{cases} \quad (C.7)
$$

and E_m is the field reaching the left-placed corners of the rooftops, as observed in Figure C.1. Thus, for $m \geq 1$,

$$
\begin{aligned}
E_m = \frac{1}{2m} \Bigg\{ & \sum_{q=0}^{m-1} E_q \Bigg[\frac{R_0}{R_{2(m-q)}} \exp[-jk(R_{2m} - R_{2q})] \\
& + \sqrt{\frac{R_0}{(m-q)(v+w)[R_0 + (m-q)(v+w)]}} \\
& \cdot D\!\left(\phi' = \frac{\pi}{2} + \alpha, \phi = \frac{3\pi}{2}, L = \sqrt{\frac{R_0(m-q)(v+w)}{R_0 + (m-q)(v+w)}} \right) \cdot \exp[-jk(m-q)(v+w)] \Bigg] \\
& + \sum_{r=1}^{m} E(r) \Bigg[\frac{R_0}{R'_{2(m-r)+1}} \exp[-jk(R_{2m} - R_{2r-1})] + \sqrt{\frac{R_0}{[(m-r)(v+w)+w][R_0 + (m-r)(v+w)+w]}} \\
& \cdot D\!\left(\phi' = \alpha, \phi = \pi, L = \sqrt{\frac{R_0[(m-r)(v+w)+w]}{R_0 + [(m-r)(v+w)+w]}} \right) \cdot \exp[-jk[(m-r)(v+w)+w]] \Bigg] \Bigg\} \quad (C.8)
\end{aligned}
$$

where

$$
R'_x = \sqrt{\left[d + \frac{x-1}{2}(v+w) + w \right]^2 + H^2} \quad (C.9)
$$

It should be noted that, with the proposed theoretical formulation for this particular case, the analysis of the diffraction of spherical waves impinging on the array of buildings, with an angle of incidence smaller than zero ($\alpha < 0$), could not be carried out, since, in this case, the above-mentioned spherical waves would hit the rightplaced wedges which form the roof cross-sections from inside the building, which is meaningless for this purpose.

C.3 Formulation for the Multiple Diffraction of Spherical Waves by a Series of Cylinders

In Figure C.5, a schematic of the considered propagation environment is displayed. A series of n perfectly conducting cylinders of the same height (relative to the transmitter antenna height H), constant inter-cylinder spacing w, and the same radius of curvature r, have been taken into account. Additionally, the source is at an arbitrary height (above, level with, or below the average cylinder height), and is located at a certain distance d from the array of cylinders.
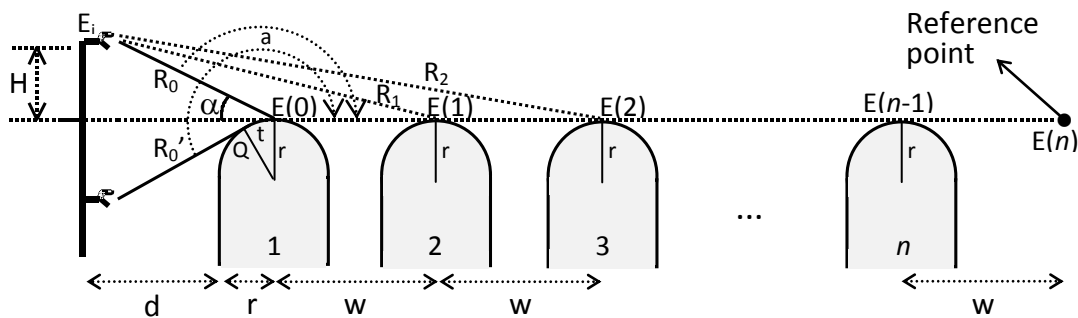
Figure C.5. Schematic of the considered propagation environment.

First, we consider the base station antenna above the average rooftop height ($H \geq 0$), when $n = 0$ (absence of cylinders) as Figure C.6.
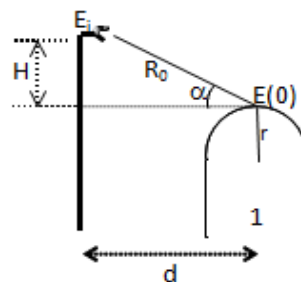
Figure C.6: Schematic for $n = 0$ (absence of cylinders).

The observed field at the reference point in Figure C.6 (the field that impinges on the first cylinder) can be expressed as

$$E_0 = \frac{E_i}{R_0} \exp(-jkR_0) \quad (C.10)$$

being that E_i is the relative amplitude of a spherical source and k is the wave number.

Next, for $n = 1$, the scenario is depicted in Figure C.7.
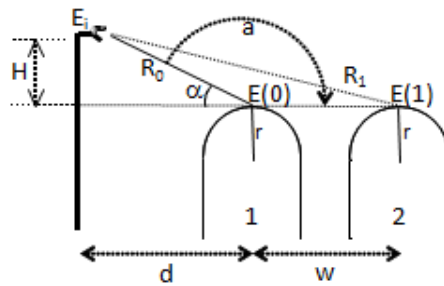
Figure C.7: Scheme for n=1 cylinder.

When $n = 1$, the field arriving at the reference point can be written as

$$
\begin{aligned}
E(1) &= \frac{E_i}{R_1} e^{-jkR_1} + \frac{E_i}{R_0} e^{-jkR_0} \sqrt{\frac{R_0}{w(R_0 + w)}} \cdot R_{s,h}(a) e^{-jkw} \\
&= E(0)\left(\frac{R_0}{R_1} e^{-jk(R_1 - R_0)} + \sqrt{\frac{R_0}{w(R_0 + w)}} \cdot R_{s,h}(a) e^{-jkw} \right)
\end{aligned}
\quad (C.11)
$$

where

$$R_{s,h}(a) = -\sqrt{\frac{r}{m'}} e^{-j\frac{\varepsilon^3(a)}{12}} e^{-j\frac{\pi}{4}} \left\{ \frac{-F[X(a)]}{2\varepsilon(a)\sqrt{\pi}} + \begin{bmatrix} p*(\varepsilon(a)) \\ q*(\varepsilon(a)) \end{bmatrix} \right\} \quad (C.12)$$

$R_{s,h}(a)$ is the reflection coefficient for both *soft/horizontal* (s) and *hard/vertical* (h) polarizations, where $F[X]$ is the so-called transition function (which is defined in terms of a Fresnel integral) $p*(\varepsilon(a))$ and $q*(\varepsilon(a))$ are the *Fock* scattering functions for *soft* and *hard* polarizations, respectively, which are dependent on the electrical characteristics of the cylinders [Pathak, 1979] , and

$$X(a) = 2kL\cos^2\left(\frac{a}{2}\right)$$

$$L = \frac{R_0(n-m)w}{R_0 + (n-m)w} \qquad (C.13)$$

$$\varepsilon(a) = -2m'\cos^2\left(\frac{a}{2}\right)$$

where a is the angle indicated in Figure C.5 and $m' = (kr=2)^{1/3}$.

When $n = 2$ (see Figure C.8), the multiple diffraction appears and $E(2)$ can be obtained by following the same methodology of virtual spherical sources presented in [Rodríguez, 2007] as the average of two field contributions coming from two spherical wave fronts impinging on every cylinder.
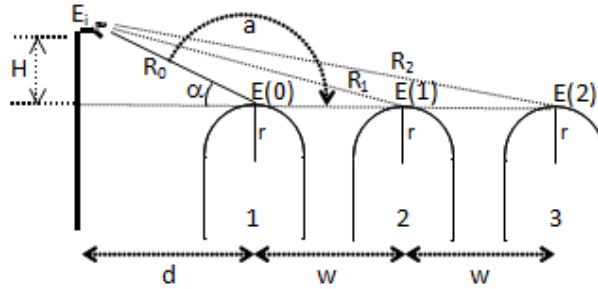
Figure C.8: Scheme for n=2 cylinders.

Therefore

$$E(2) = \frac{1}{2}\left[E'(2) + E''(2)\right] \quad (C.14)$$

where

$$E'(2) = \frac{E_i}{R_2}e^{-jkR_2} + E(0)\sqrt{\frac{R_0}{2w(R_0 + 2w)}} \cdot R_{s,h}(a)e^{-jk2w}$$

$$= E(0)\left(\frac{R_0}{R_2}e^{-jk(R_2-R_0)} + \sqrt{\frac{R_0}{2w(R_0 + 2w)}} \cdot R_{s,h}(a)e^{-jk2w}\right) \qquad (C.15)$$

and

$$E''(2) = E(1)\left(\frac{R_0}{R_1}e^{-jk(R_2-R_1)} + \sqrt{\frac{R_0}{w\cdot(R_0 + w)}} \cdot R_{s,h}(a)e^{-jkw}\right) \quad (C.16)$$

Hence, the final expression for *E(2)* can be written as

$$
E(2) = \frac{1}{2}\left[E(0)\left(\frac{R_0}{R_2}e^{-jk(R_2-R_0)} + \sqrt{\frac{R_0}{2w(R_0+2w)}} \cdot R_{s,h}(a)e^{-jk2w} \right) \right.
$$
$$
\left. + E(1)\left(\frac{R_0}{R_1}e^{-jk(R_2-R_1)} + \sqrt{\frac{R_0}{w(R_0+w)}} \cdot R_{s,h}(a)e^{-jkw} \right) \right] \quad (C.17)
$$

In this way, if we generalize the previous process in the case of n cylinders and assume the far-field approximation by which *d >> r, w >> r, d >> t, w >> t*, the field reaching the reference point indicated in Figure C.5 can be expressed, for *n > 1*, as follows.

a) Transmitting point above or level with the average cylinder height ($H \geq 0$, $\alpha \geq 0$)

$$
E(n) = \frac{1}{n}\sum_{m=0}^{n-1} E(m)\left[\frac{R_0}{R_{n-m}}e^{-jk(R_n-R_m)} + \sqrt{\frac{R_0}{(n-m)w[R_0+(n-m)w]}}R_{s,h}(a)e^{-jk(n-m)w} \right] \quad (C.18)
$$

b) Transmitting point below the average cylinder height ($H < 0$, $\alpha < 0$)

$$
E(n) = \frac{1}{n}\sum_{m=0}^{n-1} E(m)\sqrt{\frac{R_0{}'}{(n-m)w[R_0{}'+(n-m)w]}}T_{s,h}(a)e^{-jk(n-m)w} \quad (C.19)
$$

being that in this case

$$
E(0) = \frac{E_i}{R_0{}'}\sqrt{\frac{R_0{}'}{R_0{}'+t(a)}}e^{-jkR_0{}'}e^{-jkt(a)} \approx \frac{E_i}{R_0{}'}e^{-jkR_0{}'}e^{-jkt(a)} \quad (C.20)
$$

and

$$
T_{s,h}(a) = -m'\sqrt{\frac{2}{k}}e^{-j\frac{\pi}{4}}\left\{ \frac{-F[X(a)]}{2\varepsilon(a)\sqrt{\pi}} + \left[\begin{array}{c} p*(\varepsilon(a)) \\ q*(\varepsilon(a)) \end{array} \right] \right\} \quad (C.21)
$$

is the diffraction coefficient for both *soft* (s) and *hard (h)* polarizations, where

$$X(a) = \frac{kL(a - \pi)^2}{2}$$
$$L = \frac{R_0'(n - m)w}{R_0' + (n - m)w} \quad (C.22)$$
$$\varepsilon(a) = m'(a - \pi)$$
$$t(a) = r(a - \pi)$$

It should be noted that, in (C.19), the term which refers to the direct rays in (C.18) does not appear. Furthermore, for cylinders with very small values of radius of curvature, the presented solution perfectly converges with that given in [Rodríguez, 2007] regarding multiple diffraction over a series of knife edges.

Appendix D

Diffuse Scattering Parametric Study

In this appendix, table of the parametric study for the three materials studied in Chapter 4 are shown. These materials are glass, chipboard and plasterboard. For all materials, simulations have been run using the two diffuse scatter model presented in Chapter 4: directive and Lambertian. The first one needs two parameters (s and α), while the second one only s. First table for each material shows the range of simulated values, highlighting in green the best fitting one. In the case of directive, since two parameters are shown, a second table is presented for a better fitting of α. Results will show that directive model is not sensitive to α.

D.1 Glass

Directive model Parameters		Glass					
		90°		120°		60°	
S	α_R	Mean	NMSE	Mean	NMSE	Mean	NMSE
0.05	10	5.9469	0.8185	3.4858	0.6832	3.4338	1.9362
0.05	5	5.9174	0.8053	3.4981	0.6788	3.4257	1.8932
0.05	2	5.9218	0.8125	3.5165	0.6895	3.4297	1.9466
0.07	10	5.8721	0.8180	3.3891	0.6590	3.4858	1.9313
0.07	5	5.6585	0.7866	3.3781	0.6578	3.4278	1.9308
0.07	2	5.7140	0.7856	3.3991	0.6676	3.4534	1.9502
0.1	10	6.0101	0.8120	3.3477	0.6502	3.4244	1.9313
0.1	5	5.6418	**0.7804**	3.3191	0.6513	3.4090	**1.9085**
0.1	2	5.5988	**0.7772**	3.3264	**0.6449**	3.4424	1.9318
0.2	10	6.9924	0.9066	4.1638	0.7778	3.3803	1.8882
0.2	5	6.7563	0.8787	3.8228	0.7283	3.4885	1.9647
0.2	2	6.4980	0.8572	3.6716	0.6921	3.3325	1.8977
0.3	10	8.1183	1.0311	5.5256	0.9992	3.6302	1.9814
0.3	5	8.0219	1.0114	5.0742	0.9219	3.5329	1.9844
0.3	2	7.8671	0.9932	4.7639	0.8749	3.4511	1.9206
0.4	10	9.6469	1.1916	6.9197	1.2073	4.0689	2.1782
0.4	5	9.2608	1.1412	6.2213	1.1144	3.6745	2.0477
0.4	2	8.5252	1.0633	5.7652	1.0350	3.5710	2.0025
0.5	10	10.8274	1.3298	8.0460	1.3714	4.8687	2.5185
0.5	5	10.1055	1.2470	7.5281	1.3264	4.0234	2.2011
0.5	2	9.5487	1.1852	6.8367	1.2108	3.7862	2.0857
0.6	10	11.5535	1.4188	9.2433	1.5631	5.3770	2.7887
0.6	5	11.0647	1.3572	8.2347	1.4024	4.6046	2.4456
0.6	2	10.6393	1.3151	7.7981	1.3620	4.0792	2.2274
0.7	10	12.1669	1.4917	10.3100	1.7230	5.9128	2.9743
0.7	5	12.0867	1.4835	9.6706	1.6472	4.9507	2.5844
0.7	2	11.3004	1.4027	8.4705	1.4808	4.3390	2.3252
0.8	10	12.9630	1.5842	10.8968	1.8169	6.8425	3.4025
0.8	5	12.5227	1.5497	10.4940	1.7747	5.7202	2.9081
0.8	2	11.8442	1.4604	9.1740	1.5697	4.7325	2.4835
Lambertian Parameter		Media	NMSE	Media	NMSE	Media	NMSE
S=0.05		6.0391	0.8265	3.5776	0.6998	3.4088	1.9002
S=0.07		5.6680	**0.7864**	3.4604	0.6774	3.4945	1.9530
S=0.1		5.8165	0.7961	3.2672	**0.6423**	3.3496	**1.9167**
S=0.2		6.3955	0.8490	3.5168	0.6768	3.4988	1.9826
S=0.3		7.5072	0.9587	4.1532	0.7701	3.3837	**1.9154**
S=0.4		8.7737	1.1001	5.2473	0.9585	3.5012	1.9287
S=0.5		9.8387	1.2188	5.8457	1.0482	3.5421	1.9839
S=0.6		10.3298	1.2770	6.9045	1.2016	3.7923	2.0851
S=0.7		11.2870	1.3975	7.6803	1.3331	4.0689	2.2014
S=0.8		11.6400	1.4358	8.3047	1.4310	4.3516	2.3308

Table D.1.: Parametric study of the glass.

Parameters		Glass					
		90°		120°		60°	
S	α_R	Mean	NMSE	Mean	NMSE	Mean	NMSE
0.07	10	5.7336	0.8559	2.4352	0.4798	2.4927	2.0970
0.07	9	5.6100	0.8417	2.3785	0.4689	2.4885	2.0955
0.07	8	5.4805	0.8202	2.4402	0.4761	2.4851	2.0749
0.07	7	5.5998	0.8285	2.4219	0.4739	2.4790	2.0947
0.07	6	5.3857	0.8147	2.4505	0.4752	2.4574	2.0853
0.07	5	5.3185	0.8005	2.4400	0.4763	2.4514	2.0802
0.07	4	5.3572	0.7934	2.4151	0.4717	2.4515	2.0738
0.07	3	5.2830	0.7864	2.4079	0.4731	2.3704	2.0251
0.07	2	5.3110	0.7867	2.4170	0.4756	2.4217	2.0549
0.07	1	5.2157	0.7819	2.4631	0.4791	2.4685	2.0966
0.07	10	5.6689	0.8282	2.4202	0.4940	2.4602	2.0799
0.1	9	5.6392	0.8195	2.4222	0.4933	2.4808	2.1078
0.1	8	5.5573	0.8007	2.4251	0.4836	2.4301	2.0646
0.1	7	5.4769	0.7934	2.4014	0.4873	2.4270	2.0568
0.1	6	5.3281	0.7880	2.3454	0.4722	2.4803	2.0977
0.1	5	5.3997	0.7895	2.3384	0.4783	2.4503	2.0959
0.1	4	5.0712	0.7554	2.3382	0.4707	2.4358	2.0793
0.1	3	5.0999	0.7507	2.3591	0.4808	2.3989	2.0361
0.1	2	5.1007	0.7491	2.4921	0.4887	2.5661	2.1415
0.1	1	5.0321	0.7474	2.2857	0.4666	2.4551	2.0662

Table D.2.: Low range parametric study of the glass.

D.2 Chipboard

| Directive model Parameters | | Chipboard | | | | | |
| | | 90° | | 120° | | 60° | |
S	α_R	Mean	NMSE	Mean	NMSE	Mean	NMSE
0.05	10	8.6100	1.6940	5.1725	1.6078	5.0747	2.4451
0.05	5	8.4197	1.6510	5.2274	1.6250	5.0750	2.4524
0.05	2	8.6108	1.6914	5.1542	1.6015	5.1421	2.4818
0.1	10	7.2594	1.4093	5.1456	1.5903	4.6898	2.3038
0.1	5	6.9342	1.3238	5.1122	1.5863	4.8311	2.3487
0.1	2	7.0144	1.3323	5.1033	1.5780	4.9541	2.3962
0.2	10	5.1074	0.9733	4.4281	1.3949	3.9607	2.0376
0.2	5	4.7751	0.8733	4.5232	1.4105	3.8443	2.0032
0.2	2	4.6227	0.8137	4.7142	1.4715	4.1063	2.0652
0.3	10	3.9116	0.7583	3.9259	1.2891	3.5425	1.9636
0.3	5	3.5457	0.6257	3.9396	1.2698	3.3626	1.8896
0.3	2	3.4684	0.5951	4.2041	1.3353	3.6553	1.9556
0.4	10	3.0061	0.5946	3.7518	1.2447	4.2270	2.1660
0.4	5	2.5212	0.4675	3.5614	1.1969	3.6271	1.9742
0.4	2	2.2857	0.4308	4.0526	1.2992	3.1219	**1.8577**
0.5	10	3.0961	0.5615	3.6609	1.2895	5.0220	2.3798
0.5	5	2.5387	0.4762	3.3525	**1.1923**	4.2045	2.1601
0.5	2	1.8765	**0.3823**	3.4847	1.2013	3.3880	1.9360
0.6	10	3.5603	0.6325	4.0422	1.3656	5.9103	2.6860
0.6	5	2.8144	0.5079	3.5232	1.2167	5.2322	2.4286
0.6	2	2.5311	0.4772	3.4727	1.2053	4.0042	2.1264
0.7	10	4.0455	0.6914	4.4815	1.4407	6.9004	2.9873
0.7	5	3.4632	0.6022	4.1775	1.3689	5.9610	2.6580
0.7	2	3.2720	0.5683	3.4344	1.2032	4.8354	2.3225
0.8	10	4.5656	0.7693	4.9434	1.5716	7.6529	3.3454
0.8	5	4.3634	0.7509	4.3039	1.3975	6.4959	2.8794
0.8	2	3.8633	0.6497	3.7315	1.2670	5.5394	2.5265
Lambertian Parameter		Mean	NMSE	Mean	NMSE	Mean	NMSE
S=0.05		8.4886	1.6667	5.2142	1.6220	5.1520	2.4812
S=0.1		6.9854	1.3282	5.2146	1.6320	5.0846	2.4610
S=0.2		4.8785	0.8703	4.9284	1.5259	4.4037	2.1843
S=0.3		3.5150	0.6101	4.5648	1.4166	3.9317	2.0302
S=0.4		2.4426	0.4431	4.0889	1.2958	3.6400	1.9583
S=0.5		2.0778	**0.4005**	3.7693	1.2514	3.5649	**1.9407**
S=0.6		2.2249	0.4360	3.5590	**1.2210**	3.5659	1.9446
S=0.7		2.8982	0.5327	3.5303	1.2345	4.3471	2.1713
S=0.8		3.6082	0.6345	3.9710	1.3399	4.7610	2.3098

Table D.3.: Parametric study of the chipboard.

Parameters		Chipboard					
		90°		120°		60°	
S	α_R	Mean	NMSE	Mean	NMSE	Mean	NMSE
0.4	10	3.2402	0.6368	3.7495	1.2623	4.2764	2.1830
0.4	9	2.6974	0.5473	3.6794	1.2392	3.9051	2.0872
0.4	8	2.7619	0.5245	3.5260	1.2082	3.8859	2.0863
0.4	7	2.5215	0.4847	3.5243	1.2252	3.8539	2.0787
0.4	6	2.6032	0.4978	3.5248	1.2009	3.7210	2.0328
0.4	5	2.5723	0.4700	3.7110	1.2396	3.6513	1.9880
0.4	4	2.1018	0.4206	3.7668	1.2603	3.6150	1.9529
0.4	3	2.1579	0.3984	3.6367	1.2327	3.2232	1.8804
0.4	2	2.4771	0.4449	3.8923	1.2732	3.4749	1.9041
0.4	1	2.4564	0.4293	4.0614	1.3129	3.2141	1.8678
0.5	10	3.3193	0.6072	3.7369	1.2798	4.8611	2.3390
0.5	9	2.9242	0.5664	3.6887	1.2622	4.8799	2.3827
0.5	8	2.8113	0.5250	3.6360	1.2555	4.6571	2.3275
0.5	7	2.6538	0.4914	3.3801	1.2055	4.7032	2.3098
0.5	6	2.4883	0.4557	3.3529	1.1992	4.4512	2.2257
0.5	5	2.3395	0.4591	3.3353	1.2031	4.0911	2.1234
0.5	4	2.0262	0.4281	3.3096	1.2065	3.9112	2.0840
0.5	3	2.0981	0.4033	3.2742	1.1671	3.7785	2.0377
0.5	2	2.1395	0.4228	3.4791	1.2122	3.5190	1.9561
0.5	1	1.9643	0.3909	3.4680	1.2011	3.2377	1.8759
0.6	10	3.2666	0.5731	4.0708	1.3534	5.9720	2.7317
0.6	9	3.4800	0.6145	3.8913	1.3348	5.7098	2.6005
0.6	8	2.9498	0.5223	3.8631	1.3032	5.4818	2.5592
0.6	7	2.8841	0.5252	3.7423	1.2950	5.4101	2.5112
0.6	6	3.0080	0.5610	3.6980	1.2571	5.3400	2.4926
0.6	5	2.8137	0.5127	3.7800	1.2797	4.9788	2.3388
0.6	4	2.7871	0.5135	3.6753	1.2387	4.7915	2.2996
0.6	3	2.6951	0.5055	3.5062	1.2302	4.2750	2.1638
0.6	2	2.4655	0.4630	3.2539	1.1918	4.0406	2.0795
0.6	1	2.3984	0.4531	3.2519	1.1900	3.6426	1.9914

Table D.4.: Low range parametric study of the chipboard.

.

D.3 Plasterboard

Directive model Parameters		Plasterboard					
		90°		120°		60°	
S	α_R	Mean	NMSE	Mean	NMSE	Mean	NMSE
0.05	10	9.5051	2.2124	8.3756	2.2422	5.1478	1.3410
0.05	5	9.6501	2.2531	8.5773	2.3034	5.3409	1.3704
0.05	2	9.8190	2.3053	8.9208	2.4045	5.2024	1.3300
0.1	10	7.6705	1.7569	6.9368	1.8697	4.6423	1.1991
0.1	5	7.6469	1.7406	7.4373	1.9895	4.8161	1.2416
0.1	2	7.5922	1.7432	7.8855	2.1222	5.1651	1.3344
0.2	10	5.3508	1.1875	4.1664	1.1622	3.2457	0.8836
0.2	5	4.8214	1.0540	4.7713	1.3297	3.4174	0.9362
0.2	2	5.0249	1.1047	5.9209	1.6059	3.9993	1.0858
0.3	10	3.7537	0.8249	2.4110	0.7426	2.7961	0.7309
0.3	5	3.2901	0.7053	3.3856	0.9819	2.8199	0.7742
0.3	2	3.3451	0.7298	3.9611	1.1636	3.1619	0.8735
0.4	10	2.8240	0.6016	2.2934	**0.6074**	2.8471	0.7215
0.4	5	2.4861	0.5342	2.6486	0.7824	2.9197	0.7561
0.4	2	2.6589	0.5849	3.2488	0.9278	2.7128	**0.7091**
0.5	10	2.6579	0.5976	2.8972	0.7147	3.7823	0.9070
0.5	5	2.1901	**0.5116**	2.7934	0.7552	2.9572	0.7281
0.5	2	2.1969	**0.5166**	2.8116	0.8219	2.7354	**0.7059**
0.6	10	3.0928	0.6927	3.5963	0.8538	4.5445	1.0940
0.6	5	2.6649	0.5925	3.3284	0.8237	4.0012	0.9394
0.6	2	2.5052	0.5597	2.9456	0.8169	3.2065	0.7889
0.7	10	3.4644	0.7723	4.3798	1.0690	5.0514	1.2192
0.7	5	3.3566	0.7014	3.8487	0.9529	4.5566	1.0605
0.7	2	3.0648	0.6709	3.0010	0.7653	3.5490	0.8592
0.8	10	4.4768	0.9243	5.1948	1.2569	6.2507	1.4782
0.8	5	4.0414	0.8314	4.4805	1.1190	5.0139	1.2040
0.8	2	3.6964	0.7883	3.7334	0.9389	4.0787	0.9883
Lambertian Parameter		Mean	NMSE	Mean	NMSE	Mean	NMSE
S=0.05		9.9369	2.3275	9.0270	2.4166	5.4149	1.3992
S=0.1		7.8414	1.7965	8.1842	2.1960	5.1776	1.3333
S=0.2		5.3302	1.1705	6.8265	1.8099	4.4591	1.1620
S=0.3		3.8000	0.7945	4.8762	1.2914	3.8117	0.9955
S=0.4		2.6372	0.5711	3.6643	0.9902	3.2514	0.8333
S=0.5		2.0252	**0.4636**	2.7531	0.8041	2.6502	0.6798
S=0.6		2.1181	0.4900	2.1896	0.6172	2.7466	0.6992
S=0.7		2.6645	0.5899	1.9063	**0.5217**	2.5784	**0.6553**
S=0.8		3.2922	0.7311	2.3955	0.5930	2.8884	0.7144

Table D.5.: Parametric study of the plasterboard.

Parameters		Plasterboard					
		90°		120°		60°	
S	α_R	Mean	NMSE	Mean	NMSE	Mean	NMSE
0.4	10	3.7381	0.7925	3.1956	**0.7976**	3.6841	0.8788
0.4	9	3.5300	0.7474	3.5350	0.8862	3.5312	0.8712
0.4	8	3.5240	0.7618	3.5283	0.8840	3.7068	0.8941
0.4	7	3.3054	0.7143	3.4324	0.8598	3.6044	0.8699
0.4	6	3.2608	**0.6918**	3.5504	0.8801	3.6491	0.8891
0.4	5	3.5137	0.7635	3.7760	0.9580	3.5412	**0.8486**
0.4	4	3.3225	0.7138	3.6473	0.9477	3.6588	0.8911
0.4	3	3.2807	0.7232	3.9382	1.0170	3.5444	0.8840
0.4	2	3.3047	0.7297	4.3244	1.1079	3.8141	0.9531
0.4	1	3.6560	0.7757	4.4735	1.1552	3.9453	0.9806
0.5	10	3.5213	0.7827	3.6748	0.8985	4.0034	0.9608
0.5	9	3.1551	0.6900	3.5793	0.8705	4.0768	0.9588
0.5	8	3.0899	0.6610	3.6905	0.9151	3.8918	0.9309
0.5	7	3.2050	0.6812	3.6670	0.9090	4.0919	0.9598
0.5	6	3.1224	0.6850	3.6676	0.9149	3.6773	0.8968
0.5	5	2.9304	**0.6414**	3.7411	0.9253	3.8566	0.9244
0.5	4	3.1896	0.6969	3.4868	**0.8645**	3.7162	0.8832
0.5	3	2.8213	**0.6405**	3.5658	0.8972	3.7168	0.8922
0.5	2	3.2486	0.7091	3.7368	0.9533	3.6839	**0.8806**
0.5	1	3.3892	0.7328	3.9283	1.0436	3.6780	0.9025
0.6	10	3.6586	0.7809	4.4062	1.0375	4.9301	1.1327
0.6	9	3.4034	0.7486	4.2467	1.0221	4.7568	1.1035
0.6	8	3.5831	0.7757	3.9273	0.9781	4.5987	1.0695
0.6	7	3.1622	0.6926	3.8343	0.9457	4.4534	1.0559
0.6	6	3.3942	0.7350	3.7632	0.9321	4.2666	1.0314
0.6	5	3.1876	**0.6924**	3.8118	0.9459	4.2026	0.9874
0.6	4	3.3818	0.7312	3.8168	0.9433	4.0828	**0.9550**
0.6	3	3.2850	0.7130	3.5927	0.9137	4.1298	0.9874
0.6	2	3.3275	0.7085	3.5434	**0.9082**	3.5934	0.8690
0.6	1	3.3610	0.7288	3.8002	0.9260	3.6873	0.9120

Table D.6.: Low range parametric study of the plasterboard.

References

[Abdi, 2001] A. Abdi, C. Tepedelenlioglu, M. Kaveh and G. Giannakis, "On the estimation of the K parameter for the Rice fading distribution," *IEEE Communications Letters*, pp. 92–94, March 2001.

[Akeyama, 2005] A. Akeyama, T. Hirose, K. Sakamoto and A. Kanazawa, "Study on mm Wave Propagation Characteristics to Realize WPANs," *IEEE Standardization Document IEEE802.15-04/0094r0*, 2005.

[Al-Nuaimi, 2002] M.O. Al-Nuaimi and A.G. Siamarou, "Coherence bandwidth characterization and estimation for indoor Rician multipath wireless channels using measurements at 62.4GHz," *IEE Proceedings Microwaves, Antennas and Propagation*, vol.149, no.3, pp.181-187, Jun 2002.

[Andersen, 1994] J.B. Andersen, "Transition zone diffraction by multiple edges," *IEE Proceedings Microwaves, Antennas and Propagation,* vol.141, no.5, pp.382-384, Oct 1994.

[Andersen, 1997] J. B. Andersen, "UTD Multiple-Edge Transition Zone Diffraction," *IEEE Transactions on Antennas and Propagation*, vol. 45, no. 7, pp. 1093-1097, Jul 1997.

[Balanis, 1989] C. A. Balanis, *Advance Engineering Electromagnetics*, John Wiley & Sons, New York, May 1989.

[Beckmann, 1963] P. Beckmann and A. Spizzichino, *The scattering of electromagnetic waves from rough surfaces*, Pergamon Press, 1963.

[Bello, 1963] P. Bello, "Characterization of randomly time-variant linear channels," *IEEE Transactions on Communications Systems,* vol.11, no.4, pp.360-393, December 1963.

[Bertoni, 2000] H.L. Bertoni, *Radio Propagation for Modern Wireless Systems*, Prentice-Hall, January 2000.

[Capolino, 1997] F. Capolino, I.M. Albani, S. Maci and R. Tiberio, "Double diffraction at a pair of coplanar skew edges," *IEEE Transactions on Antennas and Propagation*, vol.45, no.8, pp.1219-1226, August 1997.

[Ciccognani, 2005] W. Ciccognani, A. Durantini, and D. Cassioli, "Time domain propagation measurements of the UWB indoor channel using PN-sequence in the FCC-compliant band 3.6–6 GHz," *IEEE Transactions on Antennas and Propagation*, vol. 53, no. 4, pp. 1542–1549, April 2005.

[Collonge, 2004] S. Collonge, G. Zaharia and G.E. Zein, "Wideband and dynamic characterization of the 60 GHz indoor radio propagation—Future home WLAN architectures", Ann. Télécommun., vol. 58, no. 3–4, pp. 417–447, 2003.

[Correia, 1994] L. M. Correia, P.O. Frances, "Estimation of materials characteristics from power measurements at 60 GHz," *in 5th IEEE International Symposium on Personal, Indoor and Mobile Radio Communications Wireless Networks-Catching the Mobile Future*, The Hague, Netherlands, vol. 2, pp. 510-513, September 1994.

[COST 231, 1999] COST 231, "Digital mobile radio towards future generation systems," *Off. for Off. Publ. of the Eur. Commun.*, Luxembourg, 1999.

[Czink, 2006] N. Czink, P. Cera, J. Salo, E. Bonek, J.P. Nuutinen, J. Ylitalo, "Improving clustering performance using multipath component distance," *Electronics Letters* , vol.42, no.1, pp.33-35, January 2006.

[Czink, 2006bis] N. Czink, P. Cera, J. Salo, E. Bonek, J.P. Nuutinen and J. Ylitalo, "A Framework for Automatic Clustering of Parametric MIMO Channel Data Including Path Powers," *IEEE Vehicular Technology Conference, VTC-2006 Fall 64th*, pp.1-5, 25-28 September 2006.

[Degli-Esposti, 2001] V. Degli-Esposti. "A Diffuse Scattering Model for Urban Propagation Prediction", *IEEE Transactions on Antennas and Propagation,* 49 (7), pp. 1111-1113, July 2001.

[Degli-Esposti, 2007] V. Degli-Esposti, F. Fuschini, E.M. Vitucci and G. Falciasecca, "Measurement and Modelling of Scattering From Buildings," *IEEE Transactions on Antennas and Propagation*, vol. 55, no. 1, pp. 143-153, January 2007.

[Deschamps, 1972] G. A. Deschamps, "Ray techniques in electromagnetic," *Proceedings of the IEEE*, vol. 60, no. 9, pp. 1022-1035, September 1972.

[Erricolo, 2001] D. Erricolo and P.L.E. Uslenghi, "Two-dimensional simulator for propagation in urban environments," *IEEE Transactions on Vehicular Technology*, vol. 50, no. 4, pp. 1158–1168, July 2001.

[Erricolo, 2002] D. Erricolo, "Experimental validation of second-order diffraction coefficients for computation of path-loss past buildings," *IEEE Transactions on Electromagnetic Compatibility*, vol.44, no.1, pp.272-273, February 2002.

[Erricolo, 2002bis] D. Erricolo, G. D'Elia and P.L.E. Uslenghi, "Measurements on scaled models of urban environments and comparisons with ray-tracing propagation simulation," *IEEE Transactions on Antennas and Propagation,* vol. 50, no. 5, pp. 727–735, May 2002.

[Fleury, 2000] B. H. Fleury, "First- and Second-Order Characterization of Direction Dispersion and Space Selectivity in the Radio Channel," *IEEE Transactions on Information Theory*, Vol. 46, No. 6, pp 2027-44, September 2000.

[Fu, 2013] W. Fu, J. Hu and S. Zhang, "Frequency-domain measurement of 60 GHz indoor channels: a measurement setup, literature data, and analysis," *IEEE Instrumentation & Measurement Magazine*, vol.16, no.2, pp.34-40, April 2013.

[Garcia, 2010] A.P. García-Ariza, F. Wollenschläger, S.M. Feeney, S. Salous and R.S. Thomä, "60 GHz channel sounding based on frequency-modulated-continuous-wave techniques," COST 2100, TD(10)10009, Athens, Greece, February 2010.

[Garcia-Pardo, 2012] C. Garcia-Pardo, J.M.Molina-Garcia-Pardo, A. Garrido-Cervantes, J. Muhehe, L. Juan-Llácer, "Frequency Dependence of 2-5GHz Polarized UWB Channel Parameters in Office Environment," *IEEE Transactions on Antennas and Propagation*, vol. 60, no. 6, pp. 2970-2979, June 2012.

[Gong, 1989] J. Gong, T.S.M. Maclean, Z. Wu, "Radiowave propagation over rectangular plateau", *Electronics Letters,* vol. 25, no. 11, pp. 707–709, May 1989.

[Gustafson, 2014] C. Gustafson, K. Haneda, S. Wyne and F. Tufvesson, "On mm-Wave Multi-path Clustering and Channel Modeling," IEEE *Transactions on Antennas and Propagation*, vol. 62, no. 3, pp. 1445-1455, March 2014.

 [Gutierrez, 2011] J. Gutierrez, O. Gonzalez, J. Perez, D. Ramirez, L. Vielva, J. Ibañez and I. Santamaria, "Frequency-domain methodology for measuring MIMO channels using a generic test bed," *IEEE Transactions on Instrumentation and Measurement,* vol. 60, no. 3, pp. 827–838, March 2011.

[Han, 2001] J. Han and M. Kamber, *Data mining, Concepts, and Techniques*, The Morgan Kaufmann Series in Data Management Systems, Elsevier Ltd, Oxford, August 2001.

[Haslett, 1991] C. J. Haslett and M. O. Al-Nuaimi, "Prediction of diffracted field strength in the shadow of a flat roofed building," *Electronics Letters*, vol. 27, no. 11, pp. 950–951, May 1991.

[Haslett, 1994] C.J. Haslett, "Modelling and measurements of the diffraction of microwaves by buildings," *IEE Proceedings Microwaves, Antennas and Propagation,* vol.141, no.5, pp.397-401, October 1994.

[Holm, 1996] P.D. Holm, "UTD-diffraction coefficients for higher order wedge diffracted fields," *IEEE Transactions on Antennas and Propagation,* vol.44, no.6, pp.879-888, June 1996.

[Holm, 2000] P.D. Holm, "A New Heuristic UTD Diffraction Coefficient for Nonperfectly Conducting Wedges," *IEEE Transactions on Antennas and Propagation,* vol. 48, no. 8, pp. 1211-1219, August 2000.

[IEEE 802.15.3, 2009] IEEE 802.15.3: Wireless Medium Access Control (MAC) and Physical Layer (PHY) Specifications for High Rate Wireless Personal Area Networks (WPANs) Amendment 2: Millimeter-wave-based Alternative Physical Layer Extension. New York: IEEE, 2009.

[Jacob, 2012] M. Jacob, S. Priebe, R. Dickhoff, T. Kleine-Ostmann, T. Schrader and T. Kurner, "Diffraction in mm and Sub-mm Wave Indoor Propagation Channels," *IEEE Transactions on Microwave Theory and Techniques,* vol.60, no.3, pp.833-844, March 2012.

[Janaswamy, 2000] R. Janaswamy and J. B. Andersen, "Path loss predictions in urban areas with irregular terrain topography," *Wireless Personal Communications*, vol. 12, pp. 255–268, 2000.

[Järveläinen, 2013] J. Järveläinen, H. Katsuyuki, V. Degli-Esposti, E. M. Vitucci and C. Gustafson, "Modeling Polarimetric Properties in 60 GHz Full Scattering Propagation Prediction Method," *EURO-COST*, TD(13)08053, Ghent, Belgium, 26-27 September, 2013.

[Järveläinen, 2014] J. Järveläinen and K. Haneda "Sixty gigahertz indoor radio wave propagation prediction method based on full scattering model*," Radio Science,* vol. 49*,* pp. 293–305*,* April 2014.

[Jay, 2009] Y. Jay, D. Liu and N. C. Bird, "Guest Editorial for the Special Issue on Antennas and Propagation Aspects of 60–90 GHz Wireless Communications," *IEEE Transactions on Antennas and Propagation*, vol.57, no.10, pp. 2817–2819, October 2009.

[Juan-Llácer, 1997] L. Juan-Llacer and N. Cardona, "UTD solution for the multiple building diffraction attenuation function for mobile radiowave propagation," *Electronics Letters*, vol.33, no.1, pp.92-93, 2 Jan 1997.

[Juan-Llácer, 2002] L. Juan-Llácer and J.L. Rodríguez, "A UTD-PO solution for diffraction of plane waves by an array of perfectly conducting wedges," *IEEE Transactions on Antennas and Propagation*, vol. 50, no. 9, pp. 1207–1211, September 2002.

[Kara, 2002] A. Kara and E. Yazgan, "Roof shape modelling for multiple diffraction loss in cellular mobile communication systems," *International Journal of Electronics*, vol. 89, no. 10, pp. 753–758, 2002.

[Keller, 1962] J.B. Keller, "Geometrical theory of diffraction," *Journal Optical Society American*, vol. 52, no. 2, pp. 116-130. 1962.

[Kivinen, 2007] J. Kivinen, "60-GHz Wideband Radio Channel Sounder," *IEEE Transactions on Instrumentation and Measurement,* vol.56, no.5, pp.1831-1838, October 2007.

[Kleine-Ostmann, 2012] T. Kleine-Ostmann, M. Jacob, S. Priebe, R. Dickhoff, T. Schrader and T. Kurner, "Diffraction measurements at 60 GHz and 300 GHz for modeling of future THz communication systems," *International Conference on Infrared, Millimeter, and Terahertz Waves (IRMMW-THz), 2012 37th*, vol., no., pp.1,2, 23-28 September 2012.

[Koutitas, 2006] G. Koutitas and C. Tzaras, "A UTD Solution for Multiple Rounded Surfaces," *IEEE Transactions on Antennas and Propagation*, vol. 54, no. 4, pp. 1277-1283, April 2006.

[Kouyoumjian, 1974] R. G. Kouyoumjian and P. H. Pathak, "A Uniform Geometrical Theory of Diffraction for an Edge in a Perfectly Conducting Surface," *Proceedings of the IEEE*, vol. 62, no. 11, pp. 1448-1461, November 1974.

[Kyro, 2013] M. Kyro, V. Semkin and V. Kolmonen, "Empirical characterization of scattering pattern of built surfaces at mm-wave frequencies," *7th European Conference on Antennas and Propagation (EuCAP)*, pp.112-115, 8-12 April 2013.

[Luebbers, 1984a] R. J. Luebbers, "Finite conductivity uniform GTD versus knife edge diffraction in prediction of propagation path loss," *IEEE Transactions on Antennas and Propagation,* vol. 32, no. 1, pp. 70–76, January 1984.

[Luebbers, 1984b] R. J. Luebbers, "Propagation Prediction for Hilly Terrain using GTD Wedge Diffraction," *IEEE Transactions on Antennas and Propagation*, vol. 32, no. 9, pp. 951-955, September 1984.

[Luebbers, 1989] R.J. Luebbers, "A heuristic UTD slope diffraction coefficient for rough lossy wedges," *IEEE Transactions on Antennas and Propagation*, vol.37, no.2, pp.206-211, February 1989.

[Maciel, 1993] L.R. Maciel, H.L. Bertoni and H. Xia, "Unified approach to prediction of propagation over buildings for all ranges of base station antenna height," *IEEE Transactions on Vehicular Technology,* vol.42, no.1, pp.41-45, February 1993.

[Maltsev, 2010] A. Maltsev, R. Maslennikov, A. Sevastyanov, A. Lomayev, A. Khoryaev, A. Davydov and V. Sorin, "Characteristics of indoor millimeter-wave channel at 60 GHz in application to perspective WLAN system," *Conference on Antennas and Propagation (EuCAP), Proceedings of the Fourth European*, pp.1-5, 12-16 April 2010.

[Mariage, 1994] P. Mariage, M. Lienard and P. Degauque, "Theoretical and experimental approach of the propagation of high frequency waves in road tunnels," *IEEE Transactions on Antennas and Propagation*, vol. 42, no. 1, pp. 75-81, 1994.

[Martinez-Ingles, 2013] M.T. Martinez-Ingles, J.M. Molina-Garcia-Pardo, J.V. Rodríguez, J. Pascual-García and L. Juan-Llácer, "Experimental UWB and mmW Indoor Radio Channel Characteristic Comparison," *IEEE AP-S/USNC-URSI Symposium Orlando,* 2013.

[Millington, 1962] G. Millington, R. Hewitt, and F. Immirzi, "Double knife edge diffraction in field strength predictions", *IEE Proceedings*, vol. 16, pp. 419-429, 1962.

[Minghini, 2014] L. Minghini, R. D'Errico, V. Degli Esposti and E.M. Vitucci, "Electromagnetic simulation and measurement of diffuse scattering from building walls," *COST IC1004*, TD(14)09064, Ferrara, Italy. 5-7 February, 2014.

[Molina-Garcia-Pardo, 2004] J.M. Molina-Garcia-Pardo, J.V. Rodríguez and L. Juan-Llácer, "Wide-band measurements and characterization at 2.1 GHz while entering in a small tunnel," *IEEE Transactions on Vehicular Technology*, vol.53, no.6, pp. 1794–1799, November 2004.

[Molisch, 2005] A.F. Molisch, "Ultrawideband propagation channels—Theory, measurement, and modeling", *IEEE Transactions on Vehicular Technology.*, 54, (5), pp. 1528–1545, 2005.

[Neve, 1994] M.J. Neve and G.B. Rowe, "Contributions towards the development of a UTD-based model for cellular radio propagation prediction," *IEE Proceedings Microwaves, Antennas and Propagation,* vol.141, no.5, pp. 407-414, October 1994.

[Pagani, 2008] P. Pagani, F. Tchoffo and P. Pajusco, *Ultra-Wideband Radio Propagation Channels. A Practical Approach*, Bernard Uguen ISTE Ltd and John Wiley & Sons, Inc. 2008.

[Papoulis, 2002] A. Papoulis and S.U. Pillai, *Probability, Random Variables and Stochastic Processes*, McGraw-Hill, 4th Edition. 2002.

[Park, 2007] C. Park and T. S. Rappaport, "Short-range wireless communications for next-generation networks: UWB, 60 GHz millimeter-wave WPAN, and ZigBee," *IEEE Transactions on Wireless Communications*, vol. 14, pp. 70–7, August 2007.

[Pathak, 1979] P. H. Pathak, "An Asymptotic Analysis of the Scattering of Plane Waves by a Smooth Convex Cylinder," *Radio Science*, vol. 14, (3), pp. 419-435, 1979.

[Peter, 2007] W. Peter, W. Keusgen and R. Felbecker, "Measurement and raytracing simulation of the 60 GHz indoor broadband channel: Model accuracy and parameterization," *in Proceedings European Conference Antennas and Propagation (EuCAP2007)*, Edinburgh, UK, pp. 1–8, November 2007.

[Ranvier, 2007] S. Ranvier, J. Kivinen, and P. Vainikainen, "Millimeter-Wave MIMO Radio Channel Sounder," *IEEE Transactions on Instrumentation and Measurement*, Vol. 56, No. 3, pp. 1018-1024, June 2007.

[Rappaport, 1996] T. S Rappaport, *Wireless Communication Principle and Practice*, Ed. Prentice Hall. 1996.

[Rappaport, 2002] T. S. Rappaport, *Wireless Communications: Principle and Practice*, 2nd edition, Ed. Prentice Hall, PTR, NJ, USA, 2002.

[Richter, 2005] A. Richter, "Estimation of radio channel parameters: models and algorithms," Thesis, TU Ilmenau, 2005.

[Robotics, 2014] A. Robotics, Xy linear positioner, modular linear positioners tGlide and step motor systems, [online] [30-05-2014] Available: <http://www.arrickrobotics.com/>. 2014.

[Rodríguez, 2005] J.V. Rodríguez, J.M. Molina-Garcia-Pardo and L. Juan-Llácer, "An improved solution expressed in terms of UTD coefficients for the multiple-building diffraction of plane waves," *IEEE Antennas and Wireless Propagation Letters*, vol. 4, pp. 16–19, December 2005.

[Rodríguez, 2007] J.V. Rodríguez, J.M. Molina-Garcia-Pardo and L. Juan-Llácer, "A new solution expressed in terms of UTD coefficients for the multiple diffraction of spherical waves by a series of buildings," *Radio Science*, vol. 42, RS4011, 2007.

[Rodríguez, 2008] J.V. Rodríguez, J.M. Molina-Garcia-Pardo and L. Juan-Llácer, "A Hybrid UTD-PO Solution for Multiple-Cylinder Diffraction Analysis Assuming Spherical-Wave Incidence," *IEEE Transactions on Antennas and Propagation*, vol. 56, no. 9, pp. 3078-3081, September 2008.

[Saleh, 1987] A. Saleh and R.Valenzuela, "A Statistical Model for Indoor Multipath Propagation," *IEEE Journal on Selected Areas in Communications,* vol.5, no.2, pp. 128-137, Feb 1987.

[Sanchis, 2012] C. Sanchis-Borras, J.M. Molina-Garcia-Pardo, M. Lienard and P. Degauque, "Performance evaluation of MIMO-OFDM in Tunnels," *Antennas and Wireless Propagation Letters*, vol. 11, pp. 301–304, 2012.

[Saunders, 1991] S. R. Saunders and F. R. Bonar, "Explicit multiple building diffraction attenuation function for mobile radio wave propagation," *Electronics Letters,* vol. 27, no. 14, pp. 1276–1277, July 1991.

[Sibille, 2010] A. Sibille, C. Oestges and A. Zanella, *MIMO from Theory to Implementation*, Elsevier, 2010.

[Smulders, 2002] P. Smulders, "Exploiting the 60 GHz band for local wireless multimedia access: prospects and future directions," *IEEE Communications Magazine*, vol.40, no.1, pp.140–147, 2002.

[Spencer, 2000] Q. Spencer, B. D. Jeffs, M. A. Jensen and A. L. Swindlehurst, "Modeling the Statistical Time and Angle of Arrival Characteristics," *IEEE Journal on Selected Areas in Communications*, Vol. 18, No. 3, pp. 347-360, March 2000.

[Tabakcioglu, 2009] M.B. Tabakcioglu and A. Kara, "Comparison of Improved Slope Uniform Theory of Diffraction with Some Geometrical Optic and Physical Optic Methods for Multiple Building Diffractions," *Electromagnetics*, vol. 29, no. 4, pp. 303-320, 2009.

[Tabakcioglu, 2010] M.B Tabakcioglu and A. Kara, "Improvements on Slope Diffraction for Multiple Wedges," *Electromagnetics*, vol. 30, no. 3, pp. 285-296, 2010.

[Tzaras, 2001] C. Tzaras and S.R. Saunders, "An improved heuristic UTD solution for multiple-edge transition zone diffraction," *IEEE Transactions on Antennas and Propagation,* vol.49, no.12, pp.1678,1682, December 2001.

[Verdone, 2012] R. Verdone and A. Zanella, "Pervasive Mobile and Ambient Wireless Communications, Signal and Communication Techonology," *COST Action 2100*, Springer-Verlag. 2012.

[Vogler, 1982] L.E. Vogler, "An attenuation function for multiple knifeedge diffraction," *Radio Science,* 17(6), 1541–1546. 1982.

[Walfish, 1988] J. Walfish and H. L. Bertoni, "A Theoretical Model of UHF Propagation in Urban Environments", *IEEE Transactions on Antennas and Propagation*, vol. 36, no. 12, pp. 1788-1796, December 1988.

[Wang, 2006] L. Wang, L. Bo and L. Jiao, "A Modified K-Means Clustering with a Density-Sensitive Distance Metric," *Institute of Intelligent Information Processing*, Xidian University Xi'an 710071, China, 2006.

[Whitteker, 1990] J. H. Whitteker, "Diffraction over a flat-topped terrain obstacle," *IEE Proceedings H Microwaves, Antennas and Propagation,* vol. 137, no. 2, pp. 113–116, April 1990.

[WiGig, 2010] "WiGig White Paper: Defining the Future of Multi-Gigabit Wireless Communication", [online] [30-05-2014] Available: <http://wilocity.com/resources/WiGigWhitepaper_FINAL5.pdf>, 2010.

[Xia, 1992] H. H. Xia and H. L. Bertoni, "Diffraction of cylindrical and plane waves by an array of absorbing half-screens", *IEEE Transactions on Antennas and Propagation*, vol. 40, no. 2, pp. 170–177, February 1992.

[Yang, 2005] H. Yang, M.H.A.J. Herben and P.F.M. Smulders, "Impact of antenna pattern and reflective environment on 60 GHz indoor radio channel characteristics," *IEEE Antennas and Wireless Propagation Letters,* vol. 4, pp. 300–303, 2005.

[Yong, 2007] S.K. Yong, *TG3c Channel Modeling Sub-committee Final Report*, 13 March 2007.

[Yong, 2011] S.K. Yong, P. Xia P. and A. Valdes-Garcia, *60 GHz Technology for Gbps WLAN and WPAN: From Theory to Practice*, 1st. Ed. Wiley, 2011.

[Zhang, 1995] W. Zhang, "A more rigorous UTD-based expression for multiple diffractions by buildings," *IEE Proceedings Microwaves, Antennas and Propagation*, vol. 142, no. 6, pp. 481–484, December 1995.

[Zhang, 1998] Y. P. Zhang and Y. Hwang, "Measurements and statistical modeling of 900 MHz radio propagation channels for microcellular and personal communications in tunnels," *Wireless Personal Communications*, vol. 7, no. 1, pp. 25-39, May 1998.

[Zhang, 1999] W. Zhang, J. Lahteenmaki and P. Vainikainen, "A practical aspect of over-rooftop multiple-building forward diffraction from a low source," *IEEE Transactions on Electromagnetic Compatibility,* vol.41, no.2, pp.115-119, May 1999.

[Zhang, 2000] W. Zhang, "Fast two-dimensional diffraction modeling for site-specific propagation prediction in urban microcellular environments," *IEEE Transactions on Vehicular Technology*, vol.49, no.2, pp.428-436, March 2000.

Glossary

2D   Two-dimensional.

3D   Three-dimensional.

AoA   Angle of Arrival.

AoD   Angle of Departure.

CDF   Cumulative Distribution Function.

CIR   Channel Impulse Response.

cm-W   Centimeter-Wave.

DMC   Dense Multipath Components.

DoA   Direction Of Arrival.

DoD   Direction Of Departure.

FDM   Frequency-Division Multiplexing.

FDTD   Finite Difference Time Domain.

Gbps   Gigabits per Second.

GBSM   Geometry Based Stochastic Model.

GTD   Geometrical Theory of Diffraction.

HD   High Definition.

HPBW   Half Power Beamwidth.

IF   Intermediate Frequency.

IFFT   Inverse Fast Fourier Transform.

ISB   Incident shadow boundary.

LAN   Local Area Network.

LoS   Line-of-Sight.

MCD   Multipath Component Distance.

MCS   Modulation and Coding Scheme.

MED   Maximum Excess Delay.

MIMO   Multiple-Input Multiple-Output.

MISO   Multiple-Input Single-Output.

MMSE   Minimum Mean Squared Error.

MPC   Multipath components.

mm-W   Millimeter-wave.

NLoS   Non-line-of sight.

NMSE   Normalized Mean Squared Error.

OFDM   Orthogonal Frequency Division Multiplexing.

OLoS   Obstructed Line-of Sight.

OSTBC   Orthogonal Space-Time Block Code.

PDP   Power-Delay Profile.

PER   Packet Error Ratio.

PHY   Physical.

PL   Path Loss.

P_R   Average received power.

QAM   Quadrature amplitude modulation.

QPSK   Quadrature phase shift keying.

QSTBC   Quasi-orthogonal Space-Time Block Code.

Rb   Bit Rate.

RF   Radio Frequency.

RMS AS   Root Mean Square Angular Spread.

RMS DS   Root Mean Square Delay Spread.

RSD   Reflected Shadow Boundary.

RT   Ray Tracing.

Rx   Receiver.

SISO   Single-Input Single-Output.

SNR   Signal-to-Noise Ratio.

TDM   Time-Division Multiplexing.

TNR   Total Number of Rays.

ToA   Time-delay Of Arrival.

Tx   Transmitter.

UHF   Ultra High Frequency.

ULA   Uniform Linear Array.

URA   Uniform Rectangular Array.

UTD-PO   Uniform Theory of Diffraction -Physical Optics.

UWB   Ultra Wide-Band.

WPAN   Wireless Personal Area Networks.

XPD   Cross Polar Discrimination Factor.

ZVA   Vector Network Analyzer.